Imperial College London
Department of Physics

# Coherent Charge Dynamics In Molecules on the Attosecond to Few-femtosecond Timescale

Oliver George Alexander

Submitted in part fulfilment of the requirements
for the degree of Doctor of Philosophy at
Imperial College London, March 2023

I am the sole author of this thesis, and the work contained within it is my own unless specifically stated otherwise.

Oliver George Alexander

The copyright of this thesis rests with the author. Unless otherwise indicated, its contents are licensed under a Creative Commons Attribution-NonCommercial-ShareAlike 4.0 International Licence (CC BY NC-SA).

Under this licence, you may copy and redistribute the material in any medium or format. You may also create and distribute modified versions of the work. This is on the condition that; you credit the author, do not use it for commercial purposes and share any derivative works under the same licence.

When reusing or sharing this work, ensure you make the licence terms clear to others by naming the licence and linking to the licence text. Where a work has been adapted, you should indicate that the work has been changed and describe those changes.

Please seek permission from the copyright holder for uses of this work that are not included in this licence or permitted under UK Copyright Law.

## Abstract

Electronic coherences in molecules are typically expected to survive for a few femtoseconds. This limits the timescale of charge migration, which is the electronic motion following valence excitation that is the result of electronic wavepackets, i.e. coherent superpositions of excited states. It is of fundamental and practical interest to molecular physics and quantum chemistry to understand how coherent charge migration results in long term outcomes of chemical reactions or in processes such as radiation damage. It may even be possible to bias reaction outcomes to desired products if the states with a wavepacket and their coherences can be controlled, which is the aim of quantum control. In this doctoral thesis, two experiments are also discussed in detail which aim to improve understanding of decohering interactions on this timescale.

The first is a two colour all X-ray pump-probe experiment using an X-ray free electron laser to investigate charge migration of inner valence holes following ionisation of isopropanol vapour. Two hole wavepackets are studied, each corresponding to cluster of states which can be understood as satellites of a single one-hole state broken down due to coupling to two-hole one-particle states (breakdown in the molecular orbital picture of ionisation). Hole lifetimes for these states of 5.1 $\pm$ 3.2 fs and $1^{+2}_{-1}$ fs were measured, and accompanying theoretical investigations are referred to which elucidate the role of the initial spread in nuclear geometries and nuclear motion on decoherence.

The second experiment is in liquid isopropanol, this time looking at the role of the liquid environment of electron trajectories following ionisation via high harmonic generation. This experiment has tangential interest to strong field physics, as the processes involved in high harmonic generation in liquid are investigated. Harmonics up to 50 eV are generated, the highest reported to-date in the condensed phases, and it is found that scattering of electrons from neighbouring molecules dampens but does not exclude recombination.

Accompanying these experiments is the advancement of experimental tools for those and future investigations, especially for the study of liquid systems. For this purpose, flat liquid targets of order 1 µm thickness as well as the tools for transient absorption spectroscopy using a soft X-ray high harmonic generation source are developed.

## Acknowledgements

So many elements are required to come together for worthwhile science that it would be unimaginable to suppose that the work contained here was done alone or without the help of so many people. I am grateful to the support, scientific and morale, that I have received in abundance in recent years and would like to make some acknowledgements now.

Firstly, I would like to thank those at Imperial College whom I worked so closely with. What is not reflected in a thesis is the hard work which goes into the foundations of a working lab - literally blood, toil, tears, and sweat. Although I will now single some people out who they had direct involvement with the work here, our group has a community built up by a wide number of scientists and staff, established and aspiring, who contribute to the great working environment and I thank them too.

Thank you Professor Jon Marangos, my doctoral supervisor, for always guiding me towards the heart of the problem, for excellent advice, and for having the trust in me to explore new ideas. Thank you for the countless opportunities you have afforded me and for your pursuit of the truth through good scientific method and for prioritising collaboration over competition.

Thank you to my coworkers in H012, Dr Douglas Garratt, Dr Timur Avni, Dr Toby Barnard, Jacob Lee, and Clement Ferchaud for the countless hours we have spent together. Whether it was late evenings in the lab, 2pm coffee, or 4pm beers, it was always a pleasure. This was especially appreciated during the long months of COVID lockdown we spent locked in the lab together. Thank you Dr Mary Matthews and Dr Esben Larsen for your support and advice, and for being a good ear when I have problems.

Of course, the real work was done by our ever-useful workshop engineers, Andy Gregory and Conor O'Donovan, and electrical engineer Susan Parker. Thank you for your patience, even when making the seventh adjustment to a part. Thank you as well to Judith Baylis, Marcia Silviato, and Miranda Toora for making all admin problems seamlessly disappear.

I have also been fortunate enough to work with a great number of external collaborators, especially through involvement in XFEL beamtimes and in the general spirit of collaboration. There are too many to name here, but all of those involved, especially in the 'Attosecond Campaign', 'LR25', and recently in 'LX52' have contributed so much. I would like to particularly thank Dr James Cryan and Dr Taran Driver at the LCLS, Dr Carlo Callegari at FERMI, Dr Antonio

Picon at UAM, and Dr Rebecca Ingle at UCL. Special thanks go to Dr Emma Springate, Dr Cephise Cacho, and Dr Richard Chapman of Artemis for my first look into ultrafast physics and the year they spent patiently training me.

Thank you to Prof Ben Sauer, who as director of the CQD CDT, gave me the opportunity to join such an amazing programme. On that note, thank you to my classmates on the CDT who shared evenings of intense study and have become such great friends for it.

I must also thank those who without I would never have had the opportunity to study physics to begin with and certainly not to pursue it for so long, my mother and father, who always guided me towards my interests and encouraged me at every step. Thank you for helping me choose a path which I would enjoy, so that I could pursue academia with enjoyment rather than pressure, and for providing me with everything I needed to do so. Thank you as well to Jen, Dave, and Nic, for always being there, and thank you to my mother- and father-in-law, for your interest and encouragement.

Finally and most importantly, I would like to thank the person who has shared every moment of my time here, my wonderful wife Hailey. The very first thing I did as a member of the centre for doctoral training at Imperial was meet you, and nothing has been more pivotal to the joy I have had since. Thank you for being a constant happiness in my life, for supporting my work, for always being interested in all that I do, and for sharing my passions. There is no denying that moments of a PhD can be stressful, but with you beside me, it was always worth it.

## Author Contributions

I would also like to specifically acknowledge contributions to the work contained in this thesis, which was only possible through the effort of many people. All work was supervised and given scientific direction by Jon Marangos. The design of the nozzle for creating liquid jets was completed by Gediminas Galinis. The modifications to the XAS beamline described in Chapter 5 were completed by the Author, Douglas Garratt, Toby Barnard, Clement Ferchaud, and Jacob Lee. Early measurements and setup for HHG from liquid targets was done by Sebastian Jarosch and the experiments contained here were done by the Author with Toby Barnard and Clement Ferchaud. The SFA calculations were performed by Timur Avni. The measurement of inner valence holes in isopropanol in Chapter 4 were completed at the AMO endstation of LCLS with all of the expertise of the beamline scientists there. The spokesperson of that experiment

was Tom Barrilot, who also worked on the early analysis. The analysis contained here was was performed by the Author in collaboration with Taran Driver and Douglas Garratt and with regular input from James Cryan and Siqi Li. The theory calculations were completed by Bridgette Cooper. A more complete list of those involved can be found in the publication from that work [1]. Technical support for all work at Imperial College was provided by Andy Gregory, Conor O'Donovan, and Susan Parker.

[1] T. Barillot, O. Alexander, B. Cooper, T. Driver, D. Garratt, S. Li, A. Al Haddad, A. Sanchez-Gonzalez, M. Agåker, C. Arrell, M. J. Bearpark, N. Berrah, C. Bostedt, J. Bozek, C. Brahms, P. H. Bucksbaum, A. Clark, G. Doumy, R. Feifel, L. J. Frasinski, S. Jarosch, A. S. Johnson, L. Kjellsson, P. Kolorenč, Y. Kumagai, E. W. Larsen, P. Matia-Hernando, M. Robb, J. E. Rubensson, M. Ruberti, C. Sathe, R. J. Squibb, A. Tan, J. W.G. Tisch, M. Vacher, D. J. Walke, T. J.A. Wolf, D. Wood, V. Zhaunerchyk, P. Walter, T. Osipov, A. Marinelli, T. J. Maxwell, R. Coffee, A. A. Lutman, V. Averbukh, K. Ueda, J. P. Cryan, and J. P. Marangos. Correlation-Driven Transient Hole Dynamics Resolved in Space and Time in the Isopropanol Molecule. *Physical Review X*, 11(3):031048, sep 2021. ISSN 21603308. doi: 10.1103/PhysRevX.11.031048.




- Edvard Munch, 1893, The Scream, National Gallery of Norway

"I have seen my death!"
Anna Bertha, wife of X-ray discoverer Wilhelm Röntgen, upon seeing a medical X-ray of her hand, the first of its kind.

# Contents

**Abstract** **3**

**Acknowledgements** **4**

**Author Contributions** **5**

**1 Introduction** **11**

**2 Interactions of soft X-rays with molecules** **14**
2.1 Molecular wavefunctions (orbitals) . . . . . 14
2.1.1 Basic theory and common approximations . . . . . 14
2.1.2 Correlations & configuration interactions . . . . . 17
2.2 Ionisation . . . . . 18
2.2.1 Breakdown in the molecular orbital picture of ionisation . . . . . 20
2.3 Key interaction processes . . . . . 21
2.3.1 Core to valence excitations . . . . . 21
2.3.2 Resonant inelastic X-ray scattering, Rayleigh scattering, and Auger-Meitner decay . . . . . 22
2.3.3 Elastic X-ray scattering . . . . . 23
2.4 VUV & X-ray spectroscopy for ultrafast science . . . . . 24
2.4.1 X-ray absorption spectroscopy . . . . . 25
2.4.2 Photoelectron spectroscopy . . . . . 26
2.4.3 Ultrafast X-ray scattering . . . . . 27
2.4.4 Other X-ray spectroscopies . . . . . 28

**3 XUV and soft X-ray generation for attosecond science** **35**
3.1 High harmonic generation . . . . . 35
3.1.1 Theory and characteristics of re-collision based HHG . . . . . 36
3.1.2 Experimental observations . . . . . 45
3.1.3 Beyond gas based high harmonic generation . . . . . 47
3.2 X-ray free electron lasers . . . . . 48
3.2.1 Basics of free electron lasing . . . . . 49
3.2.2 Microbunching, seeded FELS, and SASE . . . . . 51
3.2.3 Development of XFELs for ultrafast science . . . . . 53

**4 Relaxation of inner valence holes in isopropanol cations** **73**
4.1 Experimental Overview . . . . . 79
4.2 Available instruments and preprocessing . . . . . 81

4.2.1 Hemispherical electron energy analyser . . . 81
4.2.2 X-ray spectrometer . . . 83
4.2.3 Gas detector . . . 83
4.2.4 XTCAV . . . 84
4.3 Normalisation, sorting, and selection of pulses . . . 87
4.4 Results . . . 92
4.5 Discussion . . . 95

**5 Towards X-ray spectroscopy in liquid targets 104**
5.1 Liquid Target Requirements . . . 105
5.1.1 Methods of creating micrometer flatjets . . . 109
5.2 Nano-fabrication of fan spray type nozzles . . . 111
5.3 Development of a target chamber for liquid-phase NEXAFS . . . 116
5.4 Design considerations for a flatfield spectrometer . . . 118
5.5 Experimental design overview . . . 121
5.6 Commissioning . . . 123
5.7 Future of liquid-phase XAS . . . 128

**6 High harmonic generation in liquid isopropanol 132**
6.1 Setup for measuring liquid high harmonic generation . . . 135
6.2 Origin of harmonic emission . . . 136
6.3 Dependence on the driving field . . . 141
6.4 Mechanism of HHG in the liquid phase . . . 148

**7 Concluding comments and future direction 160**

**A Description of the laser system 166**

# Chapter 1

# Introduction

It is an exciting time for ultrafast X-ray science following significant developments in all of the core components to probe and understand ultrafast dynamics. Tabletop X-ray sources are capable of producing sub-femtosecond X-rays in and beyond the water window and national facilities can produce sub-femtosecond pulses intense enough for multiphoton and strong field X-ray experiments. Molecular theory is now at the point where the inclusion of electronic coherences and the interactions between nuclei and electrons beyond the Born–Oppenheimer approximation is possible. Targets can be created in all of the common states of matter. Combining these elements, it is now becoming possible for the first time to measure an important class of dynamics: the motion of charge wavepackets which is mediated by electronic coherences, i.e. charge migration.

This is crucial, as molecular processes, such as interactions with each other or with light, are mediated on the quantum scale by electrons. Chemical bonds are formed by potential energy surfaces mapped out by electronic wavefunctions, and can be broken when electrons are excited; chemical reactions involve the exchange of charge; intermolecular bonding, such as hydrogen bonding, is mediated by long range interactions of electrons; and high-energy light interacts with electrons to cause radiation damage. If it is possible to better understand the role of these correlations and to benchmark the latest theory, these types of molecular processes can be better understood, or even controlled.

This thesis focuses on using novel methods to study electron dynamics on the timescale of electronic coherences, and the advancement of techniques required to do so. The methods employed here involve interaction of molecules with VUV and soft X-ray photons. Both excitation from X-rays and X-ray probes of electron dynamics offer exciting advantages over lower photon energy alternatives. Importantly, X-rays are able to probe core electronic states of atoms and molecules, either exciting them to continuum states or bound valence orbitals. Core states are important in time resolved studies as they are highly localised to a nucleus. Therefore, upon core-to-valence excitation the excited electrons inside a molecule are also well localised to the same nucleus. Similarly, upon core to continuum excitation (ionisation) the hole is well localised to the same nucleus. This means that X-ray pumps are able to excite a charge wavepacket localised to one point on the potential energy surface. The resulting dynamics are of great fundamental and practical interest, for example in opto-electronic devices and photo-chemistry.

X-ray probes are also specific to atomic states localised in nuclei. Photoelectrons excited from core states are excited from localised wavefunctions greatly simplifying the interpretation of their scattering as they propagate through a material. Auger electrons decaying from valence shells to core holes offer a similar picture, and excitations to valence bands are affected by the local valence occupation of the nucleus due to Fermi blocking.

A secondary aim of this thesis is to apply these methods to the liquid phase. The solid and gas phase are by far the most studied phases of matter in the field of ultrafast physics. Despite their ubiquity, liquids are less well understood, due in part to the difficulty in fabricating and operating liquid targets which meet the requirements for study in the majority of experimental schemes available.

Within this thesis, two experiments targeting electron dynamics are presented as well as steps towards further studies. First though, the theory and background of the research field is described in Chapter 2. Chapter 3 discusses method for generating VUV and soft X-ray light suitable for measurement of electronic coherences.

Chapter 4 then discusses an experiment conducted using emission from an X-ray free electron laser in which the migration of inner valence hole states created in isopropanol vapour was

measured. Two holes states are observed. One, which decays via a frustrated Auger-Meitner process, is measured to have a transient population lasting only $(1 \pm 2)$ fs. The second has a longer lived state of $(13 \pm 8)$ fs with evidence of decoherence both from the initial spread in the nuclear geometries and the subsequent nuclear motion.

Chapter 5 describes the progress made on delivering liquid targets suitable for time resolved X-ray absorption spectroscopy using a high-harmonic generation based light source, including the creation of the targets, in vacuum delivery of liquid sample, and design and installation of a suitable target chamber and spectrometer.

Chapter 6 describes an experiment to investigate the generation of VUV light in liquid isopropanol via high harmonic generation with a few-cycle IR driving field. Evidence is found for a recombination mechanism similar to gas phase high harmonic generation, but with scattering of electrons from neighbouring molecules occurring during the electron excursions from their parent molecules. The implication is that scattering cross sections are encoded into the resulting harmonic emission. High harmonic generation in the liquid phase may then prove a useful probe of liquid phase cross sections, which are thought to be altered by, for example, charge screening, correlations, and exchange potentials.

# Chapter 2

# Interactions of soft X-rays with molecules

## 2.1 Molecular wavefunctions (orbitals)

### 2.1.1 Basic theory and common approximations

To understand the properties and interactions of molecules generally, solutions to the Schrödinger equation must be found for the bodies and forces involved, i.e. nuclei, electrons and the Coulomb interactions between them. Due to the many-body nature of the problem, approximations must be made before there are tractable solutions. One of the most common is the Born-Oppenheimer approximation, which treats nuclei as fixed in space for the purpose of solving the electronic wavefunction. This is reasonable, so long as the timescales of electronic motion are much shorter than those for nuclear motion. For N electrons and M nuclei, the Hamiltonian of that Schrödinger equation is then

$$\mathscr{H} = -\frac{-\hbar^2}{2m_e}\sum_{n=1}^{N}\nabla_n^2 - \frac{e^2}{4\pi\epsilon_0}\left(\sum_{n=1}^{N}\sum_{m=1}^{M}\frac{Z_m}{r_{nm}} + \sum_{n=1}^{N}\sum_{k>n}^{N}\frac{1}{r_{nk}} + \sum_{l=1}^{M}\sum_{m>l}^{M}\frac{Z_l Z_m}{R_{lm}}\right), \qquad (2.1)$$

where $\hbar$ is Plank's reduced constant, $m_e$ is the mass of an electron, $\epsilon_0$ is the permittivity of free space, $Z_i$ is the number of protons in nucleus $i$ ($i = 1, 2, 3, ...M$), $r_{ij}$ is the distance between

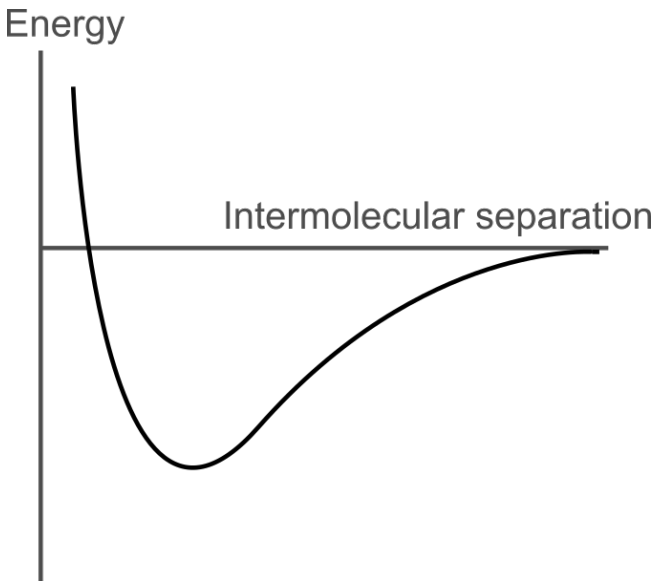



Figure 2.1: A demonstrative potential energy surface for a binding orbital of a diatomic molecule. The 'surface' is this case only depends on one coordinate, the intermolecular separation. The energy is determined by solving the electronic part of the Schrödinger at each fixed separation.

electron $i$ and electron $j$, and $R_{ij}$ is the distance between nucleus $i$ and nucleus $j$.

Other approximations have already been made at this point: the choice of the Schrödinger equation implicitly ignores relativistic effects; spin-orbit effects are also ignored; and it is assumed that nuclei can be treated as point charges. To derive the nuclear wavefunction, the electronic wavefunction is solved for all possible positions of the nuclei to derive a potential energy surface which then forms the potential for the nuclear Hamiltonian. This is not derived here as we are primarily interested in a description of electron states, but it should be noted that electronic state transitions are typically accompanied by vibrational transitions. Figure 2.1 shows a typical slice along a potential energy surface (PES), as viewed in the Born–Oppenheimer approximation. The dimension of the PES increases with the number of nuclear degrees of freedom.

Intuition is gained from considering X-ray interactions with atoms and molecules in the Hartree-Fock (HF) self-consistent field (SCF) method. The general solution to (2.1) is a non-separable many-body electronic wavefunction $\Psi_e(\mathbf{r_1}, \mathbf{r_2}, ...\mathbf{r_N})$, but the HF method assumes that this wavefunction is separable into a product of $N$ single-body electronic wavefunctions (an HF orbital),

$$\Psi_e(\mathbf{r_1}, \mathbf{r_2}, ...\mathbf{r_N}) = \phi_1(\mathbf{r_1})\phi_2(\mathbf{r_2})...\phi_N(\mathbf{r_N}). \tag{2.2}$$

The variational method is then used to derive $N$ coupled eigenvalue equations,

$$F\phi_i(\mathbf{r}) = \epsilon_i\phi_i(\mathbf{r}), \tag{2.3}$$

where $F$ is the derived Fock operator and the eigenvalue $\epsilon_i$ can be interpreted as the energy contribution of the $i$th electron. The full equation for the Fock operator and its derivation are not show here but can be found in standard quantum chemistry, molecular physics, or spectroscopy textbooks, e.g. [1]. The form of the Fock operator is that of a Schrödinger equation, which leads to the interpretation of $\epsilon_i$ as an energy. $\epsilon_i$ is negative for bound states with the most negative eigenvalue, $\epsilon_0$, corresponding to the most bound orbital. There are greater than $N$ solutions, $\epsilon_i$, to Equation 2.3, with the lowest $N$ combining to form the ground state HF orbital. The other bound solutions, $\epsilon_{i\geq N} < 0$, correspond to excited states.

The Fock operator can be expanded into three terms,

$$\hat{F} = \hat{H}^0 + \sum_{j=1}^{N}(2\hat{J}_j - \hat{K}_j). \tag{2.4}$$

The first term, $\hat{H}^0$, is unchanged from the first two terms in Eqn. 2.1 and accounts for the free Hamiltonian and the interaction of the electrons with the nuclei. As the Born-Oppenheimer approximation has been applied, there are no correlations between nuclei and electrons. The remaining two terms, however, are derived from the electron-electron repulsion in (2.1): the Coulomb term, $\hat{J}$, which is electron-electron repulsion as understood in classical electrodynamics; and the exchange term, $\hat{K}$, which is a quantum effect related to the indistinguishability of the electrons and Fermi blocking. The exchange term is the only electron-electron correlation term in the Fock operator.

Finally, to satisfy the anti-symmetry requirements of a wavefunction of fermions, the polarity of the wavefunction must swap with the exchange of an electron. This is not satisfied by the solutions of 2.3, but is solved by a Slater determinant of similar HF orbitals,

$$\Psi(\mathbf{r}_1, \mathbf{r}_2, \ldots, \mathbf{r}_N) = \frac{1}{\sqrt{N!}} \begin{vmatrix} \phi_1(\mathbf{r}_1) & \phi_2(\mathbf{r}_1) & \cdots & \phi_N(\mathbf{r}_1) \\ \phi_1(\mathbf{r}_2) & \phi_2(\mathbf{r}_2) & \cdots & \phi_N(\mathbf{r}_2) \\ \vdots & \vdots & \ddots & \vdots \\ \phi_1(\mathbf{r}_N) & \phi_2(\mathbf{r}_N) & \cdots & \phi_N(\mathbf{r}_N) \end{vmatrix}. \tag{2.5}$$

### 2.1.2 Correlations & configuration interactions

A second electron-electron correlation effect, independent of exchange, is Coulomb correlation. It is the correlation of electron positions due to Coulomb repulsion. It is not implicit in the Fock operator and cannot be included whilst the electron wavefunctions are separable.

The classes of electron dynamics of most interest to this research are those which are not adequately included in the HF method. There are numerous theoretical tools for including Coulomb correlation. Some are not derived from HF methods, such as Green's functions method [2], and density functional theory (DFT) [3] . Post-HF methods use the HF method as a starting point and add correlations explicitly, such as configuration interactions (CI) and Moller-Plesset (MP) perturbation theory [4].

Configurations interactions gives an insightful picture of electron dynamics and correlations, and is used here to interpret results. It starts by considering the molecular wavefunction to be a weighted sum (weights of $c_i$) of molecular wavefunctions, $\psi_i$ called a configuration state function,

$$\Psi = \sum_i c_i \psi_i. \tag{2.6}$$

Each of $\psi_i$ is then set to be a HF orbital. Typically $\psi_0$ is the ground state and other states in the sum are characterised by the number of excitations required from the ground state to reach them and is truncated to save computational time. Assuming this form of solution and aiming to minimise the expectation value of the Hamiltonian, the coefficients $c_i$ can be found as solutions of a general matrix eigenvalue problem.

Correlations are explicitly included in the configurations interactions between the states included in the configuration state function. In practice this means that the choice of molecular

wavefunctions is critical and depends on the class of dynamic being solved. Its application to attosecond X-ray measurements has been demonstrated in, for example, absorption of condensed matter [5] and charge dynamics in molecular ions [6].

## 2.2 Ionisation

The HF method helps interpret interactions with light as photons interacting with individual electrons within a molecular entity. In this picture a photon is absorbed and the electron from one of the orbitals $\psi_i$ is excited. The nuclear wavefunction can also be excited independent of electronic transitions, but generally at lower energies (infrared wavelengths) where those resonances exist. If the photon energy exceeds the binding energy of the electron it interacts with, the electron is excited into the continuum with transition probability given by Fermi's golden rule. When the resulting free-electron's kinetic energy is high, its wavefunction rapidly oscillates in space and the overlap integral in Fermi's golden rule is small. As such, photons absorb most strongly when they are just above the binding energy of the electron they interact with. Therefore, soft X-rays, below 1 keV, interact with the 1s electrons of the second row elements (K-edge) and with the 2s and 2p electrons of third row elements (L-edges). In molecules, the most tightly bound electrons feel most strongly the potentials of individual atoms and can be approximated as atomic orbitals, so molecules will absorb strongly close to the edges of their constituent atoms, with perturbations due to the local chemical environment.

In the molecular orbital picture, the kinetic energy of the photoelectron can be determined from Koopman's theorem, which states that the energy lost by the molecule following ionisation is the energy of the molecular orbital. With the removal of the $i$th electron, with orbital energy $\epsilon_i$, the difference in energy between the ionised and neutral (or less ionised) molecule is then

$$E_{N-1} - E_N = -\epsilon_i. \tag{2.7}$$

Therefore $-\epsilon_i$, which is positive, is the binding energy of that molecular orbital and when a

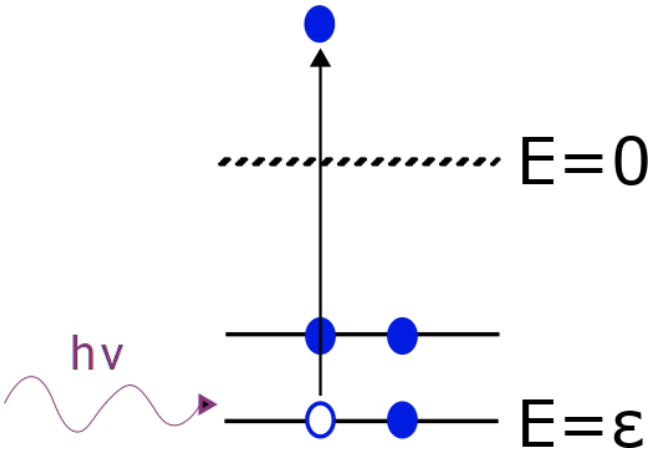



Figure 2.2: A typical energy diagram, showing the ionisation of an electron with binding energy $-\epsilon$. According to Koopman's theorem, the energy of the electron is given by Eqn 2.8.

molecule absorbs a photon of energy $\hbar\omega$, the kinetic energy of the photoelectron is

$$E_{\text{k.e.},i} = \hbar\omega + \epsilon_i. \tag{2.8}$$

Figure 2.2 illustrates the energies involved in ionisation. Illumination of a molecule with an X-ray sources (i.e. photoelectron spectroscopy) therefore probes its single-electron energies. Importantly, this kind of excitation localises the charge distribution of the orbitals which soft X-rays interact with and makes soft X-rays suitable for site-specific spectroscopic methods.

These peaks are broadened by accompanied excitations of the nuclear wavefunction; however, such experiments see more peaks than cannot be explained by the HF method (see Figure 2.3). One such class of peaks is due to the existence of 'shake-up states', which appear as satellites to molecular orbitals with higher binding energies than the main peak. These shake-up states are an excellent example of dynamics which cannot be explained without electron-electron correlations, which in this case drive transitions in electrons other than the one that is itself ionised [7]. The satellites are only at higher binding energies as the ionised molecule is left in an excited state. There also exist 'shake-off states', which are similar but with a transition to a further ionised state.

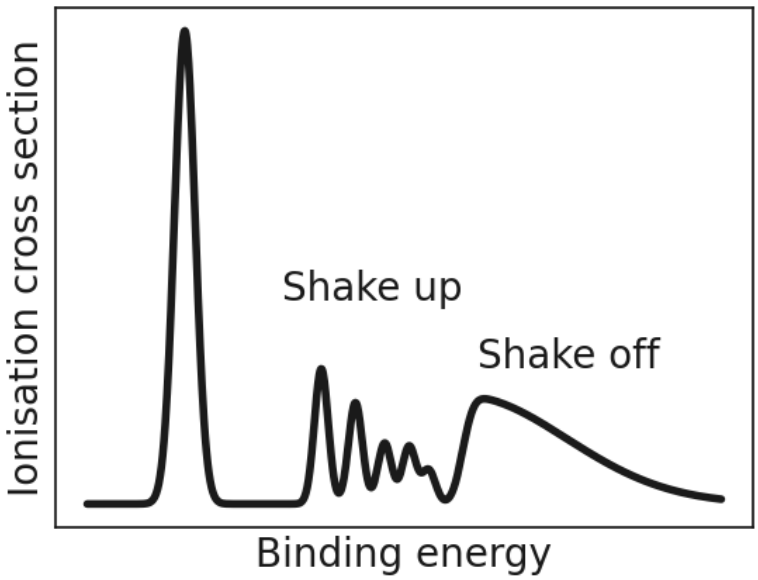



Figure 2.3: Diagrammatic representation of the shake up and shake off states, driven by electron-electron correlations. The shape up states occur first, above the main peak, and involve transitions to valence excited states. The shake off state, at the highest binding energy, involves a transition to a doubly ionised state.

### 2.2.1 Breakdown in the molecular orbital picture of ionisation

There is a third class of peaks which appear as satellites both above and below the main peak in binding energy (see Figure 2.4). These peaks can be understood in the CI picture as coupling between one-hole states, which are singly ionised configurations, and two-hole one-particle states, which are singly ionised configurations with an additional excitation of a bound electron into a valence orbital. This correlation can have a net positive or net negative contribution to the energy of the orbital. When these correlations are sufficiently strong, the satellites begin to form a continuous band, at which point this process is referred to as the breakdown of the molecular orbital picture of ionisation [8]. The theory of this was developed and used in first theoretical studies and experiments in molecular gasses in the late 70s and early 80s, particularly by Cederbaum and coworkers using Green's function methods [9, 10, 11], and by others using CI [12, 13].

Breakdown of the molecular orbital picture of ionisation is central to the theory of charge migration. A wider discussion of this phenomenon and the theory behind it is given at the

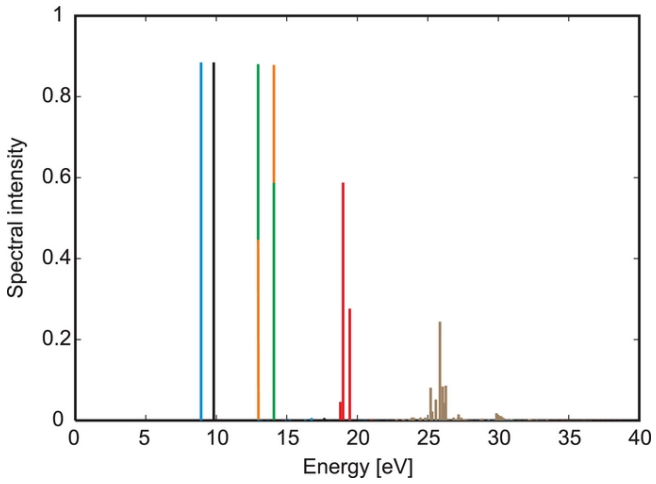



Figure 2.4: Diagrammatic ionisation spectrum of a molecule, showing the effect of electron correlations. An ionisation peak is positioned at the energy of each ionic state relative to the ground state. The ionisation peaks are colour-coded by their character, which is the dominant 1-hole 1-particle molecular orbital contribution to their wavefunction in the CI picture. I.e. blue corresponds to the HOMO, black corresponds to the HOMO+1, etc. In the outer valence, states, single ionisation peaks map to single molecular orbitals. It is also possible to have couplings between 1-hole 1-particle states, as in the case of the yellow and green peaks. In the inner valence, coupling to two-hole one-particle states leads to the emergence of satellite peaks at higher and lower energy and the breakdown in the molecular orbital picture of ionisation. Figure reproduced from [14] with permission from the license holder IOP Publishing Ltd.

beginning of Chapter 4, and is directly relevant to the experiments in that chapter.

## 2.3 Key interaction processes

### 2.3.1 Core to valence excitations

Core electrons can also be excited to bound valence states. Again, Fermi's golden rule determines the transition probabilities and for transitions to bound states introduces the resonance condition. Resonances for excitations from 1s to valence orbitals are just below the K-edge and similarly, for excitations from 2s or 2p states to valence orbitals, below the L-edge. Therefore, soft X-rays drive core to valence transitions in second and third row elements. In molecules, the transitions are to molecular orbitals, so the transition energy and dipole coupling term in the transition probability is sensitive to the molecular environment. These site-specific transitions to molecular orbitals are well suited to the study of electron dynamics.

### 2.3.2 Resonant inelastic X-ray scattering, Rayleigh scattering, and Auger-Meitner decay

In both cases, excitation of a core electron to the continuum and excitation to valence states, a core-hole remains. Though these core-excited states are bound (considering only the remaining cation), they lie energetically above ground and valence excited cationic or further cationic states.

Radiative decay is therefore possible. In this case, one photon is absorbed and one photon is emitted, and the whole process can be thought of as a single scattering event, called resonant inelastic X-ray scattering (RIXS). Where the photons are of equal energy, such that the system returns to its original state, it is called Rayleigh scattering. RIXS was first observed as a sharp increase in synchrotron radiation before absorption edges in metals [15] and subsequently explained theoretically as a second order perturbation to scattering theory [16].

Another relaxation channel is via auto-ionisation, i.e. emission of an electron with kinetic energy equal to the difference between the relaxation energy and the emitted electron's binding energy (Koopmans' theorem). This non-radiative relaxation is referred to as Auger-Meitner decay. It can be explained using Fermi's golden rule where electron-electron repulsion is treated as a perturbation from an effective central field Hamiltonian. The electron repulsion comes from the molecular entity itself and is therefore referred to as an 'autoionising' interaction.

RIXS and Auger-Meitner decay are competing processes. RIXS is favourable for atomic sites with large atomic numbers whilst Auger-Meitner decay is favoured for small atoms [17]. As such, Auger-Meitner decay is of greater importance for soft X-ray absorption. This derives from the relative rates of each process. Both actually increase with atomic number: RIXS is mediated by spontaneous emission, which has cubic scaling with frequency and scales approximately quartically with atomic number [18]; Auger decay also increases monotonically with atomic number, due to the increased Coulomb interaction of a core vacancy, but at a lower rate. The core-excited molecular entity does not necessarily decay directly to its ground state or the ground state of one of its cations and so a series of radiative and non-radiative decays is

possible. A knowledge of the decay lifetimes, and therefore probabilities, of competing processes is essential for understanding electron dynamics in highly excited systems and for experimental considerations (e.g. detection schemes) in probing these dynamics [19].

Auger-Meitner decay was first proposed to exist in the decay of highly excited atoms following alpha decay by Meitner in two seminal papers, in 1922 [20] and 1923 [21], and then unambiguously observed by Auger in cloud chamber experiments in 1925 [22], in which he described the phenomenon of 'tertiary $\beta$-rays'. Meitner's contribution was only recognised much later, so many texts refer to the process simply as Auger decay and the electrons themselves are usually referred to as Auger electrons. Auger-Meitner decay following excitation to the continuum is non-resonant. Thus, the energy of the Auger electrons is non-dispersive (does not increase linearly with the photon energy of the ionising radiation) and is useful in retrieving information about the energy structure of an entity [23, 17]. It is sensitive to shifts in energy due to correlation effects, such as Coulomb repulsion between final state holes, and correlated changes in local electronic structure [24]. In molecules, Auger spectroscopy is also sensitive to the nuclear degrees of freedom [25].

The resonant effect was first observed later in molecular systems [26] as a natural extension to the discovery or RIXS, and like RIXS, is explained by second order perturbation theory. Despite the initial and final states of the entity being independent of the photon energy, resonant decay is dispersive; as such, the Auger electron is often described as having 'remembered' the excitation and there is an interplay between the spectral width of the X-ray source, its central energy, the energetic position of the Auger resonance, and its lifetime [27]. It is treated theoretically as a scattering event, like RIXS, in which a photon is absorbed and an electron is emitted in a single step.

### 2.3.3 Elastic X-ray scattering

Elastic X-ray scattering is a process which leaves the molecular system in an unmodified state, and as such is treated quite differently to the processes already listed. It serves to convert plane waves of X-ray light into spherical waves originating at the scattering centre. On a fundamental

level, scattering occurs due to the interference between the X-rays and X-rays generated by oscillating dipoles. It is therefore dependent on the charge density and the potential felt by that charge.

Mathematically, in the far field a scattered plane wave with wavevector $\mathbf{k}$ is described by the unnormalised wavefunction

$$\psi_{\mathbf{k}}(\mathbf{r}) = e^{i(\mathbf{k}\mathbf{r}-\omega t)} + \frac{f(\theta,\phi)}{r_s} e^{i(\mathbf{k}r_s-\omega t)} \tag{2.9}$$

where $r_s$, $\theta_s$, and $\phi_s$ are the distance, polar angle, and azimuthal angle from the scattering centre. The second term describes the scattered part of the wave and the forward part of the scattering amplitude $f(\theta = 0)$ is related to the total scattering cross section, $\sigma_{\text{tot}}$, by the optical theorem,

$$\sigma_{\text{tot}} = \frac{4\pi}{k} \text{Im} f(0). \tag{2.10}$$

What is typically observed in the far-field is the interference of multiple scattering centres, or by integrating over all of the finite elements within a volume. This is particularly the case when observing diffraction, which is scattering of X-rays from a material with long range order, i.e. a crystal. Considering the form of Eqn. 2.9, an integral over a volume is formally equivalent to a Fourier transform; therefore, the far-field diffraction pattern observed in the intensity of a scattered X-ray is the Fourier transform of $\frac{f(\theta,\phi)}{r_s}$.

## 2.4 VUV & X-ray spectroscopy for ultrafast science

As already alluded to, high energy photons make excellent probes of the electronic states of matter. Many spectroscopic methods in molecular physics are therefore based on VUV or X-ray sources either resonant with core to valence transitions or into the continuum. The workhorse of ultrafast science is a general experimental scheme often referred to as pump-probe spectroscopy, though each of those elements - the pump and the probe (which does the 'spectroscopy') - are incredibly varied. The scheme uses two timed steps, the pump step and the probe step. In the pump step an interaction with the system of interest occurs and initiates the dynamics that are

to be studied. In the probe step, which follows, a second interaction occurs which feeds back a measurement of the system, revealing something which should relate to the dynamics. The time between the pump and probe steps, typically denoted $\tau$, is varied and the measurement is repeated. The measurement then tells the experimentalist the properties of the system at time $\tau$ after the pump step. The temporal response of the system is then known.

### 2.4.1 X-ray absorption spectroscopy

X-ray absorption spectroscopy (XAS), as the name suggests, measures the absorption of X-rays as a function of their energy. The absorption is generally understood in relation to the atomic edges which the absorption is close to, i.e. the K- or L-edge, and sometimes the M-edge (2p). Looking at the complete spectrum, it can be split into three regions relative to an atomic edges: pre-edge, near-edge, or post-edge.

Absorption at the pre-edge is due to transitions from core to valence states. A photon can be absorbed when a few conditions are met: it is resonant between the core state and a valence orbital; the core state is populated; the valence orbital is unoccupied; and there is a non-zero transition matrix element as determined from Fermi's golden rule. In practice, the last condition is a requirement on the symmetry of the molecules that they satisfy the dipole selection rules. With high resolution measurements the different transitions are visible as separate Lorentzian absorption peaks. Absorption in this pre-edge region therefore directly probes the populations of valence states, with the positions of the peaks giving information on the chemical environment local to the atomic site being probed.

The near-edge region probes quasi-bound states. Quasi-bound states are states with energies above the ionisation potential, i.e with negative binding energy. They can be understood in the HF method as orbitals with $\epsilon_i > 0$. These states can be transiently populated due to a potential barrier created by the rotational degrees of freedom in the molecule, the centrifugal barrier. These resonances are referred to as shape resonances due to the influence of the 'shape' of the molecular potential. [1] They are very short-lived and thus broad energetically. Terminology varies in this interdisciplinary technique but spectroscopy in the pre- and near-edge regions

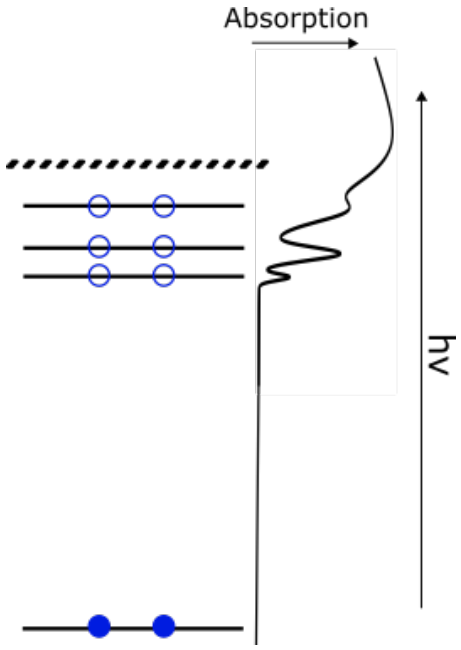



Figure 2.5: Schematic representation of XAS and corresponding energy levels core, valence, and continuum states. Absorption peaks below the absorption edge correspond to transitions from the core to unoccupied valence states. Above the edge, a broad absorption feature corresponds to transitions from core to continuum states. Here, only states in dipole-allowed transitions are drawn.

is often referred to as X-ray absorption near-edge spectroscopy (XANES) or near-edge X-ray absorption fine structure (NEXAFS).

In the post-edge region, transitions are to continuum states. The absorption spectral shape is mostly determined by interference between neighbouring atomic sites, from which structural information can be retrieved. Spectroscopy in this region is sometimes called extended x-ray absorption fine structure (EXAFS) and is applied most commonly in condensed matter research. Figure 2.5 shows how XAS probes transitions to unpopulated bound and continuum states.

### 2.4.2 Photoelectron spectroscopy

Photoelectron spectroscopy (PES) looks directly at the continuum electrons emitted from ionisation. It is also sensitive to core and molecular state populations, their chemical environment, and to interference between neighbouring atomic sites, from which structural information can be retrieved. Angle resolved photoelectron spectroscopy (ARPES) additionally measures the momentum of the outgoing photoelectrons and is of particular importance to condensed matter

systems in which momentum plays an important role in band structure. Electrons from Auger-Meitner decay are also measured, revealing further information about state populations and chemical properties.

### 2.4.3 Ultrafast X-ray scattering

Although not strictly 'spectroscopy', the use of X-ray scattering as a probe of the structure of matter cannot be ignored. It was introduced in Section 2.3.3 that the far-field diffraction pattern of scattered X-rays is the Fourier transform of the scattering amplitude, which in turn relates to the charge distribution within the scatterer, i.e. its structure. If an inverse Fourier transform can be performed on a measured diffraction pattern, the structure is therefore recovered.

Until recently, elastic scattering of X-rays has primarily been studied in the context of diffraction from crystals. This is due to dosage limits imposed by ionisation leading to damage and modifying the structure. Therefore, to produce a strong enough scattering signal whilst avoiding significant ionisation, low intensities are required over many scattering centres. Only in an ordered material is the phase coherent, and therefore crystals are required.

With the advent of high-intensity ultrafast X-ray sources, which are introduced in the following chapter, this problem can be avoided altogether by what is known as diffraction before destruction [28]. The principle is that if enough photons can be scattered in a short enough time that the nuclear motion following radiation damage cannot occur, the undamaged structure is still measured. With increasing intensities, it is therefore possible to measure smaller crystals. An early application of these technique, showcasing its power, was the first reconstruction of the structure of photosystem I, one of the two protein complexes key to photosynthesis [29].

The importance to ultrafast science is that it is now possible to study the structural changes of molecular systems following excitation with a pump pulse. For example, the ring opening of cyclohexadiene [30].

### 2.4.4 Other X-ray spectroscopies

Other spectroscopic methods are available to the experimentalist, which are not described in detail here, for instance: spectroscopy based on RIXS, or the non-resonant equivalent x-ray emission spectroscopy (XES); measurement of ions which may include coincidence counting such as that in cold target recoil ion momentum spectroscopy (COLTRIMS). Nonlinear interactions, involving multiple pump photons, are also of interest, such as the X-ray Raman effect [31, 32] and double core hole generation [8]. Other spectroscopies also exist with unconventional pumps or probes, such as high harmonic generation spectroscopy, which is discussed in Section 3.1.

# References


[1] Joachim Stöhr. *NEXAFS Spectroscopy*, volume 25 of *Springer Series in Surface Sciences*. Springer Berlin Heidelberg, Berlin, Heidelberg, 1992. ISBN 9783540544227. doi: 10.1007/978-3-662-02853-7. URL http://link.springer.com/10.1007/978-3-662-02853-7http://books.google.com.au/books?id=N5NBD0393ZYC.

[2] L S Cederbaum. Application of Green's functions to excitations accompanying photoionization in atoms and molecules. *Molecular Physics*, 28(2):479–493, aug 1974. ISSN 0026-8976. doi: 10.1080/00268977400103011. URL https://doi.org/10.1080/00268977400103011.

[3] Kieron Burke. Perspective on density functional theory. *Journal of Chemical Physics*, 136 (15):150901, apr 2012. ISSN 00219606. doi: 10.1063/1.4704546.

[4] C Moller and M S Plesset. Note on an approximate treatment for many-electron systems Phys. *Rev*, 46(6):18–622, 1934.

[5] Antonio Picon, Luis Plaja, and Jens Biegert. Attosecond x-ray transient absorption in condensed-matter: A core-state-resolved Bloch Model. *New Journal of Physics*, mar 2019. ISSN 1367-2630. doi: 10.1088/1367-2630/ab1311. URL http://iopscience.iop.org/article/10.1088/1367-2630/ab1311.

[6] Pascal Krause, Tillmann Klamroth, and Peter Saalfrank. Time-dependent configuration-interaction calculations of laser-pulse-driven many-electron dynamics: Controlled dipole switching in lithium cyanide. *Journal of Chemical Physics*, 123(7):074105, aug 2005. ISSN 00219606. doi: 10.1063/1.1999636. URL http://aip.scitation.org/doi/10.1063/1.1999636.

[7] T. Åberg. Asymptotic double-photoexcitation cross sections of the helium atom. *Physical Review A*, 2(5):1726–1729, nov 1970. ISSN 10502947. doi: 10.1103/PhysRevA.2.1726.

[8] L. S. Cederbaum, F. Tarantelli, A. Sgamellotti, and J. Schirmer. On double vacancies in the core. *The Journal of Chemical Physics*, 85(11):6513–6523, dec 1986. ISSN 00219606. doi: 10.1063/1.451432. URL http://aip.scitation.org/doi/10.1063/1.451432.

[9] L. S. Cederbaum, J. Schirmer, W. Domcke, and W. Von Niessen. Complete breakdown of the quasiparticle picture for inner valence electrons. *Journal of Physics B: Atomic and Molecular Physics*, 10(15):L549, oct 1977. ISSN 00223700. doi: 10.1088/0022-3700/10/15/001. URL https://iopscience.iop.org/article/10.1088/0022-3700/10/15/001https://iopscience.iop.org/article/10.1088/0022-3700/10/15/001/meta.

[10] W. Domcke, L. S. Cederbaum, J. Schirmer, W. von Niessen, C. E. Brion, and K. H. Tan. Experimental and theoretical investigation of the complete valence shell ionization spectra of CO2and N2O. *Chemical Physics*, 40(1-2):171–183, jul 1979. ISSN 03010104. doi: 10.1016/0301-0104(79)85131-9.

[11] P. W. Langhoff, S. R. Langhoff, T. N. Rescigno, J. Schirmer, L. S. Cederbaum, W. Domcke, and W. Von Niessen. Theoretical studies of inner-valence-shell photoionization cross sections in N2 and CO. *Chemical Physics*, 58(1):71–91, jun 1981. ISSN 03010104. doi: 10.1016/0301-0104(81)80047-X.

[12] Nobumitsu Honjou, Takashi Sasajima, and Fukashi Sasaki. Theoretical study of the satellite bands in the valence shell XPS spectra of N2, CO, O2 and NO molecules. *Chemical Physics*, 57(3):475–485, may 1981. ISSN 03010104. doi: 10.1016/0301-0104(81)80226-1.

[13] Reidar Arneberg, Jiri Müller, and Rolf Manne. Configuration interaction calculations of satellite structure in photoelectron spectra of H2O. *Chemical Physics*, 64(2):249–258, jan 1982. ISSN 03010104. doi: 10.1016/0301-0104(82)87091-2.

[14] Alexander I Kuleff and Lorenz S Cederbaum. Ultrafast correlation-driven electron dynamics, jun 2014. ISSN 13616455. URL http://stacks.iop.org/0953-4075/47/i=12/a=124002?key=crossref.e21d15de7e171e6ebe378451ffbb8bf8.

[15] Cullie J. Sparks. Inelastic resonance emission of X rays: Anomalous scattering associated with anomalous dispersion. *Physical Review Letters*, 33(5):262–265, jul 1974. ISSN 00319007. doi: 10.1103/PhysRevLett.33.262. URL https://journals.aps.org/prl/abstract/10.1103/PhysRevLett.33.262.

[16] Yigal B. Bannett and Isaac Freund. Resonant X-ray Raman scattering. *Physical Review*

*Letters*, 34(6):372–376, feb 1975. ISSN 00319007. doi: 10.1103/PhysRevLett.34.372. URL https://link.aps.org/doi/10.1103/PhysRevLett.34.372.

[17] C. D. Broyles, D. A. Thomas, and S. K. Haynes. The measurement and interpretation of the K Auger intensities of Sn113, Cs137, and Au198. *Physical Review*, 89(4):715–724, feb 1953. ISSN 0031899X. doi: 10.1103/PhysRev.89.715. URL https://journals.aps.org/pr/abstract/10.1103/PhysRev.89.715.

[18] M. O. Krause. Atomic radiative and radiationless yields for K and L shells. *Journal of Physical and Chemical Reference Data*, 8(2):307–327, 1979. ISSN 15297845. doi: 10.1063/1.555594.

[19] Walter Bambynek, Bernd Crasemann, R. W. Fink, H. U. Freund, Hans Mark, C. D. Swift, R. E. Price, and P. Venugopala Rao. X-ray fluorescence yields, auger, and coster-kronig transition probabilities. *Reviews of Modern Physics*, 44(4):716–813, oct 1972. ISSN 00346861. doi: 10.1103/RevModPhys.44.716. URL https://journals.aps.org/rmp/abstract/10.1103/RevModPhys.44.716.

[20] Lise Meitner. Über den Zusammenhang zwischen $\beta$- und $\gamma$-Strahlen. *Zeitschrift für Physik*, 9(1):145–152, dec 1922. ISSN 14346001. doi: 10.1007/BF01326963. URL https://link.springer.com/article/10.1007/BF01326963.

[21] Lise Meitner. Das $\beta$-Strahlenspektrum von UX1 und seine Deutung. *Zeitschrift für Physik*, 17(1):54–66, 1923. ISSN 14346001. doi: 10.1007/BF01328663. URL https://link.springer.com/content/pdf/10.1007/BF01328663.pdf.

[22] Pierre Auger. Sur l'effet photoélectrique composé. *Journal de Physique et le Radium*, 6 (6):205–208, jun 1925. ISSN 0368-3842. doi: 10.1051/jphysrad:0192500606020500. URL http://www.edpsciences.org/10.1051/jphysrad:0192500606020500.

[23] J. J. Lander. Auger peaks in the energy spectra of secondary electrons from various materials. *Physical Review*, 91(6):1382–1387, sep 1953. ISSN 0031899X. doi: 10.1103/PhysRev.91.1382. URL https://journals.aps.org/pr/abstract/10.1103/PhysRev.91.1382.

[24] P. Weightman. The contribution of auger spectroscopy to the study of

core hole screening and electron correlation in alloys. *Physica Scripta*, 1989 (T25):165–172, jan 1989. ISSN 14024896. doi: 10.1088/0031-8949/1989/T25/030. URL https://iopscience.iop.org/article/10.1088/0031-8949/1989/T25/030https://iopscience.iop.org/article/10.1088/0031-8949/1989/T25/030/meta.

[25] B. K. McFarland, J. P. Farrell, S. Miyabe, F. Tarantelli, A. Aguilar, N. Berrah, C. Bostedt, J. D. Bozek, P. H. Bucksbaum, J. C. Castagna, R. N. Coffee, J. P. Cryan, L. Fang, R. Feifel, K. J. Gaffney, J. M. Glownia, T. J. Martinez, M. Mucke, B. Murphy, A. Natan, T. Osipov, V. S. Petrović, S. Schorb, Th Schultz, L. S. Spector, M. Swiggers, I. Tenney, S. Wang, J. L. White, W. White, and M. Gühr. Ultrafast X-ray Auger probing of photoexcited molecular dynamics. *Nature Communications*, 5(1):1–7, jun 2014. ISSN 20411723. doi: 10.1038/ncomms5235. URL www.nature.com/naturecommunications.

[26] George S. Brown, Mau Hsiung Chen, Bernd Crasemann, and Gene E. Ice. Observation of the Auger resonant Raman effect. *Physical Review Letters*, 45(24):1937–1940, 1980. ISSN 00319007. doi: 10.1103/PhysRevLett.45.1937.

[27] E. Kukk, S. Aksela, and H. Aksela. Features of the Auger resonant Raman effect in experimental spectra. *Physical Review A - Atomic, Molecular, and Optical Physics*, 53(5): 3271–3277, 1996. ISSN 10941622. doi: 10.1103/PhysRevA.53.3271.

[28] Henry N. Chapman, Carl Caleman, and Nicusor Timneanu. Diffraction before destruction. *Philosophical Transactions of the Royal Society B: Biological Sciences*, 369(1647), jul 2014. ISSN 14712970. doi: 10.1098/rstb.2013.0313.

[29] Henry N. Chapman, Petra Fromme, Anton Barty, Thomas A. White, Richard A. Kirian, Andrew Aquila, Mark S. Hunter, Joachim Schulz, Daniel P. Deponte, Uwe Weierstall, R. Bruce Doak, Filipe R.N.C. Maia, Andrew V. Martin, Ilme Schlichting, Lukas Lomb, Nicola Coppola, Robert L. Shoeman, Sascha W. Epp, Robert Hartmann, Daniel Rolles, Artem Rudenko, Lutz Foucar, Nils Kimmel, Georg Weidenspointner, Peter Holl, Mengning Liang, Miriam Barthelmess, Carl Caleman, Sébastien Boutet, Michael J. Bogan, Jacek Krzywinski, Christoph Bostedt, Săa Bajt, Lars Gumprecht, Benedikt Rudek, Benjamin Erk,

Carlo Schmidt, André Hömke, Christian Reich, Daniel Pietschner, Lothar Ströder, Günter Hauser, Hubert Gorke, Joachim Ullrich, Sven Herrmann, Gerhard Schaller, Florian Schopper, Heike Soltau, Kai Uwe Kühnel, Marc Messerschmidt, John D. Bozek, Stefan P. Hau-Riege, Matthias Frank, Christina Y. Hampton, Raymond G. Sierra, Dmitri Starodub, Garth J. Williams, Janos Hajdu, Nicusor Timneanu, M. Marvin Seibert, Jakob Andreasson, Andrea Rocker, Olof Jönsson, Martin Svenda, Stephan Stern, Karol Nass, Robert Andritschke, Claus Dieter Schröter, Faton Krasniqi, Mario Bott, Kevin E. Schmidt, Xiaoyu Wang, Ingo Grotjohann, James M. Holton, Thomas R.M. Barends, Richard Neutze, Stefano Marchesini, Raimund Fromme, Sebastian Schorb, Daniela Rupp, Marcus Adolph, Tais Gorkhover, Inger Andersson, Helmut Hirsemann, Guillaume Potdevin, Heinz Graafsma, Björn Nilsson, and John C.H. Spence. Femtosecond X-ray protein nanocrystallography. *Nature*, 470(7332):73–78, feb 2011. ISSN 00280836. doi: 10.1038/nature09750. URL `http://www.nature.com/doifinder/10.1038/nature09750`.

[30] M. P. Minitti, J. M. Budarz, A. Kirrander, J. S. Robinson, D. Ratner, T. J. Lane, D. Zhu, J. M. Glownia, M. Kozina, H. T. Lemke, M. Sikorski, Y. Feng, S. Nelson, K. Saita, B. Stankus, T. Northey, J. B. Hastings, and P. M. Weber. Imaging Molecular Motion: Femtosecond X-Ray Scattering of an Electrocyclic Chemical Reaction. *Physical Review Letters*, 114(25):255501, jun 2015. ISSN 10797114. doi: 10.1103/PhysRevLett.114.255501.

[31] Shaul Mukamel, Daniel Healion, Yu Zhang, and Jason D. Biggs. Multidimensional Attosecond Resonant X-Ray Spectroscopy of Molecules: Lessons from the Optical Regime. *Annual Review of Physical Chemistry*, 64(1):101–127, apr 2013. ISSN 0066-426X. doi: 10.1146/annurev-physchem-040412-110021. URL `http://www.annualreviews.org/doi/10.1146/annurev-physchem-040412-110021`.

[32] Jordan T. O'Neal, Elio G. Champenois, Solène Oberli, Razib Obaid, Andre Al-Haddad, Jonathan Barnard, Nora Berrah, Ryan Coffee, Joseph Duris, Gediminas Galinis, Douglas Garratt, James M. Glownia, Daniel Haxton, Phay Ho, Siqi Li, Xiang Li, James Macarthur, Jon P Marangos, Adi Natan, Niranjan Shivaram, Daniel S. Slaughter, Peter Walter, Scott Wandel, Linda Young, Christoph Bostedt, Philip H. Bucksbaum, Antonio Picón, Agostino

Marinelli, and James P. Cryan. Electronic Population Transfer via Impulsive Stimulated X-Ray Raman Scattering with Attosecond Soft-X-Ray Pulses. *Physical Review Letters*, 125(7):073203, aug 2020. ISSN 10797114. doi: 10.1103/PhysRevLett.125.073203. URL https://link.aps.org/doi/10.1103/PhysRevLett.125.073203.

# Chapter 3

# XUV and soft X-ray generation for attosecond science

If one is to study the interaction of soft X-rays with matter or to use this interaction, as described in Chapter 2, the creation, control, and measurement of soft X-ray fields is of critical importance. The two main types of XUV and soft X-ray sources in the attoscience community today are high harmonic generation (HHG) sources and X-ray free electron lasers (XFELs). HHG relies on widely available femtosecond NIR lasers and as such can be conducted in a typical research laboratory. As such, HHG sources are often described as tabletop sources. Conversely, XFELs rely on large scale infrastructure and are currently limited to a few national facilities globally. The experiments detailed in this report utilise both sources, where appropriate, and in the case of Section 6, develops the HHG process itself.

## 3.1 High harmonic generation

High harmonic generation is a process in which a strong driving laser field interacts with a solid, liquid, gas, or plasma to create high-order harmonics of the driving field. It is treated separately to perturbative, low-order harmonic generation as it is in the intensity regime where the polynomial expansion of the nonlinear susceptibility (or equivalently polarisation) breaks down; however, on a fundamental level it is still mediated by the dipole response. HHG is

principally an interaction with electrons within the generating medium and to understand the process theoretically, it is the motion of electrons which is generally considered. Two classes of HHG are differentiated via the description of their electrons: that which can be described in a re-collision based model and that which can be described in a band structure model.

### 3.1.1 Theory and characteristics of re-collision based HHG

HHG in gasses, which is re-collision based, is the only HHG method for producing attosecond soft X-ray pulses. Re-collision based HHG sources have unique characteristics which are determined both by the interacting medium and the driving field. To begin to understand and describe HHG, it is usual to use a semi-classical description, the three-step model [1]. HHG is understood to be a process mediated primarily by the interaction of the driving field with the electrons of the HHG target, and the three-step model describes the behaviour of the electrons in this situation. The three steps are:

1. An intense classical electric field modulates the potential seen by electrons within an atom. This ionises the electron, either via direct ionisation or tunnel ionisation depending on the regime as determined by the Keldysh parameter, which depends on field intensity and frequency [2].

2. The electron then accelerates in the field, which on returning to its parent ion

3. collapses to its original ground state and produces a photon.

The energy of the photon is the difference between the high kinetic energy unbound state and the ground state it collapses to. The maximum energy released can be related to the ionisation energy of the electron, $I$ and the pondermotive energy, $U_p$, of the electron in the classical field,

$$E_{\text{cutoff}} = I + 3.17U_p. \tag{3.1}$$

As pointed out by [1], the flux of high energy photons produced (on the atomic scale) depends on the ionisation rate in the first step and the probability of electrons returning to their parent ion during their trajectory in the second step, i.e. it depends on the spreading of the electron

wavepacket in time and the trajectory, as determined by the driving field. This has immediate consequences for the properties of the emission. For example, re-collision based HHG is typically optimised for linearly polarised driving fields.

With regards to the nuclear wavepacket, it was later shown that recombination probability is proportional to the autocorrelation of the nuclear wavefunction when the electron is ejected and the nuclear wavefunction when the electron recombines [3]. Nuclear motion is slower for heavier nuclei; therefore, heavier isotopes will have large relative yield at longer trajectory times. It should also be noted that return of the trajectory is not sufficient to ensure recombination, with competition from elastic and inelastic scattering.

Whilst the three-step model is useful for physical intuition and description, it is necessary to treat the problem from the perspective of quantum mechanics. One may start by solving the time dependent Schrödinger equation (TDSE),

$$-\frac{\hbar^2}{2m}\frac{\partial^2\psi(\mathbf{r},t)}{\partial\mathbf{r}^2}+V(\mathbf{r},t)\psi(\mathbf{r},t)=i\hbar\frac{\partial\psi(\mathbf{r},t)}{\partial t} \tag{3.2}$$

for a potential $V(\mathbf{r},t)$ which includes contributions from the static potential and driving field – for example, in an atomic gas with a driving field of strength $E(t)$ linearly polarised in x, $V(\mathbf{r},t)=V_{\text{atom}}(\mathbf{r})+xE(t)$.

The TDSE can be solved directly using numerical methods without loss of generality, and doing so provides a testbed for predictions made by other methods; however, this gains little physical intuition into HHG and is computationally expensive enough that calculations which include other effects, for example propagation, are intractable. Alternatively, by making a series of suitable approximations one can derive an analytic expression for the electric dipole in response to a strong driving field.

This is the approach taken in [4], in what is known as the quantum path model. In the quantum path model, it is assumed that

1. Bound electrons are in their ground state, with negligible contributions from excited states.

2. The binding potential (atomic or molecular potential) can be ignored in the continuum (after excitation).

3. The ground state is negligibly depleted.

Assumption (2) is the strong field approximation (SFA). It is shown in [4] that the time dependence of the electron dipole moment,

$$\langle\psi(\mathbf{r},t)|\, x\, |\psi(\mathbf{r},t)\rangle = i\int_{-\inf}^{t} dt' \int d\mathbf{p}^3 d^*(\mathbf{p}+\mathbf{A}(t))\exp(-iS(\mathbf{p},t,t'))E(t')d(\mathbf{p}+\mathbf{A}(t')) + c.c. \tag{3.3}$$

Here, $d(\mathbf{p})$ is the dipole transition matrix element between the ground state and continuum, $\mathbf{A}(\mathbf{t})$ is the vector potential, $\mathbf{p}$ is the canonical momentum of the electron, and $S$ is the semiclassical action which corresponds to the phase accumulated by an electron in the field driven continuum. To derive the HHG spectrum, one must then Fourier transform the result. Saddle point analysis, which requires the dominant contribution to the complex integral to come from the integrand when it has stationary phase, is used to interpret the dipole contribution. It gives the result that the largest contribution to the phase comes from electrons which are ionised into the continuum and recombine at a later time. A resemblance to each step of the three step model can be be drawn from each component of the integral in Equation 3.3, chronologically read from right to left:

1. $E(t')d(\mathbf{p}+\mathbf{A}(t'))$. The electron receives an ionising dipole interaction with the laser field at time $t'$, removing it from its ground state.

2. $\exp(-iS(\mathbf{p},t,t'))$. It then evolves in the continuum and accumulates phase from unitary evolution between time $t'$ and $t$, ignoring the atomic potential (strong field approximation).

3. $d^*(\mathbf{p}+\mathbf{A}(t))$. At time $t$, a second dipole interaction occurs as the electron recombines with its parent nucleus.

Indeed, when introducing the model in [4], a similar scaling law for the cutoff energy as the

Table 3.1: The ionisation potentials of noble gasses, which are commonly used for high harmonic generation targets.

| | **He** | **Ne** | **Ar** | **Kr** | **Xe** |
|---|---|---|---|---|---|
| $I_p$ | 24.59 | 20.18 | 15.76 | 14.00 | 12.13 |

semi-classical model is derived,

$$E_{\text{cuttoff}} = F(I_p/U_p)I_p + 3.17U_p. \tag{3.4}$$

The additional scaling factor for the ionisation potential, $F(I_p/U_p)$, approaches 1.3 in the limit $I_p \ll U_p$ and 1 for large $I_p$. The use of this scaling law is that it derives characteristics of a HHG source from its driving field and the interaction medium.

There is an approximately linear increase in the cutoff energy with increasing ionisation potential of the interaction medium. The high ionisation potentials of noble gasses (see Table 3.1) is the reason that they are the most common targets for re-collison based HHG. There is also a linear scaling with the pondermotive energy, which scales quadratically with the peak electric field, $E_0$, (linearly with intensity, $I$) and quadratically with the driving wavelength $\lambda$:

$$U_p = \frac{e^2 E_0^2 \lambda^2}{16\pi^2 c^2 m_e} = \frac{e^2 I \lambda^2}{8\pi^2 c^3 \epsilon_0 m_e}, \tag{3.5}$$

where $e$ is charge of an electron, $c$ is the speed of light in a vacuum, and $\epsilon_0$ is the permittivity of free space. For this reason, when seeking to reach the highest energy harmonics, femtosecond NIR/MIR lasers in typically short focussing geometries are used. This also demonstrates another benefit to the use of high $I_p$ targets, which can sustain higher $U_p$ without saturating ionisation.

Several predictions are also made about the temporal-energetic (photon energy) properties of HHG sources. From the three-step and quantum path models it is shown that emission only occurs at the time of return of electrons, which can only occur within a certain period within each half-cycle of the driving field. It follows that a short burst of light, an attosecond pulse, is created at each half cycle. The result is a train of attosecond pulses separated by half the period of the driving field, $T$, as shown in Figure 3.1a. If HHG can be restricted to a single half

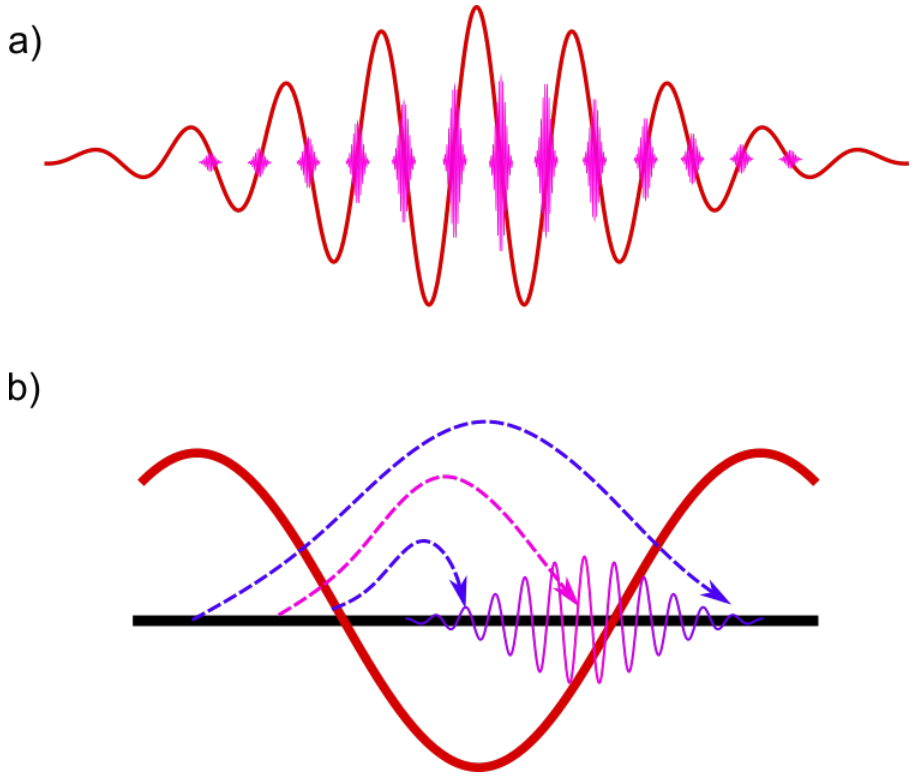



Figure 3.1: a) Temporal structure of the attosecond pulse train, relative to its driving field. Harmonic emission occurs on every half cycle of the laser field. b) The temporal structure the electron trajectories of HHG within a laser cycle, with trajectories and emission only shown for ionisation from one half cycle. Not all trajectories return; the earliest ionisation time which does return is at the peak of the electric field and is also the last to return. As the ionisation occurs later in the cycle, the return time decreases and the trajectory gets shorter. The kinetic energy of the returning electrons (and therefore the photon energy) also increases, up to a maximum, and then begins to decrease. The 'long trajectories' are those in the first regime, where kinetic energy increases with decreasing trajectory length. Conversely, the 'short trajectories' are those where kinetic energy decreases with trajectory time.

cycle, an isolated attosecond pulse will be created. From the different electron trajectories, it is also predicted that the individual attosecond pulses have significant chirp, as shown in Figure 3.1b. Considering first the short trajectories, which are born into the continuum later and arrive earlier, the very shortest trajectories have the lowest kinetic energy upon recombination; and, the later the electron recombines, the higher its energy. Consequently, there is significant chirp, with the photon energy increasing sharply within the first half of the pulse. The long trajectories follow the opposite trend, with the first returning electrons having the highest energy and the latest (the longest trajectories) having the lowest. Trajectories which are born before the peak of the laser half cycle, i.e. before the long trajectories, will not return and do not contribute to the emission.

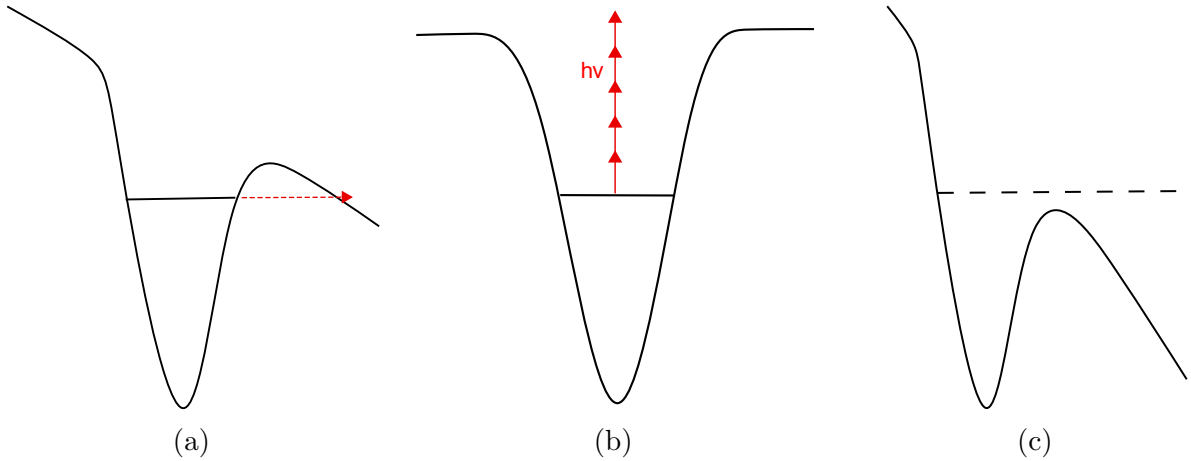



Figure 3.2: Illustration of (a) tunnel ionisation, (b) multi-photon ionisation, and (c) over-the-barrier ionisation.

Another important characteristic for a HHG source is its total yield, i.e. the average or single-shot power emitted from an HHG source, as well as the relative yield of different harmonics. In both cases, it is important to know the ionisation rate as total yield is proportional to the total ionisation rate and the yield of a specific photon energy is proportional to the ionisation rate at the birth time of the contributing trajectories. Ionisation in the strong field approximation is a research interest which predates HHG, and in particular the papers of Keldysh [5], Faisal [6], and Reiss [2] combine to form the basis of SFA theories, which are sometimes referred to as Keldysh-Faisal-Reiss or KFR theories. Keldysh derived an expression for ionisation from a Coulomb potential in a strong field, disentangling the competing processes of tunnel and multi-photon ionisation. Tunnel ionisation is the process by which barrier suppression of the Coulomb potential is sufficient for a bound electron in a molecule to tunnel directly into the continuum, as shown in Figure 3.2(b). Multi-photon ionisation is the process by which the bound electron is simultaneously excited by many photons such that it lies energetically above the Coulomb barrier and is ionised, as shown in Figure 3.2(a). Keldysh derived the rate of tunnel ionisation by neglecting the effect of the Coulomb potential on the continuum electron wavefunction. He took the ansatz that the transition probability amplitude from bound and unperturbed state $|\Psi_0\rangle$ to continuum state $|\Psi_{\mathbf{p}}\rangle$, with momentum $\mathbf{p}$ is given by

$$M(\mathbf{p}) = \int_{-\infty}^{\infty} \langle \Psi_{\mathbf{p}} | \, V_{\text{int}}(t) \, | \Psi_0 \rangle \, , \tag{3.6}$$

where $V_{\text{int}}(t)$ is the interaction potential in interaction picture. On the face of it, neglecting the contribution of a long range potential ($V_{\text{Coulomb}} \propto 1/r$) on $|\Psi_p\rangle$ seems improper, but the effect is only to add an order unity scaling correction to the result and not modify its general form. Faisal generalised Keldysh's theory, deriving the ansatz 3.6 (which is not actually stated in [5] but is implicit [7]) under only the dipole approximation and a restriction on the product of the driving field and potential range. This second condition appears limiting, but is not sufficiently strong to make the theory inappropriate for tunnel ionisation, only over-the-barrier ionisation, in which the field is sufficient to completely suppress its binding potential and leave a barrier-free route to horizontal ionisation. This is depicted in Figure 3.2(c). Over-the-barrier ionisation therefore imposes a limit on the intensities which can be used for HHG. Keldysh observed that the rate of tunnel ionisation should be dependent of the driving field frequency, as at high frequencies there is insufficient time for the electron to tunnel within a laser cycle. Multi-photon ionisation, on the other hand, increases with frequency and thus wins the competition in this limit. The regime of a given strong-field ionising interaction is determined by what is now known as the Keldysh parameter,

$$\gamma = \omega \frac{\sqrt{2m_e I_p}}{eE_0}. \tag{3.7}$$

$\gamma$ can be understood intuitively as proportional to the ratio of the time taken classically for an electron with energy $I_p$ to cross the tunnelling barrier and the time period of the driving field. For $\gamma \ll 1$, tunnel ionisation dominates whilst for $\gamma > 1$, multi-photon ionisation dominates. For example, a 0.5 mJ 1800 nm 15 fs laser pulse focussed to a $1/e^2$ width of 100 µm in argon forms an interaction with $\gamma = 0.175$ at the peak intensity, and ionisation is predominantly from tunnelling.

The combined probability of ionisation from a gas in a single laser period is given by

$$w_0 = \sqrt{\frac{2I_p}{\hbar}}\omega \left(\frac{\gamma}{\sqrt{1+\gamma^2}}\right)^{3/2} S\left(\gamma, \frac{\tilde{I}_p}{\hbar\omega}\right) \exp\left\{-\frac{2\tilde{I}_p}{\hbar\omega}\left[\sinh^{-1}\gamma - \gamma\frac{\sqrt{1+\gamma^2}}{1+2\gamma^2}\right]\right\}, \tag{3.8}$$

where $I_p$ is a modified ionisation potential and $S\left(\gamma, \frac{\tilde{I}_p}{\hbar\omega}\right)$ is a slowly varying function - the full forms of each can be found in [5] but are omitted here for brevity. This expression forms a

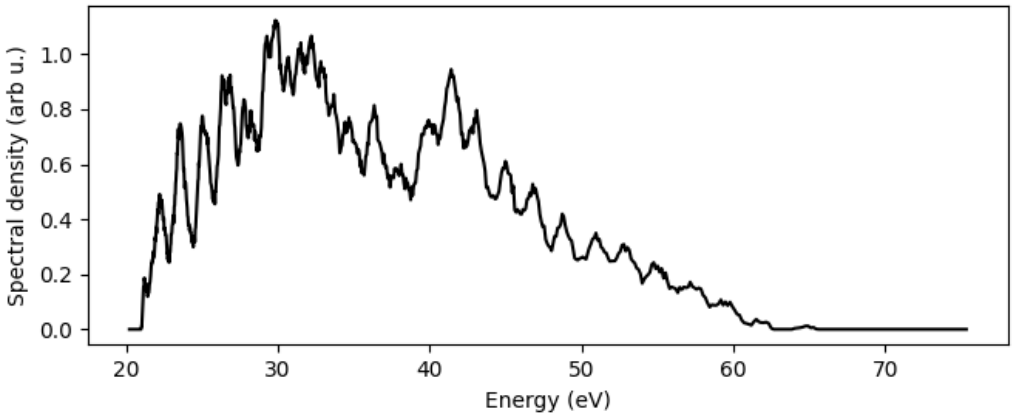



Figure 3.3: Spectrum of high harmonics generated using a CEP stable few-cycle pulse in krypton, extending beyond 60 eV.

pre-factor to the total high harmonic yield. To know the relative yield of different harmonics, one must consider the rate of ionisation at the birth time of the corresponding trajectories. The tunnelling rate is highest when the barrier is most suppressed, i.e. at the peak of each half-cycle.

The exact form of this contribution to the relative yield is not necessary for this work, only to realise that it is different from harmonics in the perturbative regime, which scale inversely with the intensity to the power of the polynomial order. As such, there is an approximately exponential decrease in yield from successive harmonic orders in the perturbative limit. For HHG however, there is no such restriction; this gives the spectrum of HHG a distinctive shape in which successive harmonic orders are of similar order of intensity extending over tens or hundreds of orders, and is commonly described as a plateau.

Given that the harmonic cutoff scales quadratically with wavelength, NIR and MIR lasers are typically required to generate harmonic orders in the soft X-ray region; however, the total harmonic yield is reported to scale unfavourably with $\lambda$. Calculations which use a combination of direct integration of the TDSE and the SFA estimate the scaling as $\precsim \lambda^{-(5\text{–}6)}$ [8]. This was later measured with good agreement in low density xenon and krypton [9]. This is as a result of a combination of factors: longer trajectories lead to greater spreading of the electron wavepacket, lowering the probability of re-collision ($\propto \lambda^{-2}$); conversion of the number of photons to energy contributes a factor $\propto \lambda^{-1}$; and other factors contributing the remaining $\lambda^{-3}$ scaling, such as the effect on the number of field oscillations before re-collision and the motion of the nuclear

wavepacket, which remains an unsettled problem.

So far, here, re-collision based HHG has only been considered on the micro scale, e.g. the response of a single atom in atomic gasses. Macroscopic effects are also fundamental to HHG. Propagation effects of HHG are more comparable to perturbative harmonics in that phase-matching, the equivalence between the wave vectors of the driving field and harmonic emission, plays a critical role to the efficiency of emission. In the case of perfect coherence between emitters, photon emission scales quadratically with the number of emitters. Experimental setups for HHG therefore seek to maximise the number of coherent emitters either by increasing the density or the coherence length of the interaction, whilst mitigated the unwanted effect of re-absorption of the harmonics. The coherence length is roughly the length over which emission is in phase. Contributions to this phase come from four sources:

1. The Gouy phase, $\Delta\mathbf{k}_g$, which is derived from the change in the wavefront at a focus, which results in an apparent lengthening of the wavelength at the focus.

2. The dipole phase, $\Delta\mathbf{k}_d$, which is derived from the change in emission time of photons of a given energy due to changes in the trajectories arising from e.g. change in driving field intensity.

3. Normal dispersion, $\Delta\mathbf{k}_n$, derived from changes in the refractive index of the medium from e.g. a change in gas density.

4. Plasma dispersion, $\Delta\mathbf{k}_n$, derived from changes in plasma density which also shifts the refractive index but is typically treated separately to $\Delta\mathbf{k}_p$.

The total mismatch is then:

$$\Delta\mathbf{k} = \Delta\mathbf{k}_g + \Delta\mathbf{k}_d + \Delta\mathbf{k}_n + \Delta\mathbf{k}_p \tag{3.9}$$

This is further complicated by spatial and temporal variation in the driving field and the interaction medium: The rate of ionisation increases through the pulse, shifting the plasma contribution; intensity varies over the transverse profile of the pulse, affecting the dipole

contribution; Gouy phase necessarily changes dramatically close to the focus; and the density emitters varies in many target systems, e.g. gas jets which disperse into a vacuum chamber, and changes the normal dispersion contribution. For example, a 550 µJ 12 fs pulse focused to 2 PW cm$^{-2}$ into a 4 bar helium target will experience ionisation fractions of a few per cent after propagating only a micrometre lengths [10]. This will clamp the intensity to only half the peak it would experience in vacuum, via plasma defocussing, thus clamping further ionisation and lead to order $\pi$ phase shifts. This effect is greatest at the centre of the focus, causing the edges of the beam to propagate first, distorting the wavefront [10]. In this high intensity regime, emission is therefore limited to the first micrometres of propagation.

### 3.1.2 Experimental observations

The first published observations of HHG in gas targets came in the late 1980's when McPherson et al. [11] were able to identify a deviation from the scaling laws of perturbative harmonics, i.e. the characteristic plateau of HHG, when focusing a UV laser (248 nm) into neon and other noble gasses. Their observation of 17th order harmonics and Ferray et. al's subsequent observations of 21st order harmonics produced with a 1053 nm Nd:YAG laser [12] was rapidly expanded on [13, 14] and by 1992, harmonics up to the 135th order were observed [15]. At this time, it was suspected from Fourier synthesis that the temporal properties of HHG might be suitable for attoscience [16]. The broadband spectrum of peaks separated by regular energy intervals hints at the temporal structure of a series of attosecond pulses separated by half the period of the driving field. In [16], the authors went as far as suggesting that pulses as short as 30 as could be common.

At the turn of the century, several experimental studies verified the creation of attosecond pulses. Interferometry between two HHG sources showed features of sub-100 fs field localisation in attosecond pulse trains [17]. Then cross-correlation of a HHG source and its driving field in a gas target, as measured by the energy of emitted photoelectrons, measured 650 as XUV pulses in one study [18] and 1.8 fs pulses in another [19]. Today, pulses as short as 53 as have been measured using this method [20], which became known as attosecond streaking. Each

of these studies on isolated pulses utilised the previously mentioned method of limiting the harmonic generation to a single half-cycle of the driving field. This has been achieved by gating the HHG in the temporal domain — in [20], for example, polarisation gating is used, which limits the period for which the driving field is linearly polarised to sub-cycle. Alternatively, frequency gating can be employed for sufficiently short (few-cycle) driving fields, where only one half-cycle is sufficiently intense to contribute to the harmonics. Spatiotemporal separation of high harmonic emission has also been achieved through the use of a spatially chirped driving field, and is sometimes referred to as the 'attosecond lighthouse' [21].

The variation of the field maximum between successive half cycles draws attention to the fact that, for few-cycle pulses, the slowly varying envelope approximation is invalid. As a consequence, the carrier envelope phase (CEP) makes an important contribution to the magnitude of electric field extrema within the pulse. In particular, the peak electric field is only maximised when the CEP is such that the peak of the electric field occurs at the peak of the pulse envelope, i.e. $\phi_{\mathrm{CEP}} = 0$. Therefore, changes in the CEP result in changes in the harmonic spectrum and in particular, the cutoff energy achieved.

Measurement of the CEP has been demonstrated using the harmonic yield itself [22], by considering the relative harmonic cutoff energies from each half cycle of the laser. The peak intensity of a half cycle is encoded in the energy of the recombining electrons; the half cycle cutoffs (HCOs), which are the maximum photon energies emitted due to each laser half cycle, are visible in the combined spectrum using a spatially resolved spectrometer. The CEP can then be determined using a retrieval algorithm which compares to a library of theoretical harmonic yields corresponding to varying CEPs. Note, pulse characterisation is required to calculate accurate yields. A passively stable CEP can be obtained by using the idler output of a optical parametric amplifier [23], which has the additional benefit of increasing the wavelength, for a higher HHG cut-off energy.

As was determined from the three-step model, HHG pulses are intrinsically chirped: electrons ionised at $t_c = 0.047$ optical cycles after the field maximum have the highest pondermotive energy [24]. Electrons ionised afterwards follow shorter trajectories and have lower energy. The

shorter trajectories recombine first, creating a positively chirped harmonic signal. Electrons ionised before $t_c = 0.047$ follow longer trajectories and in contrast, create a negatively chirped signal. To create a one-to-one mapping of harmonic order to emission time, short trajectories can be isolated by focusing the pump laser before the gas jet, not allowing them to phase-match [25].

Utilising this knowledge, attosecond experiments have been conducted using HHG. For example, an early experiment with $\sim$100 as resolution was conducted [26] by considering the resulting harmonic signal to be a series of probes separated by the trajectory spacing for consecutive harmonics. Relative strengths of harmonics were then used to calculate the time dependence of the nuclear autocorrelation function and retrieve the nuclear separation using the theory in Ref. [3], discussed previously.

Gas based high harmonic generation has also been used as either a pump or probe in time resolved studies the structure and dynamics of matter on electronic timescales [27, 28, 29] and is now such a well developed method that commercial systems are available.

### 3.1.3 Beyond gas based high harmonic generation

The three-step model interpretation of HHG relies on the concept of a localised potential, typically atomic but also molecular, and a potential free vacuum surrounding it. The quantum picture of solids is very different, as is reflected by their energetics which are best understood as bands in momentum space. Liquids on the quantum scale share some of the characteristics of each. They do not have the long range structure of solids but have some short range order and molecular orbitals of multiple molecules are shared via bonding. High harmonic generation in both solids [30] and liquids[31, 32] have generated significant interest in their mechanisms and application.

The earliest observation of non-perturbative harmonics in solids [30] led to a series of studies [33, 34, 35, 36, 37]. In contrast to a gas, in crystalline media (as is often the case for solids used in these experiments), electrons are not bound to a molecular centre but understood within the Bloch's theorem to be delocalised. The mechanism for HHG in solids is therefore

different and, as of yet, solid HHG sources have been limited to photon energies below 50 eV and indeed the highest energies achieved have been in amorphous solids, where the the nature of the harmonic generation is debatable. Serious debate remains over the characteristics of solid target HHG sources – a debate that was recently reignited with a theory of the emission not in Bloch space [38] – and their applicability as efficient XUV or soft X-ray sources. So far, there is not convincing evidence that such sources offer strong enough advantages over gas sources. A particular concern is the damage accrued on solid targets on a single shot basis due to ablation, and intensity induced colour centres (defects which introduce additional absorption or emission features), or over time due to heating.

This is something that can be avoided in liquids, which are 'self-healing', but are also condensed matter. The mechanism of high harmonic generation in liquids is unclear and much less studied. Molecular orbitals in liquids are not free from interaction with neighbouring molecules, but no long range order exists, and therefore they form an intermediate case between solid and gas. The mechanism of liquid phase HHG is the subject of investigation detailed in Section 6 and a background of the literature and full discussion is given there.

## 3.2 X-ray free electron lasers

Despite its many desirable properties, high harmonic generation is limited in its conversion efficiency, so is unsuitable for applications requiring high average or peak power. In the absence of optical methods for amplifying X-ray pulses, other methods of X-ray generation must be used. The most common is synchrotron radiation, which is radiation from a charge accelerated by a magnetic field and takes its name from the familiar machines for generating it. Synchrotrons have been used for decades to produce X-ray radiation with average powers and brightness orders of magnitude higher than HHG sources, but in general produce almost continuous wave, monochromatic beams. Beams on the order of 100 fs can be achieved, at the expense of average power, by 'slicing' electron bunches through interaction with femtosecond lasers such that only a fraction of the electron bunch radiates. Whilst useful for some applications, this time resolution is unsuitable for the study of processes on the timescale of electronic coherences.

However, much of the technology, techniques, and expertise developed for electron synchrotrons was directly transferred to linear electron accelerators, those used for free electron lasers (FELs). FELs have been used to generate X-rays (then referred to as XFELs) with the high average powers of synchrotrons and the pulse lengths of HHG sources. Despite not being cyclic accelerators, they are sometimes referred to as fourth generation synchrotrons due to the mechanism of their radiation. The advancement and use of third generation synchrotrons is ongoing [39], but their use for ultrafast science has been mostly superseded by XFELs.

### 3.2.1 Basics of free electron lasing

Synchrotron radiation is in general caused by the interaction of relativistic electrons with a periodically modulated magnetic field, causing them to accelerate and emit light according to basic principles of electromagnetism. Contrary to non-relativistic emission from oscillating charges, which is of the typical dipole form, relativistic effects result in a narrow cone of emission. This can be explained by an observed squeezing of time periods by a stationary observer of the accelerated electron bunch. Consider emission from electrons moving towards the observer and producing electromagnetic radiation: the electrons chase the emission such that the perceived time between two events is reduced (squeezed). In the opposite scenario, observing emission in the reverse direction, the time observed increases. Therefore, in the forwards direction, observed acceleration is larger and given that the electric field strength is proportional to the magnitude of the observed radiation, it is also larger in that direction and the emission is directional. This greatly enhances the achievable brightness. Importantly, the radiation emitted by an oscillating relativistic electron also benefits from Doppler shifting in the forwards direction, to shorter wavelengths, scaling with the wavelength of the oscillation, $\lambda_u$, and inversely with the square of the Lorentz contraction,

$$\lambda = \frac{\lambda_u}{\gamma^2}. \tag{3.10}$$

It is this scaling which allows for the generation of hard X-rays.

Wigglers and undulators are two common instruments used to modulate the magnetic field along the path of the electrons for X-ray generation. They are in fact limiting cases of the

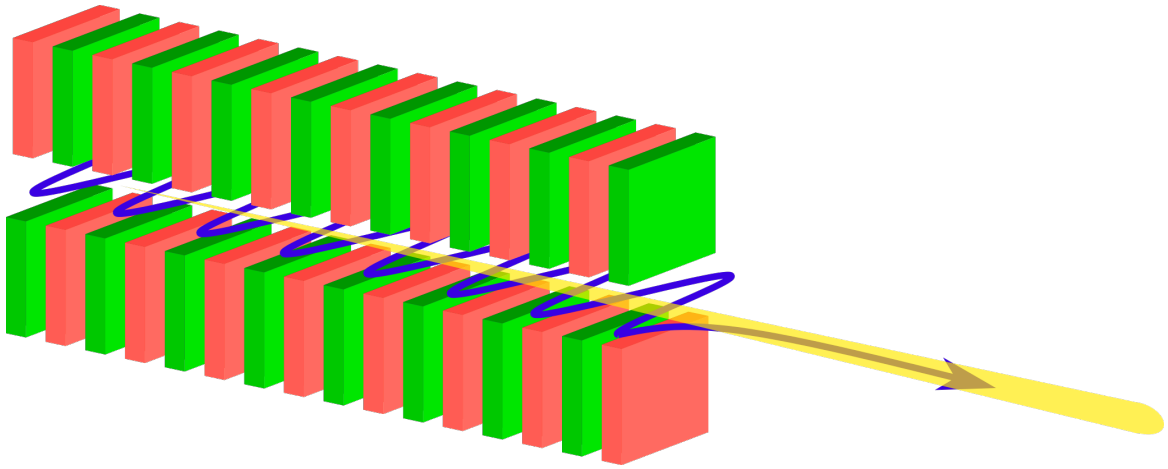


Figure 3.4: Illustration of the working principle of an undulator. Relativistic electrons travelling along the axis of a Halbach array of magnets oscillate in the magnetic field, emitting a narrow cone of X-ray light as they accelerate. In the far-field, there appears to be a single radiation source, but in fact emission is greatest at the turning point in each oscillation, where acceleration is maximised.

same configuration, a Halbach array of either permanent or superconducting magnets. They are characterised by the deflection parameter, which is proportional to the product of the wavelength and field strength of the Halbach array and is typically denoted as $K$ [40]. For undulators $K >> 1$, and for wigglers $K << 1$. Emission between individual bends in an undulator is coherent for a narrow band of wavelengths and as such undulator emission is narrow band and bright compared to wigglers, which have no coherence between bends. The coherence and brightness of emission from undulators is as a result of coherence between emission from successive periods in the undulator. This is achieved when the slippage between the emitting electrons and the X-rays is exactly one period of the X-ray field in the time it takes for the electrons to traverse one undulator period. An undulator and emission from an electron beam is illustrated in Figure 3.4.

Undulator emission from a FEL, as opposed to a synchrotron, is brighter still. This can be explained by coherence between the emitting electrons which occurs when they are bunched. To create electron bunches in a FEL, electrons are typically emitted by the incidence of a pulse laser on a cathode. The cathode is usually placed at the back of an 'RF gun', which is a cavity capable of producing strong radio frequency fields which accelerate the electron bunch to 10s of MeV of energy. Linear accelerators can then be used to accelerate the electron bunches to GeV

energies, and manipulation of the electron bunches can be achieved with, for example, chicanes for the purpose of bunch compression. Modern XFEL facilities use advanced techniques for X-ray generation to gain advantages in their pulse properties, for example in brilliance, pulse length, or wavelength range.

### 3.2.2 Microbunching, seeded FELS, and SASE

One of the most important concepts to XFEL science is the microbunching of electrons caused by interaction between electrons and electromagnetic radiation co-propagating in an undulator. In this situation, there is an exchange of energy governed by the interdependence of the phase between the sinusoidal motion of the electrons and the radiation, $\theta$, and the energy of the electrons relative to a resonance, $\gamma_0$. This is governed by the pendulum equations, derivations of which can be found in textbooks [40] or review papers [41]. The pendulum equations describe how the relative energy of the electrons, $\eta = (\gamma - \gamma_0)/\gamma_o$, and $\theta$ change due to the interaction between the electrons and the radiation. They are parametric in the propagation along the undulator axis, $z$, and given by:

$$\frac{d\theta}{dz} = 2k_u\eta, \tag{3.11}$$

$$\frac{d\eta}{dz} = \frac{eK}{2\gamma_0^2 mc^2} E_0 \cos(\theta + \psi_0), \tag{3.12}$$

where $k_u$ is the wavenumber of the undulator, $e$ is the charge of an electron, $m$ is the mass, $c$ is the speed of light in a vacuum, $E_0$ is the electric field strength of the radiation, and $\psi_0$ is the initial phase of the radiation.

From the pendulum equations, it is understood that electrons which are non-resonant ($\eta \neq 0$) and out-of-phase with the radiation have a change in phase, and out-of-phase electrons also change in energy as they propagate. The overall effect is to push the electrons towards a steady state of $\theta + \psi_0 = (n + 1/2)\pi$ and $\eta = 0$. This is demonstrated in Figure 3.5. The result is microbunching at periods equal to the wavelength of the radiation. Bunched electrons have a higher current, and therefore produce higher intensity radiation in the bunch. The higher intensities lead to further bunching, and the result is exponential gain as the electron bunch

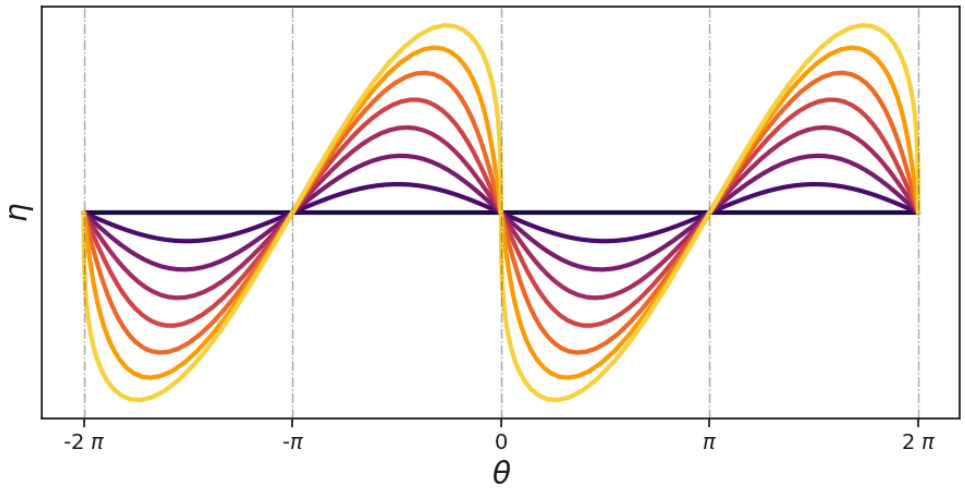



Figure 3.5: Evolution in $\theta$–$\eta$ phase space of an electron beam co-propagating in an undulator, calculated by integrating the pendulum equations for an electron beam initially at $\eta = 0$. Steps along the undulator go from black through orange to yellow. Microbunching occurs every $2\pi$ in $\theta$, at the zero-crossings of the electric field ($\psi_0 = \pi$).

propagates in the undulator. An important parameter for characterising a FEL is the Pierce parameter, $\rho_{\mathrm{p}}$ (conventionally unsubscripted, but with subscript here to avoid confusion with density), which is inversely proportional to the gain length of the FEL as well as the length to saturation. It can also be shown that the power conversion from the electron beam to X-rays is approximately $1.6\rho_{\mathrm{p}}$. For modern XFELS, $\rho_{\mathrm{p}} \sim 10^{-3}$. In the high gain regime, which is typical, the product of $\rho_{\mathrm{p}}$ and the number of undulator periods is comparable to 1 [42].

The initial co-propagating radiation which seeds the radiation must be resonant with the lasing of the undulators and electron bunch. The origin of this radiation is one of the major differences between XFEL architectures in use today. Seeded XFELs use radiation from a laser source. The advantage to this is that the XFEL output is characterised by the seed, and therefore typically has greater temporal coherence, and greater stability (for example, in the spectrum).

It is also possible to 'self-seed', which is to co-propagate radiation from an earlier undulator section, with the possibility of filtering the spectrum before hand. However, the brightest XFEL sources available today utilise the process of self-amplified spontaneous emission (SASE), which is amplification of broadband radiation resulting from the random shot noise in the electron bunch [43].

### 3.2.3 Development of XFELs for ultrafast science

Development of XFELs and advancement in scientific discovery using X-rays have driven each other in recent decades. In the remarkable brief paper by researchers at Stanford in 1977 [44], the first FEL was demonstrated, and produced NIR light at 3.4 µm; this followed the earlier theory work of Madey [45]. At the time, the motivation was to be able to generate high powers at tunable wavelengths. The first seeded FEL was seeded via a UV laser and was able to generate tunable picosecond UV pulses between 100 and 300 nm with millijoule energies, a source with clear applications in photochemistry. The demonstrated bunching of the electron current is exactly that described in Section 3.2.2.

The earliest theory to realise the potential for SASE came in the in the early 1980s, independently in the USSR [46] and in the USA [47]. In 1989, the first experimental demonstration was made in the millimetre wavelength regime [48]; and in 1999 SASE was demonstrated in the mid IR [49]; but it is the 2001 demonstration in the visible and UV at the Argonne National Laboratory [50] that is widely renowned as the first in the current line of experimental progress.

By 2006, dozens of FELs were operational, with and many more were planned [51], and the FLASH XFEL was open for users, providing gigawatt pulses between 13 and 30 nm [52, 53]. Although a few studies using FELs for applications based research can be found in earlier literature (early examples include the ablation of tissue [54] in the IR and nonlinear optics [55]), it was the opening of X-ray user facilities which allowed access to the broader community which led to the application-driven progress of the past 15 years. Early experiments utilised the unprecedented intensities in the X-ray regime for nonlinear processes, mainly multiphoton ionisation [56, 57, 58], but also the increased flux and femtosecond pulses allowing for coherent diffractive imaging before destruction [59].

When the LCLS facility opened in 2009 [60], not only did it provide angstrom wavelengths for hard X-ray science, but it gave the ultrafast science community access to few-femtosecond pulses [61] with 50 fs sychronisation to optical lasers [62]. Early experiments were again focussed on multiphoton ionisation, but now in the new regime of the femtosecond response of atoms [63] and molecules [64].

Chapter 2 highlighted the importance of charge coherence in the dynamics of matter, and one of the limiting factors in the applicability of XFEL pulses in ultrafast science is the coherence properties of the radiation. It was shown early on that SASE in the high gain regime will select a single transverse mode from an initially noisy distribution [65, 42], and therefore result in good spatial coherence. However, temporal coherence is less assured and is determined by the coherence length of the electron bunch [40],

$$L_{coh} \approx \frac{\lambda}{2\sqrt{\pi}\rho_{\mathrm{p}}}. \tag{3.13}$$

To a good approximation, within each coherence length of the electron bunch a single SASE spike is emitted; therefore the ratio of the electron bunch length and the coherence length gives the total number of SASE spikes. In the early operation of FLASH and LCLS, there were typically a few hundred emission spikes in each pulse. A second implication of this is that the overall temporal length of SASE pulses is limited by the length of the electron bunch.

Efforts to increase the temporal properties of XFEL pulses are therefore focused on controlling the electron bunch and lasing within it. This is a rapidly evolving field, which has seen great progress even over the relatively short timescale of this work. An early successful method for producing pulses of controllable temporal duration, down to 8 fs was the insertion of a slotted foil into the centre of a chicane bunch compressor [66]. Figure 3.6 demonstrates the working principles: The electron bunch is passed through a chicane bunch-compressor; at the centre of the bunch compressor, where the spatio-temporal tilt of the electron pulse is greatest, a slotted foil is inserted, typically made of aluminium. When the bunch passes through the foil, all but a small section of the bunch is Coulomb scattered and 'spoiled' such that it cannot lase efficiently. This has the effect of reducing the length of the electron bunch. The length of the electron bunch, and pulse, is proportional to the slit size. A consequence is that the total charge of the electron bunch is effectively reduced by the same fraction, although in [66], it is shown that the peak current remains constant down to a minimum slit size, at which very little benefit is gained from reducing the size further.

Today, the state-of-the-art for creating short pulses relies on enhanced SASE (eSASE), which

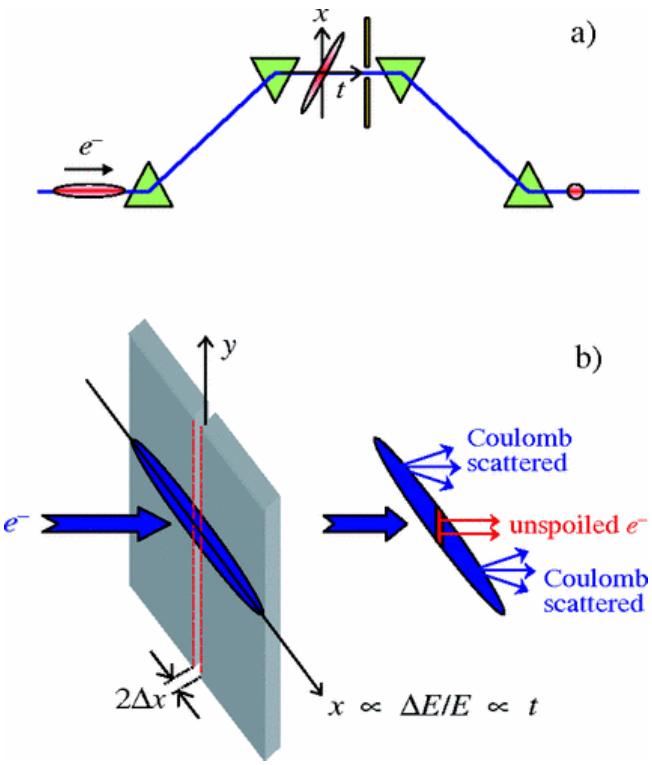



Figure 3.6: The working principle of the slotted foil technique for producing shorter-than 10 fs pulses. a) A sketch of the experimental layout, with a slotted foil placed with a bunch compressor (green), at the point where the electron bunch (red) is tilted forwards spatio-temporally. b) The effect of the slotted foil on the electron bunch, Coulomb scattering all but a small section of the bunch. Figure reproduced from [66] with permission of the license holder, APS.

despite only recently being implemented [67], was theorised already in 2005 [68]. The principal components of eSASE are an infrared beam overlapping longitudinally with the electron beam in a wiggler section and a following chicane. The infrared beam imparts a a sinusoidal energy modulation on the electron bunch's spatial distribution. The chicane is dispersive, i.e. low energy electrons follow a longer path and high energy electrons follow a short path, thus mapping the energy distribution of the bunch into space. This converts the sinusoidal distribution to sharp spikes of the electron density, at each of the zeros of the sinusoid. The origin of the infrared radiation in inconsequential, and the use of radiation generated by the electron bunch within the wiggler (as previously discussed, wigglers generate broadband, low frequency radiation) avoids the difficulties involved with synchronising the electron bunches with an external laser, so is generally preferred. Using this technique, pulses shorter than 500 as FWHM have been been generated and measured using angular streaking [67].

Aside from SASE based methods, there is also great potential for seeded XFELs in ultrafast

science. In 2011, the first seeded XFEL using high harmonic generation from a Ti:Saph laser was demonstrated [69]. However, as noted in that work, the intensity required to seed an XFEL is set by the intensity of spontaneous emission in the undulator and this imposes a limit on how high photon energies can be achieved. Today, the FERMI XFEL in Trieste, which is the the only major user facility using a seeded XFEL, is able to generate wavelengths as low as 4 nm. This is possible by seeding the XFEL with a higher wavelength (deep UV) and tuning the undulators to produce light at a harmonic of that wavelength [70]. In this way, excellent spectral stability and coherence is achieved; however it is not possible to reach the flux nor brightness of SASE based XFELS and the temporal properties are limited to those of the seed laser.

As discussed in Chapter 1, measurements in ultrafast science rely on the existence of a pump and a probe. Some spectroscopic methods use a pump and probe provided by the same pulse (for example HHG spectroscopy); however, it is mostly necessary to be able to provide two pulses, with a stable and controllable time delay between them. In XFELs, this has been achieved in a number of ways. A natural extension to the slotted foil method is to use a double-slotted foil, which leaves two temporally-separated portions of the electron beam unspoiled [71]. Each portion of the bunch is able to lase, and the delay between the two emitted X-ray pulses is determined by the chirp of the bunch and the separation of the slots. Due to the time-energy mapping of the electron bunch, the energy and time separation between the bunches is correlated, which is usually undesirable. This can be improved upon with the addition of a dispersive section added before the undulators [72], to control the time delays.

Another method is the 'split-undulator method', which uses two undulators, which can be tuned to different X-ray wavelengths (undulator $K$ values) within the chirp of the electron bunch, and adds delay to the electron bunch between the them [73]. Delay to the electrons is added by adding to their path, with the inclusion of a magnetic chicane. This has the benefit of individually tunable wavelengths; however, the pulse produced by the first undulator must always arrive first and there is a lower limit to the time delay achievable. It is also possible to produce two electron bunches, and to generate a pulse in each of them [74]. Provided the

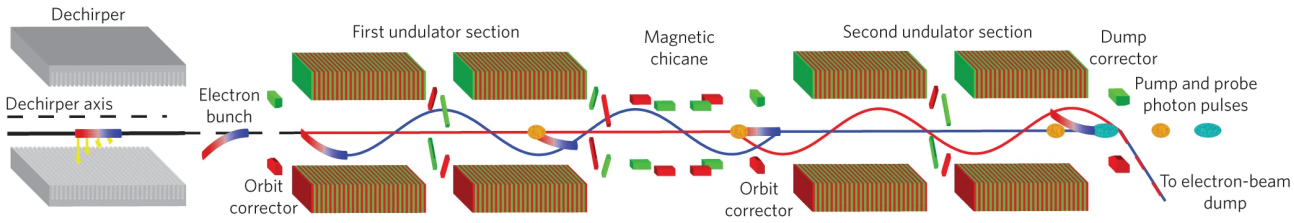



Figure 3.7: An overview of the fresh-slice method for producing two or more femtosecond pulses with variable time delay using and XFEL, as employed as LCLS for the pump-probe experiment in Chapter 4. The electron bunch is first modulated by a dechirper, 'kicking' the tail of the bunch transverse to its propagation. An orbit corrector is then used to control which portion of the bunch follows a straight trajectory in an undulator section, where the first pulse is generated (this pulse arrives last). A magnetic chicane then introduces the desirable amount of delay between the electron bunch and first X-ray pulse. Finally, a second orbit corrector selects a different portion of the bunch to follow a straight trajectory through a second undulator section, producing the second pulse. Figure reproduced from [75] with permission of the license holder, Spring Nature.

central photon energies are separated by a less than a few per cent, a single undulator can be used for both bunches.

In Chapter 4, the 'fresh-slice' method was employed at the LCLS XFEL to provide two X-ray pulses, with photon energy of approximately 499 eV and 514 eV, for a pump-probe experiment. The fresh-slice method is similar to the split-undulator method in that there are two (or more) different undulator sections, which can lase at different wavelengths [75]. It also draws inspiration from the double-slotted foil method, by manipulating the electron bunch to only allow lasing in a portion of the bunch.

An overview of the method is shown in Figure 3.7. The idea is to use a dechirper to introduce a time-dependent transverse spatial distribution to the bunch, which for a short bunch is approximately parabolic. The result is that the trajectories followed by the electrons depends on their position within the bunch. Then, exploiting the fact that lasing can only occur when the electrons follow a straight trajectory through the undulators, an orbit corrector is used to select only one 'slice' of the electron bunch to follow a straight through the first undulator section. This slice, which is very short, produces a few-femtosecond pulse. A different portion of the bunch (referred to as a 'fresh-slice') is selected to follow a straight in a second undulator section, and produces a second bunch. A magnetic chicane between the two undulator sections introduces a desired amount of delay to the electron bunch for control of the delay between

the final X-ray pulses. In contrast to the split-undulator method, the undulator sections can be operated in the saturation regime, allowing for higher intensity [75]. It is also possible to extend the method to the generation of three pulses.

XFELs are large and expensive tools, and are therefore only present at a handful of national facilities globally which are open for user experiments. They include:

- FERMI, Trieste, Italy
- FLASH, Hamburg, Germany
- European XFEL, Hamburg, Germany
- LCLS, California, USA
- PAL-XFEL, Pohang, South Korea
- SwissFEL, Villigen, Switzerland

The XFEL experiments described in this thesis have been exclusively using the LCLS XFEL. LCLS is currently undergoing a period of upgrade to LCLS-II. One of the main components of the upgrade is the installation of a superconducting linac, which will increase the repetition rate to $\sim$1 MHz, with a flux up to $10^{13}$ photons per pulse in the soft X-ray regime [76].

# References


[1] P. B. Corkum. Plasma perspective on strong field multiphoton ionization. *Physical Review Letters*, 71(13):1994–1997, sep 1993. ISSN 00319007. doi: 10.1103/PhysRevLett.71.1994. URL https://link.aps.org/doi/10.1103/PhysRevLett.71.1994.

[2] Howard R Reiss. EFFECT OF AN INTENSE ELECTROMAGNETIC-FIELD ON A WEAKLY BOUND SYSTEM. *Physical Review A*, 22(5): 1786–1813, 1980. ISSN 1050-2947. doi: 10.1103/PhysRevA.22.1786. URL https://journals-aps-org.iclibezp1.cc.ic.ac.uk/pra/pdf/10.1103/PhysRevA.22.1786papers3://publication/uuid/CC827472-12B6-4C59-96F6-4AA69C0EADAF.

[3] Manfred Lein. Attosecond probing of vibrational dynamics with high-harmonic generation. *Physical Review Letters*, 94(5), 2005. ISSN 00319007. doi: 10.1103/PhysRevLett.94.053004. URL https://journals-aps-org.iclibezp1.cc.ic.ac.uk/prl/pdf/10.1103/PhysRevLett.94.053004.

[4] M. Lewenstein, Ph. Balcou, M. Yu. Ivanov, Anne L'Huillier, and P. B. Corkum. Theory of high-harmonic generation by low-frequency laser fields. *Physical Review A*, 49(3): 2117–2132, mar 1994. ISSN 1050-2947. doi: 10.1103/PhysRevA.49.2117. URL https://link.aps.org/doi/10.1103/PhysRevA.49.2117.

[5] LV Keldysh. Ionization in the field of a strong electromagnetic wave. *Sov. Phys. JETP*, 20 (5):1307–1314, 1965. URL http://jetp.ac.ru/cgi-bin/dn/e{_}020{_}05{_}1307.pdf.

[6] F. H.M. Faisal. Multiple absorption of laser photons by atoms. *Journal of Physics B: Atomic and Molecular Physics*, 6(4):L89, apr 1973. ISSN 00223700. doi: 10.1088/0022-3700/6/4/011. URL https://iopscience.iop.org/article/10.1088/0022-3700/6/4/011https://iopscience.iop.org/article/10.1088/0022-3700/6/4/011/meta.

[7] S. V Popruzhenko. Keldysh theory of strong field ionization: History, applications, difficulties and perspectives. *Journal of Physics B: Atomic, Molecular and Optical Physics*, 47(20):204001, oct 2014. ISSN 13616455. doi: 10.1088/0953-4075/47/20/204001. URL

https://iopscience.iop.org/article/10.1088/0953-4075/47/20/204001https://iopscience.iop.org/article/10.1088/0953-4075/47/20/204001/meta.

[8] J. Tate, T. Auguste, H. G. Muller, P. Salières, P. Agostini, and L. F. Dimauro. Scaling of wave-packet dynamics in an intense midinfrared Field. *Physical Review Letters*, 98(1), 2007. ISSN 00319007. doi: 10.1103/PhysRevLett.98.013901.

[9] A D Shiner, C Trallero-Herrero, N Kajumba, H. C. Bandulet, D Comtois, F Légaré, M. Giguère, J. C. Kieffer, P B Corkum, and D M Villeneuve. Wavelength scaling of high harmonic generation efficiency. *Physical Review Letters*, 103(7), 2009. ISSN 00319007. doi: 10.1103/PhysRevLett.103.073902.

[10] Allan S. Johnson, Dane R. Austin, David A. Wood, Christian Brahms, Andrew Gregory, Konstantin B. Holzner, Sebastian Jarosch, Esben W. Larsen, Susan Parker, Christian S. Strüber, Peng Ye, John W.G. Tisch, and Jon P. Marangos. High-flux soft x-ray harmonic generation from ionization-shaped few-cycle laser pulses. *Science Advances*, 4(5):eaar3761, may 2018. ISSN 23752548. doi: 10.1126/sciadv.aar3761. URL http://advances.sciencemag.org/lookup/doi/10.1126/sciadv.aar3761.

[11] A. McPherson, G Gibson, H Jara, U Johann, T S Luk, I. A. McIntyre, K Boyer, and C K Rhodes. Studies of multiphoton production of vacuum-ultraviolet radiation in the rare gases. *Journal of the Optical Society of America B*, 4(4):595, 1987. ISSN 0740-3224. doi: 10.1364/josab.4.000595.

[12] M. Ferray, A. L'Huillier, X. F. Li, L. A. Lompre, G. Mainfray, and C. Manus. Multiple-harmonic conversion of 1064 nm radiation in rare gases. *Journal of Physics B: Atomic, Molecular and Optical Physics*, 21(3):L31, feb 1988. ISSN 09534075. doi: 10.1088/0953-4075/21/3/001.

[13] Nobuhiko Sarukura, Kiyoshi Hata, Takashi Adachi, Ryoichi Nodomi, Masayoshi Watanabe, and Shuntaro Watanabe. Coherent soft-x-ray generation by the harmonics of an ultrahigh-power KrF laser. *Physical Review A*, 43(3):1669–1672, feb 1991. ISSN 10502947. doi: 10.1103/PhysRevA.43.1669.

[14] J. J. Macklin, J. D. Kmetec, and C. L. Gordon. High-order harmonic generation using intense femtosecond pulses. *Physical Review Letters*, 70(6):766–769, feb 1993. ISSN 00319007. doi: 10.1103/PhysRevLett.70.766.

[15] Anne L'Huillier and Ph Balcou. High-order harmonic generation in rare gases with a 1-ps 1053-nm laser. *Physical Review Letters*, 70(6):774–777, 1993. ISSN 00319007. doi: 10.1103/PhysRevLett.70.774.

[16] Gy Farkas and Cs Tóth. Proposal for attosecond light pulse generation using laser induced multiple-harmonic conversion processes in rare gases. *Physics Letters A*, 168(5-6):447–450, sep 1992. ISSN 03759601. doi: 10.1016/0375-9601(92)90534-S.

[17] N. A. Papadogiannis, B. Witzel, C. Kalpouzos, and D. Charalambidis. Observation of attosecond light localization in higher order harmonic generation. *Physical Review Letters*, 83(21):4289–4292, jan 1999. ISSN 10797114. doi: 10.1103/PhysRevLett.83.4289. URL `https://journals.aps.org/prl/abstract/10.1103/PhysRevLett.83.4289`.

[18] M. Hentschel, R. Kienberger, Ch Spielmann, G. A. Reider, N. Milosevic, T. Brabec, P. Corkum, U. Heinzmann, M. Drescher, and F. Krausz. Attosecond metrology. *Nature*, 414 (6863):509–513, nov 2001. ISSN 00280836. doi: 10.1038/35107000. URL `www.nature.com`.

[19] M. Drescher, M. Hentschel, R. Kienberger, G. Tempea, C. Spielmann, G. A. Reider, P. B. Corkum, and F. Krausz. X-ray pulses approaching the attosecond frontier. *Science*, 291 (5510):1923–1927, mar 2001. ISSN 00368075. doi: 10.1126/science.1058561.

[20] Jie Li, Xiaoming Ren, Yanchun Yin, Kun Zhao, Andrew Chew, Yan Cheng, Eric Cunningham, Yang Wang, Shuyuan Hu, Yi Wu, Michael Chini, and Zenghu Chang. 53-attosecond X-ray pulses reach the carbon K-edge. *Nature Communications*, 8(1):1–5, dec 2017. ISSN 20411723. doi: 10.1038/s41467-017-00321-0. URL `www.nature.com/naturecommunications`.

[21] Francisco Silva, Stephan M. Teichmann, Seth L. Cousin, Michael Hemmer, and Jens Biegert. Spatiotemporal isolation of attosecond soft X-ray pulses in the water window. *Nature Communications*, 6(1):1–6, mar 2015. ISSN 20411723. doi: 10.1038/ncomms7611.

[22] C. A. Haworth, L. E. Chipperfield, J. S. Robinson, P. L. Knight, J. P. Marangos, and J. W G Tisch. Half-cycle cutoffs in harmonic spectra and robust carrier-envelope phase retrieval. *Nature Physics*, 3(1):52–57, 2007. ISSN 17452473. doi: 10.1038/nphys463.

[23] Andrius Baltuška, Takao Fuji, Takayoshi Kobayashi, Andrius Baltuska, Takao Fuji, and Takayoshi Kobayashi. Controlling the Carrier-Envelope Phase of Ultrashort Light Pulses with Optical Parametric Amplifiers. *Physical Review Letters*, 88(13): 133901, 2002. ISSN 0031-9007. doi: 10.1103/PhysRevLett.88.133901. URL `https://journals-aps-org.iclibezp1.cc.ic.ac.uk/prl/pdf/10.1103/PhysRevLett.88.133901http://link.aps.org/doi/10.1103/PhysRevLett.88.133901`.

[24] Leonardo Brugnera, David J Hoffmann, Thomas Siegel, Felix Frank, Amelle Zaïr, John W G Tisch, and Jonathan P Marangos. Trajectory selection in high harmonic generation by controlling the phase between orthogonal two-color fields. *Physical Review Letters*, 107(15), 2011. ISSN 00319007. doi: 10.1103/PhysRevLett.107.153902. URL `https://spiral.imperial.ac.uk/bitstream/10044/1/18903/2/PhysicalReviewLetters{_}107{_}15{_}2011.pdf`.

[25] Y. Mairesse, A. De Bohan, L. J. Frasinski, H. Merdji, L. C. Dinu, P. Monchicourt, P. Breger, M. Kovačev, R. Taïeb, B. Carré, H. G. Muller, P. Agostini, and P. Salières. Attosecond Synchronization of High-Harmonic Soft X-rays. *Science*, 302(5650):1540–1543, 2003. ISSN 00368075. doi: 10.1126/science.1090277. URL `http://science.sciencemag.org/content/sci/302/5650/1540.full.pdf`.

[26] S Baker, J S Robinson, C A Haworth, H Teng, R A Smith, C C Chirila, M Lein, J W G Tisch, and J P Marangos. Probing proton dynamics in molecules on an attosecond time scale. *Science (New York, N.Y.)*, 312(5772):424–7, apr 2006. ISSN 1095-9203. doi: 10.1126/science.1123904. URL `http://www.ncbi.nlm.nih.gov/pubmed/16513942`.

[27] M. Kotur, D. Guénot, Jiménez-Galán, D. Kroon, E. W. Larsen, M. Louisy, S. Bengtsson, M. Miranda, J. Mauritsson, C. L. Arnold, S. E. Canton, M. Gisselbrecht, T. Carette, J. M. Dahlström, E. Lindroth, A. Maquet, L. Argenti, F. Martín, and A. L'Huillier. Spectral phase

measurement of a Fano resonance using tunable attosecond pulses. *Nature Communications*, 7(1):1–6, feb 2016. ISSN 20411723. doi: 10.1038/ncomms10566.

[28] V Gruson, L Barreau, Jiménez-Galan, F Risoud, J Caillat, A Maquet, B Carré, F Lepetit, J. F. Hergott, T Ruchon, L Argenti, R Taïeb, F Martín, and P Salières. Attosecond dynamics through a Fano resonance: Monitoring the birth of a photoelectron. *Science*, 354(6313):734–738, nov 2016. ISSN 10959203. doi: 10.1126/science.aah5188. URL `http://www.ncbi.nlm.nih.gov/pubmed/27846602`.

[29] Yoann Pertot, Cédric Schmidt, Mary Matthews, Adrien Chauvet, Martin Huppert, Vit Svoboda, Aaron Von Conta, Andres Tehlar, Denitsa Baykusheva, Jean Pierre Wolf, and Hans Jakob Wörner. Time-resolved x-ray absorption spectroscopy with a water window high-harmonic source. *Science*, 355(6322):264–267, jan 2017. ISSN 10959203. doi: 10.1126/science.aah6114. URL `http://www.ncbi.nlm.nih.gov/pubmed/28059713`.

[30] Shambhu Ghimire, Anthony D. Dichiara, Emily Sistrunk, Pierre Agostini, Louis F. Dimauro, and David A. Reis. Observation of high-order harmonic generation in a bulk crystal. *Nature Physics*, 7(2):138–141, dec 2011. ISSN 17452481. doi: 10.1038/nphys1847.

[31] Anthony D. DiChiara, Emily Sistrunk, Terry A. Miller, Pierre Agostini, and Louis F. DiMauro. An investigation of harmonic generation in liquid media with a mid-infrared laser. *Optics Express*, 17(23):20959, nov 2009. ISSN 1094-4087. doi: 10.1364/oe.17.020959. URL `https://www.osapublishing.org/oe/abstract.cfm?uri=oe-17-23-20959`.

[32] Heiko G. Kurz, Daniel S. Steingrube, Detlev Ristau, Manfred Lein, Uwe Morgner, and Milutin Kovačev. High-order-harmonic generation from dense water microdroplets. *Physical Review A - Atomic, Molecular, and Optical Physics*, 87(6):063811, jun 2013. ISSN 10502947. doi: 10.1103/PhysRevA.87.063811. URL `https://link.aps.org/doi/10.1103/PhysRevA.87.063811`.

[33] T. T. Luu, M. Garg, S. Yu. Kruchinin, A. Moulet, M. Th Hassan, and E. Goulielmakis. Extreme ultraviolet high-harmonic spectroscopy of solids. *Nature*, 521(7553):498–502, may 2015. ISSN 14764687. doi: 10.1038/nature14456.

[34] Yong Sing You, David A. Reis, and Shambhu Ghimire. Anisotropic high-harmonic generation in bulk crystals. *Nature Physics*, 13(4):345–349, apr 2017. ISSN 17452481. doi: 10.1038/nphys3955.

[35] Tran Trung Luu, Zhong Yin, Arohi Jain, Thomas Gaumnitz, Yoann Pertot, Jun Ma, and Hans Jakob Wörner. Extreme–ultraviolet high–harmonic generation in liquids. *Nature Communications*, 9(1):1–10, dec 2018. ISSN 20411723. doi: 10.1038/s41467-018-06040-4.

[36] Shima Gholam-Mirzaei, John E. Beetar, Alexis Chacón, and Michael Chini. High-harmonic generation in ZnO driven by self-compressed mid-infrared pulses. *Journal of the Optical Society of America B*, 35(4):A27, apr 2018. ISSN 0740-3224. doi: 10.1364/josab.35.000a27.

[37] Chuan Yu, Kenneth K. Hansen, and Lars Bojer Madsen. High-order harmonic generation in imperfect crystals. *Physical Review A*, 99(6):063408, jun 2019. ISSN 24699934. doi: 10.1103/PhysRevA.99.063408.

[38] H. Lakhotia, H. Y. Kim, M. Zhan, S. Hu, S. Meng, and E. Goulielmakis. Laser picoscopy of valence electrons in solids. *Nature*, 583(7814):55–59, jul 2020. ISSN 14764687. doi: 10.1038/s41586-020-2429-z. URL `https://doi.org/10.1038/s41586-020-2429-z`.

[39] Donald H Bilderback, Pascal Elleaume, and Edgar Weckert. Review of third and next generation synchrotron light sources. *Journal of Physics B: Atomic, Molecular and Optical Physics*, 38(9):S773–S797, may 2005. ISSN 09534075. doi: 10.1088/0953-4075/38/9/022. URL `http://stacks.iop.org/0953-4075/38/i=9/a=022?key=crossref.fff50e96d91376df49e03a0a29977070`.

[40] Kwang-Je Kim, Zhirong Huang, and Ryan Lindberg. *Synchrotron Radiation and Free-Electron Lasers*. Cambridge University Press, 2017. ISBN 9781107162617. doi: 10.1017/9781316677377. URL `https://www.cambridge.org/core/books/synchrotron-radiation-and-freeelectron-lasers/F90638BB364B5A3EF9A78978CE15B1A5`.

[41] Zhirong Huang and Kwang Je Kim. Review of x-ray free-electron laser theory. *Physical*

*Review Special Topics - Accelerators and Beams*, 10(3), 2007. ISSN 10984402. doi: 10.1103/PhysRevSTAB.10.034801.

[42] Kwang Je Kim. Three-dimensional analysis of coherent amplification and self-amplified spontaneous emission in free-electron lasers. *Physical Review Letters*, 57(15):1871–1874, 1986. ISSN 00319007. doi: 10.1103/PhysRevLett.57.1871.

[43] R Bonifacio, L De Salvo, P Pierini, N Piovella, and C. Pellegrini. Spectrum, temporal structure, and fluctuations in a high-gain free-electron laser starting from noise. *Physical Review Letters*, 73(1):70–73, 1994. ISSN 00319007. doi: 10.1103/PhysRevLett.73.70.

[44] D. A.G. Deacon, L. R. Elias, J. M.J. Madey, G. J. Ramian, H. A. Schwettman, and T. I. Smith. First operation of a free-electron laser. *Physical Review Letters*, 38(16): 892–894, apr 1977. ISSN 00319007. doi: 10.1103/PhysRevLett.38.892. URL `https://journals.aps.org/prl/abstract/10.1103/PhysRevLett.38.892`.

[45] John M.J. Madey. Stimulated emission of bremsstrahlung in a periodic magnetic field. *Journal of Applied Physics*, 42(5):1906–1913, 1971. ISSN 00218979. doi: 10.1063/1.1660466.

[46] A M Kondratenko and E L Saldin. GENERATION OF COHERENT RADIATION BY A RELATIVISTIC ELECTRON BEAM IN AN ONDULATOR. *Particle accelerators Print*, 10(3-4):207–216, 1980. ISSN 00312460.

[47] R. Bonifacio, C. Pellegrini, and L. M. Narducci. COLLECTIVE INSTABILITIES AND HIGH-GAIN REGIME FREE ELECTRON LASER. In *AIP Conference Proceedings*, number 118, pages 236–259. AIP, 1984. ISBN 088318317X. doi: 10.1063/1.34640.

[48] D. A. Kirkpatrick, G. Bekefi, A. C. DiRienzo, H. P. Freund, and A. K. Ganguly. A millimeter and submillimeter wavelength free-electron laser. *Physics of Fluids B*, 1(7): 1511–1518, 1989. ISSN 08998221. doi: 10.1063/1.858927.

[49] M J Hogan, C Pellegrini, J Rosenzweig, S Anderson, P Frigola, A Tremaine, C Fortgang, D C Nguyen, R L Sheffield, J Kinross-Wright, A. Varfolomeev, A A Varfolomeev, S Tolmachev, and Roger Carr. Measurements of gain larger than 105 at 12$\mu$m in a self-amplified

spontaneous-emission free-electron laser. *Physical Review Letters*, 81(22):4867–4870, 1998. ISSN 10797114. doi: 10.1103/PhysRevLett.81.4867.

[50] S. V. Milton, E. Gluskin, N. D. Arnold, C. Benson, W. Berg, S. G. Biedron, M. Borland, Y. C. Chae, R. J. Dejus, P. K. Den Hartog, B. Deriy, M. Erdmann, Y. I. Eidelman, M. W. Hahne, Z. Huang, K. J. Kim, J. W. Lewellen, Y. Li, A. H. Lumpkin, O. Makarov, E. R. Moog, A. Nassiri, V. Sajaev, R. Soliday, B. J. Tieman, E. M. Trakhtenberg, G. Travish, I. B. Vasserman, N. A. Vinokurov, X. J. Wang, G. Wiemerslage, and B. X. Yang. Exponential gain and saturation of a self-amplified spontaneous emission free-electron laser. *Science*, 292(5524):2037–2041, jun 2001. ISSN 00368075. doi: 10.1126/science.1059955.

[51] W B Colson, J Blau, and A Kampouridis. Free electron lasers in 2006. In *28th International Free Electron Laser Conference, FEL 2006*, pages 756–760, 2006. URL `http://sbfel3.ucsb.edu/www/vl{_}fel.html`.

[52] V Ayvazyan, N Baboi, J Bähr, V Balandin, B Beutner, A Brandt, I Bohnet, A Bolzmann, R Brinkmann, O I Brovko, J P Carneiro, S Casalbuoni, M Castellano, P Castro, L Catani, E Chiadroni, S Choroba, A Cianchi, H Delsim-Hashemi, G. di Pirro, M Dohlus, S Düsterer, H T Edwards, B Faatz, A A Fateev, J Feldhaus, K Flöttmann, J Frisch, L Fröhlich, T Garvey, U Gensch, N Golubeva, H. J. Grabosch, B Grigoryan, O Grimm, U Hahn, J H Han, M V Hartrott, K Honkavaara, M Hüning, R Ischebeck, E Jaeschke, M Jablonka, R Kammering, V Katalev, B Keitel, S Khodyachykh, Y Kim, V Kocharyan, M Körfer, M Kollewe, D Kostin, D Krämer, M Krassilnikov, G Kube, L Lilje, T Limberg, D Lipka, F Löhl, M Luong, C Magne, J Menzel, P Michelato, V Miltchev, M Minty, W D Möller, L Monaco, W Müller, M Nagl, O Napoly, P Nicolosi, D Nölle, T Nuñez, A Oppelt, C Pagani, R Paparella, B Petersen, B Petrosyan, J Pflüger, P Piot, E Plönjes, L Poletto, D Proch, D Pugachov, K Rehlich, D Richter, S Riemann, M Ross, J Rossbach, M Sachwitz, E L Saldin, W Sandner, H Schlarb, B Schmidt, M Schmitz, P Schmüser, J R Schneider, E A Schneidmiller, H. J. Schreiber, S Schreiber, A V Shabunov, D Sertore, S Setzer, S Simrock, E Sombrowski, L Staykov, B Steffen, F Stephan, F Stulle, K P Sytchev, H Thom, K Tiedtke, M Tischer, R Treusch, D Trines, I Tsakov, A Vardanyan, R Wanzenberg, T Weiland, H Weise,

M Wendt, I Will, A Winter, K Wittenburg, M V Yurkov, I Zagorodnov, P Zambolin, and K Zapfe. First operation of a free-electron laser generating GW power radiation at 32 nm wavelength. *European Physical Journal D*, 37(2):297–303, 2006. ISSN 14346079. doi: 10.1140/epjd/e2005-00308-1.

[53] H Schlarb. FLASH UPGRADED-PREPARING FOR THE EUROPEAN XFEL.

[54] Glenn Edwards, Regan Logan, Michael Copeland, Lou Reinisch, Jeffrey Davidson, Bruce Johnson, Robert Maciunas, Marcus Mendenhall, Robert Ossoff, Jerri Tribble, Jay Werkhaven, and Denis O'Day. Tissue ablation by a free-electron laser tuned to the amide II band. *Nature*, 371(6496):416–419, 1994. ISSN 00280836. doi: 10.1038/371416a0. URL `https://www.nature.com/articles/371416a0`.

[55] E Tuncel, J L Staehli, C Coluzza, G Margaritondo, J. T. McKinley, R G Albridge, A V Barnes, A Ueda, X Yang, and N H Tolk. Free-electron laser studies of direct and indirect two-photon absorption in germanium. *Physical Review Letters*, 70(26):4146–4149, 1993. ISSN 00319007. doi: 10.1103/PhysRevLett.70.4146.

[56] H Wabnitz, L Bittner, A. R.B. De Castro, R. Döhrmann, P. Gürtler, T Laarmann, W Laasch, J Schulz, A Swiderski, K. Von Haeften, T. Möller, B Faatz, A Fateev, J Feldhaus, C Gerth, U Hahn, E Saldin, E Schneidmiller, K Sytchev, K Tiedtke, R Treusch, and M. Yurkov. Multiple ionization of atom clusters by intense soft X-rays from a free-electron laser. *Nature*, 420(6915):482–485, 2002. ISSN 00280836. doi: 10.1038/nature01197. URL `www.nature.com/nature`.

[57] M Meyer, D Cubaynes, P. O'Keeffe, H Luna, P Yeates, E T Kennedy, J T Costello, P Orr, R Taïeb, A Maquet, S Düsterer, P Radcliffe, H Redlin, A Azima, E Plönjes, and J Feldhaus. Two-color photoionization in xuv free-electron and visible laser fields. *Physical Review A - Atomic, Molecular, and Optical Physics*, 74(1), 2006. ISSN 10502947. doi: 10.1103/PhysRevA.74.011401.

[58] A. A. Sorokin, S. V. Bobashev, K. Tiedtke, and M. Richter. Multi-photon ionization of molecular nitrogen by femtosecond soft x-ray FEL pulses. *Journal of Physics B: Atomic, Molecular*

*and Optical Physics*, 39(14):L299, jun 2006. ISSN 09534075. doi: 10.1088/0953-4075/39/14/L04. URL https://iopscience.iop.org/article/10.1088/0953-4075/39/14/L04https://iopscience.iop.org/article/10.1088/0953-4075/39/14/L04/meta.

[59] Henry N Chapman, Anton Barty, Michael J Bogan, Sébastien Boutet, Matthias Frank, Stefan P Hau-Riege, Stefano Marchesini, Bruce W Woods, Saša Bajt, W Henry Benner, Richard A London, Elke Plönjes, Marion Kuhlmann, Rolf Treusch, Stefan Düsterer, Thomas Tschentscher, Jochen R Schneider, Eberhard Spiller, Thomas Möller, Christoph Bostedt, Matthias Hoener, David A Shapiro, Keith O Hodgson, David Van Der Spoel, Florian Burmeister, Magnus Bergh, Carl Caleman, Gösta Huldt, M Marvin Seibert, Filipe R.N.C. Maia, Richard W Lee, Abraham Szöke, Nicusor Timneanu, and Janos Hajdu. Femtosecond diffractive imaging with a soft-X-ray free-electron laser. *Nature Physics*, 2(12):839–843, 2006. ISSN 17452481. doi: 10.1038/nphys461. URL www.nature.com/naturephysics.

[60] P Emma, R Akre, J Arthur, R Bionta, C Bostedt, J Bozek, A Brachmann, P Bucksbaum, R Coffee, F. J. Decker, Y Ding, D Dowell, S Edstrom, A Fisher, J Frisch, S Gilevich, J Hastings, G Hays, Ph Hering, Z Huang, R Iverson, H Loos, M Messerschmidt, A Miahnahri, S Moeller, H. D. Nuhn, G Pile, D Ratner, J Rzepiela, D Schultz, T Smith, P Stefan, H Tompkins, J Turner, J Welch, W White, J Wu, G Yocky, and J Galayda. First lasing and operation of an ångstrom-wavelength free-electron laser. *Nature Photonics*, 4(9):641–647, 2010. ISSN 17494885. doi: 10.1038/nphoton.2010.176. URL http://www.nature.com.iclibezp1.cc.ic.ac.uk/articles/nphoton.2010.176.pdf.

[61] Y Ding, A Brachmann, F. J. Decker, D Dowell, P Emma, J Frisch, S Gilevich, G Hays, Ph Hering, Z Huang, R Iverson, H Loos, A Miahnahri, H. D. Nuhn, D Ratner, J Turner, J Welch, W White, and J Wu. Measurements and simulations of ultralow emittance and ultrashort electron beams in the linac coherent light source. *Physical Review Letters*, 102 (25), 2009. ISSN 00319007. doi: 10.1103/PhysRevLett.102.254801.

[62] A Brachmann, C Bostedt, J Bozek, R Coffee, F. J. Decker, Y Ding, D Dowell, P Emma, J Frisch, S Gilevich, G Haller, G Hays, Ph Hering, B Hill, Z Huang, R Iverson, E Kanter, B Kraessig, H Loos, A Miahnahri, H. D. Nuhn, A Perazzo, M Petree, D Ratner, R Santra,

T Smith, S Southworth, J Turner, J Welch, W White, J Wu, L Young, J. M. Byrd, G. Huang, and R. Wilcox. Femtosecond operation of the LCLS for user experiments. In *IPAC 2010 - 1st International Particle Accelerator Conference*, pages 2287–2289, 2010. ISBN 9789290833529.

[63] L Young, E P Kanter, B. Kräsignssig, Y Li, A M March, S T Pratt, R Santra, S H Southworth, N Rohringer, L F Dimauro, G Doumy, C A Roedig, N Berrah, L Fang, M Hoener, P H Bucksbaum, J P Cryan, S Ghimire, J M Glownia, D A Reis, J D Bozek, C Bostedt, and M. Messerschmidt. Femtosecond electronic response of atoms to ultra-intense X-rays. *Nature*, 466(7302):56–61, 2010. ISSN 00280836. doi: 10.1038/nature09177.

[64] James P. Cryan, J. M. Glownia, J. Andreasson, A. Belkacem, N. Berrah, C. I. Blaga, C. Bostedt, J. Bozek, C. Buth, L. F. Dimauro, L. Fang, O. Gessner, M. Guehr, J. Hajdu, M. P. Hertlein, M. Hoener, O. Kornilov, J. P. Marangos, A. M. March, B. K. McFarland, H. Merdji, V. S. Petrović, C. Raman, D. Ray, D. Reis, F. Tarantelli, M. Trigo, J. L. White, W. White, L. Young, P. H. Bucksbaum, and R. N. Coffee. Auger electron angular distribution of double core-hole states in the molecular reference frame. *Physical Review Letters*, 105(8):083004, aug 2010. ISSN 00319007. doi: 10.1103/PhysRevLett.105.083004. URL `https://journals.aps.org/prl/abstract/10.1103/PhysRevLett.105.083004`.

[65] E. L. Saldin, E. A. Schneidmiller, and M. V. Yurkov. Coherence properties of the radiation from X-ray free electron laser. *Optics Communications*, 281(5):1179–1188, mar 2008. ISSN 00304018. doi: 10.1016/j.optcom.2007.10.044.

[66] P Emma, K Bane, M Cornacchia, Z Huang, H Schlarb, G Stupakov, and D Walz. Femtosecond and Subfemtosecond X-Ray Pulses from a Self-Amplified Spontaneous-Emission–Based Free-Electron Laser. *Physical Review Letters*, 92(7), 2004. ISSN 10797114. doi: 10.1103/PhysRevLett.92.074801.

[67] Joseph Duris, Siqi Li, Taran Driver, Elio G. Champenois, James P. MacArthur, Alberto A. Lutman, Zhen Zhang, Philipp Rosenberger, Jeff W. Aldrich, Ryan Coffee, Giacomo Coslovich, Franz Josef Decker, James M. Glownia, Gregor Hartmann, Wolfram Helml,

Andrei Kamalov, Jonas Knurr, Jacek Krzywinski, Ming Fu Lin, Jon P. Marangos, Megan Nantel, Adi Natan, Jordan T. O'Neal, Niranjan Shivaram, Peter Walter, Anna Li Wang, James J. Welch, Thomas J.A. Wolf, Joseph Z. Xu, Matthias F. Kling, Philip H. Bucksbaum, Alexander Zholents, Zhirong Huang, James P. Cryan, and Agostino Marinelli. Tunable isolated attosecond X-ray pulses with gigawatt peak power from a free-electron laser. *Nature Photonics*, 14(1):30–36, jan 2020. ISSN 17494893. doi: 10.1038/s41566-019-0549-5.

[68] Alexander A. Zholents. Method of an enhanced self-amplified spontaneous emission for x-ray free electron lasers. *Physical Review Special Topics - Accelerators and Beams*, 8 (4):8–13, apr 2005. ISSN 10984402. doi: 10.1103/PhysRevSTAB.8.040701. URL `https://journals.aps.org/prab/abstract/10.1103/PhysRevSTAB.8.040701`.

[69] Tadashi Togashi, Eiji J. Takahashi, Katsumi Midorikawa, Makoto Aoyama, Koichi Yamakawa, Takahiro Sato, Atsushi Iwasaki, Shigeki Owada, Tomoya Okino, Kaoru Yamanouchi, Fumihiko Kannari, Akira Yagishita, Hidetoshi Nakano, Marie E Couprie, Kenji Fukami, Takaki Hatsui, Toru Hara, Takashi Kameshima, Hideo Kitamura, Noritaka Kumagai, Shinichi Matsubara, Mitsuru Nagasono, Haruhiko Ohashi, Takashi Ohshima, Yuji Otake, Tsumoru Shintake, Kenji Tamasaku, Hitoshi Tanaka, Takashi Tanaka, Kazuaki Togawa, Hiromitsu Tomizawa, Takahiro Watanabe, Makina Yabashi, and Tetsuya Ishikawa. Extreme ultraviolet free electron laser seeded with high-order harmonic of Ti:sapphire laser. *Optics Express*, 19(1):317, jan 2011. ISSN 1094-4087. doi: 10.1364/oe.19.000317. URL `https://opg.optica.org/viewmedia.cfm?uri=oe-19-1-317{&}seq=0{&}html=truehttps://opg.optica.org/abstract.cfm?uri=oe-19-1-317https://opg.optica.org/oe/abstract.cfm?uri=oe-19-1-317`.

[70] Paola Finetti, Hauke Höppner, Enrico Allaria, Carlo Callegari, Flavio Capotondi, Paolo Cinquegrana, Marcello Coreno, Riccardo Cucini, Miltcho B. Danailov, Alexander Demidovich, Giovanni De Ninno, Michele Di Fraia, Raimund Feifel, Eugenio Ferrari, Lars Fröhlich, David Gauthier, Torsten Golz, Cesare Grazioli, Yun Kai, Gabor Kurdi, Nicola Mahne, Michele Manfredda, Nikita Medvedev, Ivaylo P. Nikolov, Emanuele Pedersoli, Giuseppe Penco, Oksana Plekan, Mark J. Prandolini, Kevin C. Prince, Lorenzo Raimondi,

Primoz Rebernik, Robert Riedel, Eleonore Roussel, Paolo Sigalotti, Richard Squibb, Nikola Stojanovic, Stefano Stranges, Cristian Svetina, Takanori Tanikawa, Ulrich Teubner, Victor Tkachenko, Sven Toleikis, Marco Zangrando, Beata Ziaja, Franz Tavella, and Luca Giannessi. Pulse duration of seeded free-electron lasers, jun 2017. ISSN 21603308. URL https://journals.aps.org/prx/abstract/10.1103/PhysRevX.7.021043.

[71] Y. Ding, C. Behrens, R. Coffee, F. J. Decker, P. Emma, C. Field, W. Helml, Z. Huang, P. Krejcik, J. Krzywinski, H. Loos, A. Lutman, A. Marinelli, T. J. Maxwell, and J. Turner. Generating femtosecond X-ray pulses using an emittance-spoiling foil in free-electron lasers. *Applied Physics Letters*, 107(19):191104, nov 2015. ISSN 00036951. doi: 10.1063/1.4935429. URL https://aip.scitation.org/doi/abs/10.1063/1.4935429.

[72] Ángela Saá Hernández, Eduard Prat, and Sven Reiche. Generation of two-color x-ray free-electron-laser pulses from a beam with a large energy chirp and a slotted foil. *Physical Review Accelerators and Beams*, 22(3), 2019. ISSN 24699888. doi: 10.1103/PhysRevAccelBeams.22.030702.

[73] A A Lutman, R Coffee, Y Ding, Z Huang, J Krzywinski, T Maxwell, M Messerschmidt, and H. D. Nuhn. Experimental demonstration of femtosecond two-color X-ray free-electron lasers. *Physical Review Letters*, 110(13), 2013. ISSN 00319007. doi: 10.1103/PhysRevLett.110.134801.

[74] A. Marinelli, D. Ratner, A. A. Lutman, J. Turner, J. Welch, F. J. Decker, H. Loos, C. Behrens, S. Gilevich, A. A. Miahnahri, S. Vetter, T. J. Maxwell, Y. Ding, R. Coffee, S. Wakatsuki, and Z. Huang. High-intensity double-pulse X-ray free-electron laser. *Nature Communications*, 6(1):1–6, mar 2015. ISSN 20411723. doi: 10.1038/ncomms7369. URL https://www.nature.com/articles/ncomms7369https://www.nature.com/articles/ncomms7369/.

[75] Alberto A Lutman, Timothy J Maxwell, James P. MacArthur, Marc W Guetg, Nora Berrah, Ryan N Coffee, Yuantao Ding, Zhirong Huang, Agostino Marinelli, Stefan Moeller, and Johann C.U. Zemella. Fresh-slice multicolour X-ray free-electron lasers. *Nature*

*Photonics*, 10(11):745–750, 2016. ISSN 17494893. doi: 10.1038/nphoton.2016.201. URL www.nature.com/naturephotonics.

[76] John N Galayda. The Linac Coherent Light Source-II Project. In *International Particle Accelerator Conference 2014 (IPAC14)*, pages 935–937, 2014. ISBN 9783954501328. doi: 10.2172/815259. URL http://accelconf.web.cern.ch/AccelConf/IPAC2014/papers/tuoca01.pdf?n=IPAC2014/papers/tuoca01.pdfhttp://www.osti.gov/servlets/purl/815259-wPPZYZ/native/.

# Chapter 4

# Relaxation of inner valence holes in isopropanol cations

Chapter 2 introduces the effects of correlations on the energetics of molecular eigenstates. In particular, Section 2.2.1 introduces the concept of the breakdown of the molecular orbital picture of ionisation resulting from charge correlations, which can be understood by configuration interactions to be the result of coupling between one-hole and two-hole-one-particle states. The result is that the sudden excitation of an inner valence electron, which in the ground state is well approximated as a Slater determinant of Hartree-Fock orbitals, into the continuum, does not leave the molecule in a pure one-hole state of the cation

Therefore, ionisation of an inner valence electron creates an inner valence hole (IVH) with a wavefunction consisting of a superposition of valence hole eigenstates. The dynamics which follow can be understood from basic quantum theory describing the unitary evolution of a quantum state. Each state, $|\psi\rangle$ of energy eigenvalue $E$ evolves according to

$$|\psi(0,t)\rangle = e^{-iEt/\hbar}\,|\psi\rangle\,. \tag{4.1}$$

The exponents of a coherent superposition of states with different energies will dephase on a timescale inversely proportional to their energetic spread. This is a result familiar to many

areas of physics, such as molecular rotation and alignment. The simplest case is a coherent superposition of two states with energy separation $\Delta E$,

$$|\psi(0,t)\rangle = e^{-iE_0 t/\hbar}|\psi_0\rangle + e^{-i(E_0+\Delta E)t/\hbar}|\psi_1\rangle \tag{4.2}$$

$$= e^{-iE_0 t/\hbar}\left(|\psi_0\rangle + e^{-i\Delta E t/\hbar}|\psi_1\rangle\right). \tag{4.3}$$

Beating occurs with period $\hbar/\Delta E$. A 1 meV energy separation beats with a 4.14 ps period, and a 1 eV separation with a 4.14 fs period.

The energetic spread an inner valence hole wavepacket is typically a few eV and charge dynamics therefore occur on the sub- to few-femtosecond timescale. The rapidity of this effect is derived from the fact that it is a purely electronic rearrangement of charge, and is referred to as charge migration. It is a different phenomenon from charge transfer, which is driven by the non-adiabatic coupling of electronic and nuclear degrees of freedom. That is not to say that nuclear motion does not affect charge migration and, as will be shown, it indeed has significant impact, but the process is not reliant on nuclear motion.

Section 2.2.1 notes the early theoretical works of the 70s and early 80s in the role of charge correlations on ionisation. It wasn't until the later theoretical work of Cederbaum and Zelensky [1] that the implications of this on ultrafast charge migration were studied explicitly. There, it is shown that charge will migrate along the carbon chain of difluoropropadienone. It has also been suggested that there is a 'universal' charge migration occurring in the first 50 as following the removal of an electron [2].

Charge migration is dependent on the initial energies and coherences of the eigenstates which make up the wavepacket; consequently, the nuclear geometry of a molecule affects charge migration following ionisation. One case where this becomes important is in the different conformers of a molecule, for example in Glycine where the three most common conformers in the gas phase were shown to have significantly different charge migration following ionisation [3]. It has also been shown that it is important to account for the fact that, even for a single conformer, nuclei at the time of ionisation are distributed in space – the so-called zero point

energy spread. The zero point energy spread alters the energy eigenvalues of the valence hole and results in decoherence between the spread of nuclear arrangements. This has been studied in the mixing of one-hole states in the outer valence [4, 5, 6] and is equally valid in the case of one-hole mixing with two-hole-one particle states in the inner valence. Furthermore, any hole population surviving on a timescale comparable to nuclear motion will also decohere [7, 4], and it has been suggested that nuclear motion could play a role in the trapping of charge following charge migration in a two-step process [8].

The modelling of charge migration is complex and computationally expensive on several counts. Firstly, the inclusion of charge correlations required to calculate the energies and wavefunctions of the coupled states greatly increases the dimension of the problem - even more so if higher order couplings are to be considered.

Secondly, the initial choice of populations making up the hole wavepacket is not clear, and there exists no complete theory for calculating this. Of particular difficulty is calculating the interaction of the electron which is leaving the molecule during the ionisation step and the remaining cation. As such, the sudden approximation must be invoked and this is only valid in the sudden ionisation limit, which is the limit that the electron leaves the cation before the electrons remaining in the cation can react [8]. Referring again to the universal charge migration happening in the first 50 as [2], this indicates that the electron must have sufficient kinetic energy to leave in the first 50 as.

Thirdly, the inclusion of the zero-point spread in the nuclear geometries again greatly increases the computational cost. Practically, it requires any calculation to be repeated for a spread in initial nuclear geometries and then summed, with the number of geometries increased until convergence is found. Finally, including the nuclear motion again greatly increases the dimension of the problem [6]. To date, no simulations exist in literature which account for all of these effects and such a calculation is beyond the current state-of-the-art in quantum chemistry. Experimental observations of charge migration therefore form an exciting benchmark for new theory and motivation to improve on current methods.

Isopropanol is highly suitable for observing these hole migration effects. This organic molecule

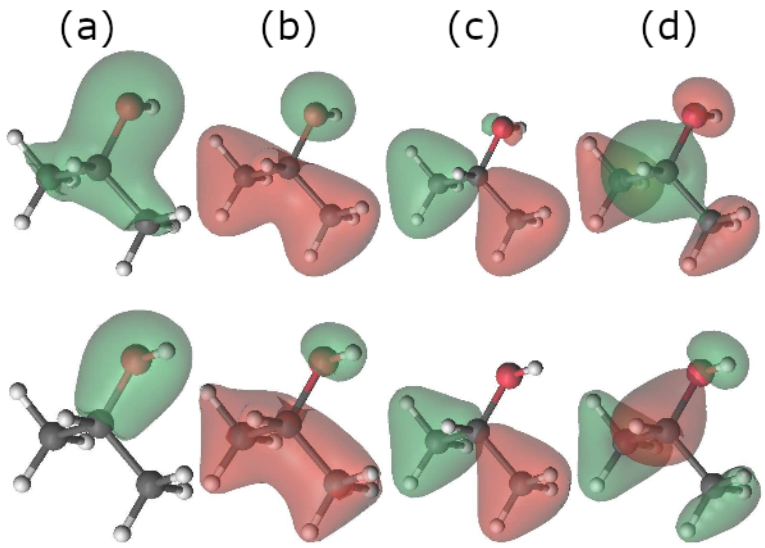



Figure 4.1: (top row) Hartree-Fock orbitals of the *anti* conformer of isopropanol. Carbon, oxygen, and hydrogen atoms are respectively depicted as black, red, and white spheres. From left to right: (a) Density concentrated on the oxygen centre and in the sigma C-C bonds; (b) Nodal plane through O-C bond; (c) Nodal plane along mirror plane (through HOCH); (d) Three nodal planes through terminal C atoms and through O atom (bottom row) Hartree-Fock orbitals of the *gauche* conformer of isopropanol. As in *anti*, but with less mixing of Oxygen orbitals with the sigma C-C bonds noticeable in (a) and (c). Image credit: Bridgette Cooper

is of sufficient size for there to be non-trivial evolution of a suddenly excited superposition of inner valence hole states. In this molecular cation a range of hole dynamics of different types in a single experiment may be accessible. Isopropanol exists in two conformers, *anti* and *gauche*. These two conformers and their corresponding inner valence holes of a-type symmetry, 5a, 6a, 7a, and 8a, are shown in Figure 4.1. The 6a, 7a, and 8a states lie below the double ionisation potential, whilst the 5a state lies above it. Given that the oxygen 1s binding energy is 538.5 eV, their resonances for core-hole excitation from the oxygen 1s are approximately 519.5 eV, 516.5 eV, 515 eV, and 508 eV.

Figure 4.2 shows the spectral intensity plots for each of the conformers of isopropanol. Evidence of electron correlations is already present in the splitting of what would otherwise be single peaks into many satellites. The major difference between the two conformers is in the green hole (the "s" of the carbon). The increased symmetry in the *anti* conformer means that the two carbons on either side of the molecule in the same environment; there is no energy splitting, and in general there is less mixing of any of one-hole-one-hole type.

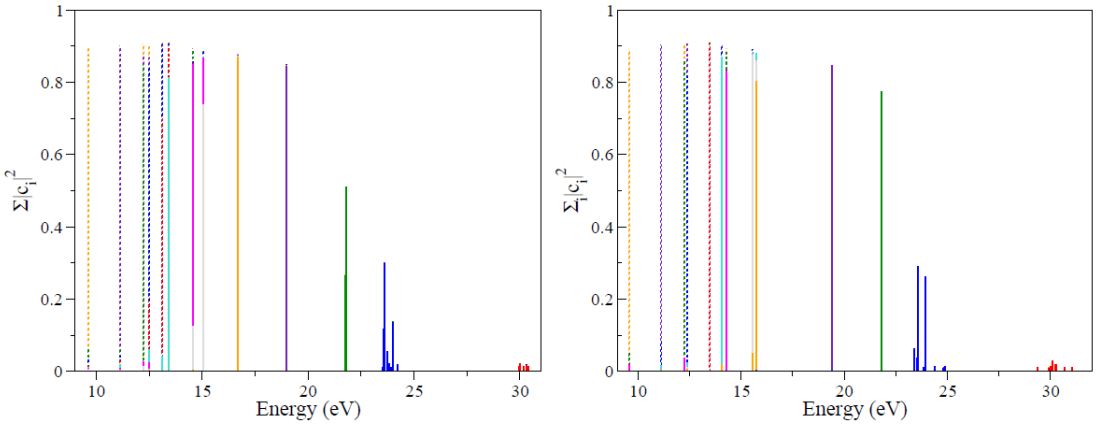



Figure 4.2: Ionisation spectrum (see Figure 2.4) for the two conformers of isopropanol. Colour and line-type is used to differentiate the contribution from 1h states of the molecule in the molecular orbital picture. Colours are also consistent with Figure 4.3 and the 4 states of interest, 5a, 6a, 7a, and 8a, are respectively represented by red, blue, green and purple solid lines. The left plot shows the gauche conformer, and the right plot shows the anti conformer. Image credit: Bridgette Cooper

Figure 4.3 shows the hole survival probability, $S(t)$, which is the amplitude of the projection of the wavefunction onto the wavefunction at $t = 0$, following impulsive excitation of these four states. These calculations were made using the ADC(2)x method for fixed nuclear geometries. The curves in Figure 4.3 are each for a single nuclear geometry. For a fixed geometry, creation of a hole in the 8a molecular orbital is followed by a rapid decay, on that attosecond timescale, to approximately 0.7. This has been described as the universal response of molecules to ionisation [2], as the hole dissipates over the molecule. Beyond this, the population persists over tens of femtoseconds. A hole created impulsively in the 7a orbital sees a greater attosecond decay, to 0.6, and then continues to decay non-linearly for the 40 fs duration of our simulation. For the 6a orbital, a decay over 5 femtoseconds is followed by oscillatory evolution with a period of 10-15 fs. Finally, the 5a orbital sees a fast, exponential-like decay in just a few femtoseconds. As the nuclei are fixed, it can be determined that the dynamics arise purely from the electronic wavepacket driven by electron correlations between states. It should be noted however that nuclear dynamics will play a role, particularly on the timescales of their motion, i.e. on the 10s of femtoseconds timescale.

A notable trend is that with increasing binding energy the correlation driven dynamics become faster and more extreme. This rule of thumb, though not universally true, comes from the

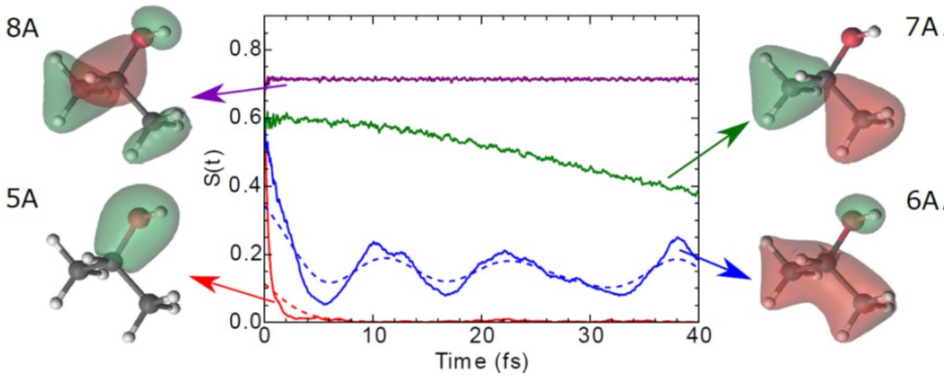



Figure 4.3: Hole survival probability in different initial (neutral) inner valence orbitals 8a (outermost) to 5a (innermost) after single ionization of isopropanol. The survival probability curves correspond to a mixture (1:1) of the two lowest conformers of the molecule. Dashed lines account for convolution with a 5 fs pulse. The orbitals shapes (Hartree-Fock) are shown around the plot for gauche conformer. Image credit: Bridgette Cooper

increased opportunity of couplings to 2-hole 1-particle states with increasing binding energy. The 6a hole, which is the most energetic hole which lies above the double ionisation potential, provides the most interesting case and can be understood as 'frustrated Auger-Meitner decay'. The hole wavepacket of the 6a state is initially well localised but the diffuse 2-hole nature of the wavepacket draws the charge density away from the molecule as the coherences propagate in time; but, being below the double ionisation potential, the wavepacket lacks the energy required to decay via auto-ionisation and at later times, the phases begin to partially realign and form revivals. It is this decay channel that is of particular interest to the measurements described in this chapter.

Static photon absorption and photoelectron spectroscopy can be used to estimate hole lifetimes but provide little information about the decay process itself. Therefore, a more direct method of measuring the IVH decay path is required. Pump-probe experiments provide this direct, time-resolved approach. Even for linear probing methods, pump-probe experiments require a sufficient excitation fraction of the sample to have any chance of detection. This is readily achieved for optical and infrared pumps, using tabletop lasers; however the strong fields required for tunnelling ionisation (Keldysh parameter much less than 1) dress the system in such a way that the resulting hole dynamics are no longer representative of the field free molecule [9, 10]. Also, the kinetic energy of the outgoing electron is far below that required for the sudden ionisation limit to be satisfied. Furthermore, dynamics occur on the femtosecond or even

attosecond[11] scale, which is fundamentally inaccessible in these regimes due to the required time-bandwidth product.

On the contrary, single ionisation from a soft X-ray pulse creates the desired hole wave-packet in an otherwise noninvasive way as it is far from rotational or vibration resonances so does not heat the molecule in the way that a strong field IR pulse will. Moreover, the use of soft X-ray wavelengths offers the possibility to address transitions from the core to the valence band of a specific atomic species, allowing an atomic site probing of the molecular hole dynamics. Considering the options detailed in Chapter 3, X-ray free electron lasers provide the only possible route to generating pulses for a soft x-ray pump and probe as HHG is unable to provide the excitation fractions required. Fortunately, X-ray free electron lasers (FEL) are making rapid progress towards shorter pulse duration, having recently reached the attosecond regime using the XLEAP technique [12]. To measure the charge dynamics in isopropanol, access to the atomic, molecular, and optical science (AMO) beamline at LCLS was granted, operating under the fresh-slice mode [13].

## 4.1 Experimental Overview

Figure 4.4 shows an overview of the experimental scheme. The pump step of the experiment involved single X-ray photon excitation of an inner valence hole (IVH), and the IVH state time-dependence was probed through resonant absorption from the O 1s state at the oxygen site. These two pulses were tuned to 35 eV and 20 eV below the K edge of oxygen in the molecule, for pump and probe respectively, and separated by a variable delay from 0 to 30 fs. When the probe was tuned to the appropriate energy, and following valence ionisation from an inner valence orbital, a transition from the oxygen K shell (1s) to this inner valence hole was possible, as shown in Figure 4.4c.

The fingerprint Auger electron signal associated with the subsequent refilling of the 1s core hole then tracked the probe photon absorption, as proposed in [14]. The time dependence of the absorption registers the evolution of the inner valence hole. This X-ray pump-probe methodology provides unique access to the electron dynamics with few-femtosecond temporal

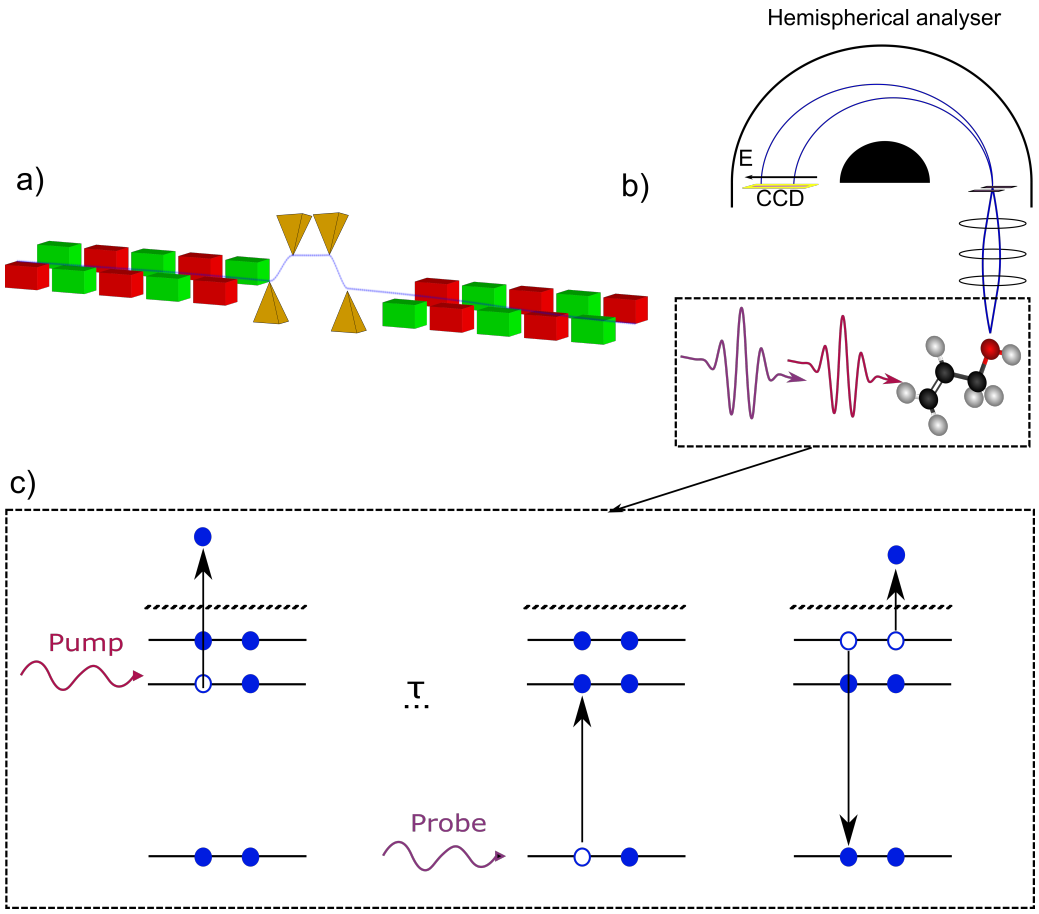



Figure 4.4: a) Pump (499 eV) and probe (514 eV) pulses generated via the fresh slice mode with variable delay, $\tau$, are b) incident on a isopropanol and photoelectrons are collected. c) Shows the molecular response to the two pulses: First, the pump ionises the isopropanol from any one of the valence orbitals, including the creation of inner valence holes. This opens a transition to the oxygen 1s core excited state, if the probe meets that resonant condition. The strength of that transition is proportional to the hole population delay $\tau$. Following this, the most common decay channel is via Auger-Meitner decay, in which the core hole is filled and an electron is removed from the valence, which can then be detected.

resolution and is spatially resolved to an atomic site. Figure 4.3 shows the time dependence of the hole survival probabilities following sudden ionisation for one conformer of isopropanol, in a fixed geometry.

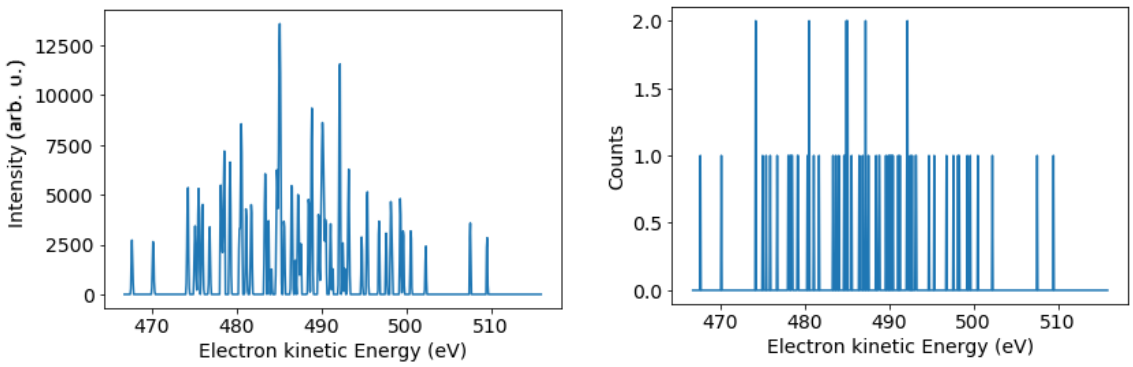
Five shifts at the LCLS AMO end-station [15] were dedicated to this experiment. Of these shifts, two were used for setup and calibration of the FEL and its instruments. The data analysis presented focuses on two data series, in which the FEL was tuned to the correct resonances and the spectrometer was set to measure the decay. They will be denoted Series 1 and Series 2. Series 1 was conducted with the vernier tuned up to the resonance and the centre of the electron spectrometer at 500 eV. Total acquisition time was 124 minutes, which makes this the larger of the two data series. Delays of -15, -12, -9, -6, -3, -1, 0, 1, 2, 3, 5, 6, 9, 15, and 20 fs were used, in a randomised order. Series 2 was the same photon energy and detector window as Series 1, but with the FEL optimised for a shorter pulse duration. Delays of -3, -1, 1, 2, 3, 5, 7, and 10 fs were used, also randomised.

## 4.2 Available instruments and preprocessing

The LCLS beamline and AMO end-station offer state-of-the-art instruments for single-shot detection and diagnostics. The main available instruments for the experiment were: the main detector, an electron spectrometer; and pulse diagnostics for the pulse spectra, intensities and temporal profiles. These were all acquired on a single shot basis. The first step in the analysis was to process these shots, removing noise, backgrounds, etc., and storing their output in a manageable format. Each of these instruments and the processing that was done on each of them on an individual basis (pre-processing) is described here.

### 4.2.1 Hemispherical electron energy analyser

The electron spectrometer detector was a hemispherical analyser with half-angle acceptance of 30° (1/16 of the total solid angle) and 1.25 eV spectral resolution. Note that the 30° half-angle acceptance is insufficient for many correlation measurements, such as electron-electron covariance mapping.



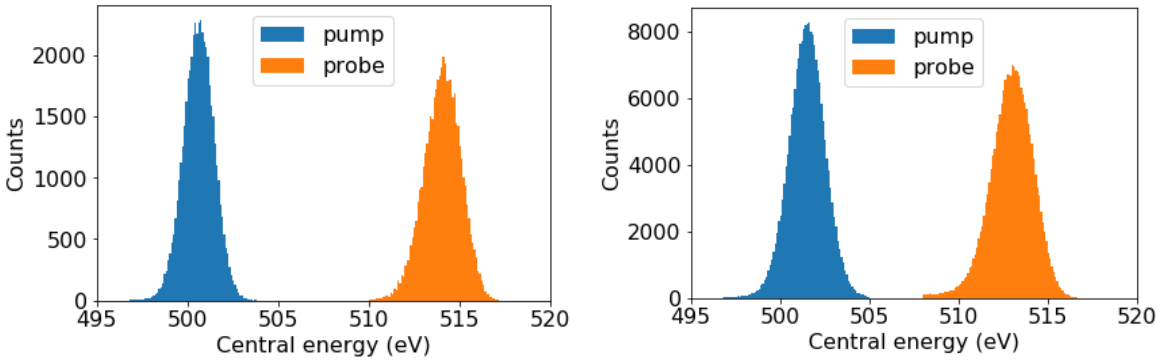

(a) (b)

Figure 4.5: (a) Typical single-shot spectrum from the hemispherical analyser after accounting for geometric effects. (b) Spectrum from the same shot as (a), but after using hit-finding algorithm to identify and homogenise single electrons.

Whilst the camera which images the electrons had a square array, due to geometric effects (MCP and slit) the usable portion of the MCP was not square. To remedy this, a perspective transformation was done on the raw images to crop and re-scale the usable portion of the detector such that the response due to linear effects was constant across the region of interest. This was done using the CV2 image manipulation package. With the detector window nominally centred at 493 eV the usable region of interest covers the window 466.8-515.9 eV. Although hemispherical analysers are also angularly resolved, this provides little useful information for this experiment as Auger electrons have no angular dependence; so, shots were summed over one axis for simplicity and to reduce memory cost. Figure 4.5a shows a single shot spectrum acquired at this window position, after accounting for geometric effects. Individual electrons are easily identifiable on single shot images as sharp peaks in the spectra. However, they are not homogeneous, as is desired. To rectify this, a 'blob-finding' algorithm was used which looked at the geometrically transformed images and identified the positions of 'blobs' which corresponded to individual electrons and added them to a histogram with each bin corresponding to a single column (energy varies along horizontal axis) of pixels. The result is that each electron hit then contributed equally to the resulting lineout, as can be seen in Figure 4.5b.

### 4.2.2 X-ray spectrometer

Single-shot X-ray spectra of both the pump and probe pulses were acquired for every shot on a single camera image of window 484–549.3 eV. A dark background recorded in Run 117 (with no-lasing) was subtracted from each image. The spectra were then Gaussian filtered, and a threshold was applied. Guassian fits were made to each shot of the lineouts. The fitting is noticeably poor as the spectra are not Guassian; however, the central energies retrieved are reliable and can be verified by comparison with the first moment (centre of mass) in the pump and probe spectral ranges. Figure 4.6 shows the retrieved distributions of pump and probe central photon energies.



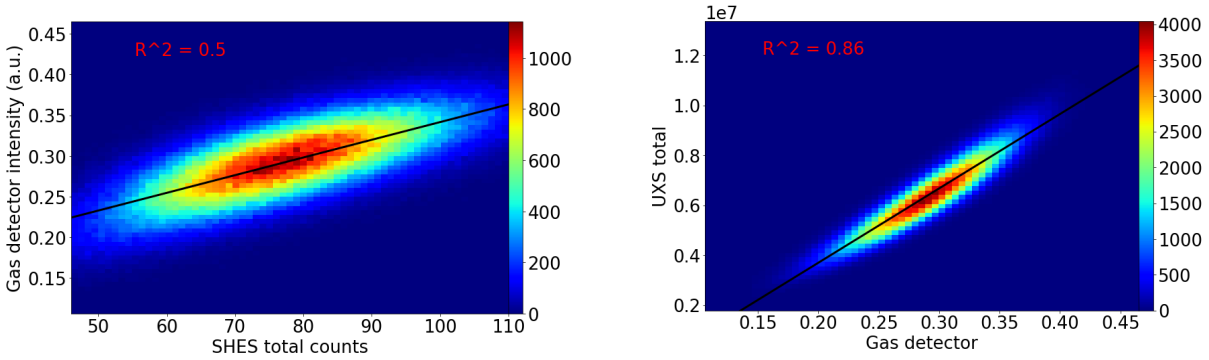

(a) (b)

Figure 4.6: Distribution of pump and probe central photon energies for (a) Series 1 and (b) Series 2 . There is a notable shift of the pump pulse to higher energies, and the probe to lower energies from Series 1 to 2.

### 4.2.3 Gas detector

To measure the energy in each pulse, a low density gas detector was used [16]. This measures the strength of luminescence in the ultraviolet (300-400 nm) following photoionisation of an inert gas, such as nitrogen. Other methods of measuring the single-shot pulse energies were available, such as the total electron counts and the total signal detected on the X-ray spectrometer. The former suffers on two counts: firstly, the expected dynamics would result in a time dependent electron signal; and secondly, the low collection efficiency and count rate would lead to poor correlation with the true value. The latter should also provide a good measure; however, questions were raised following the experiment regarding the input pointing stabilisation to the

X-ray spectrometer. Nonetheless, an indication of the maximum error of the gas detector can be found by considering its correlation with these alternate measures. Figures 4.7a and 4.7b show two-dimensional histograms and linear regression fits between the gas detector and, respectively, the total electron analyser counts and X-ray spectrometer signal. It correlates strongly with the X-ray spectrometer and less well with the electron spectrometer counts, most likely due to difference in collection efficiency between the two measures; note that not only does the electron spectrometer not collect all angles of electron emission, but it also only collects electrons within a set energy window.




(a) (b)

Figure 4.7: Two-dimensional histograms and regressions showing the correlation between the available measures of intensity. (a) The total electron counts vs the gas detector and (b) The gas detector vs the photon spectrometer

### 4.2.4 XTCAV

X-band Transverse Deflecting Cavity (XTCAV) is a photon diagnostic tool which works by looking at the electron bunch after lasing and uses this information to infer the temporal structure of the emitted pulses [17, 18]. It can be run simultaneously with data acquisition for non-intrusive single-shot diagnostics. XTCAV works by using a X-band radio frequency deflector to apply a time dependent force to the electron bunch, perpendicular to their propagation axis (horizontally). In doing so, time in the bunch is mapped to the propagation axis. A dipole magnet is then used to deflect the electron beam vertically by an amount dependent on the electron energy. The result is that energy in mapped to the vertical axis.

At fixed intervals of the experiment, short runs were made in which no amplified emission was

allowed within the bunches. This generated a bank of 'lasing off references' which were used for the runs immediately before or after to avoid errors introduced from long term fluctuations in the FEL's behaviour. Some image processing was done on these shots to mask the background of the image and crop to a smaller area as well as some denoising. In order to reduce the statistical error in the reference it was desirable to average over many shots. However, averaging all of the shots means that variation between the bunches is ignored. Ideally, one wants to compare a lasing XTCAV image with a non-lasing XTCAV image which had a similar original bunch. As a compromise, the bunches were separated into 20 groups according to their likeness (pixel correlation) and these groups were then averaged to form a bank of 20 references. For each of these lasing off references, the centre of mass and RMS spread of the energy (vertical) axis were calculated for comparison to the lasing on shots. For each laser shot in which lasing was allowed, the XTCAV image was processed according to the same methods as the lasing off reference. The processed image was then compared to the bank of lasing off references taken at a time closest to the shot, to find the lasing off reference most similar. The retrieval was then done, comparing the energy COM and RMS of the lasing XTCAV shot and lasing off reference to retrieve the temporal profile of the lasing in the shot. Finally, a fit was then made to each retrieval and those parameters recorded which would be useful in the data analysis for the experiment.

Figure 4.8 shows four stages of the retrieval process: the raw XTCAV images, a processed lasing on shot, processed lasing off reference, and the fitting to the retrieval. Figure 4.9 shows the retrieved pulse parameters from Series 1. Unfortunately, the resolution of the XTCAV is not sufficiently high to resolve the smaller pulse from Series 2. It was however able to verify that the pulses in Series 2 are typically shorter than in Series 1, and was able to verify the pulse separation within the bunch and to measure its jitter. The median pulse lengths (FWHM) in Series 1 were 7 fs for the pump and 8 fs for the probe. Note that as this is close to the resolution limit of the XTCAV, the pulse duration is likely smaller, though this is hard to quantify.

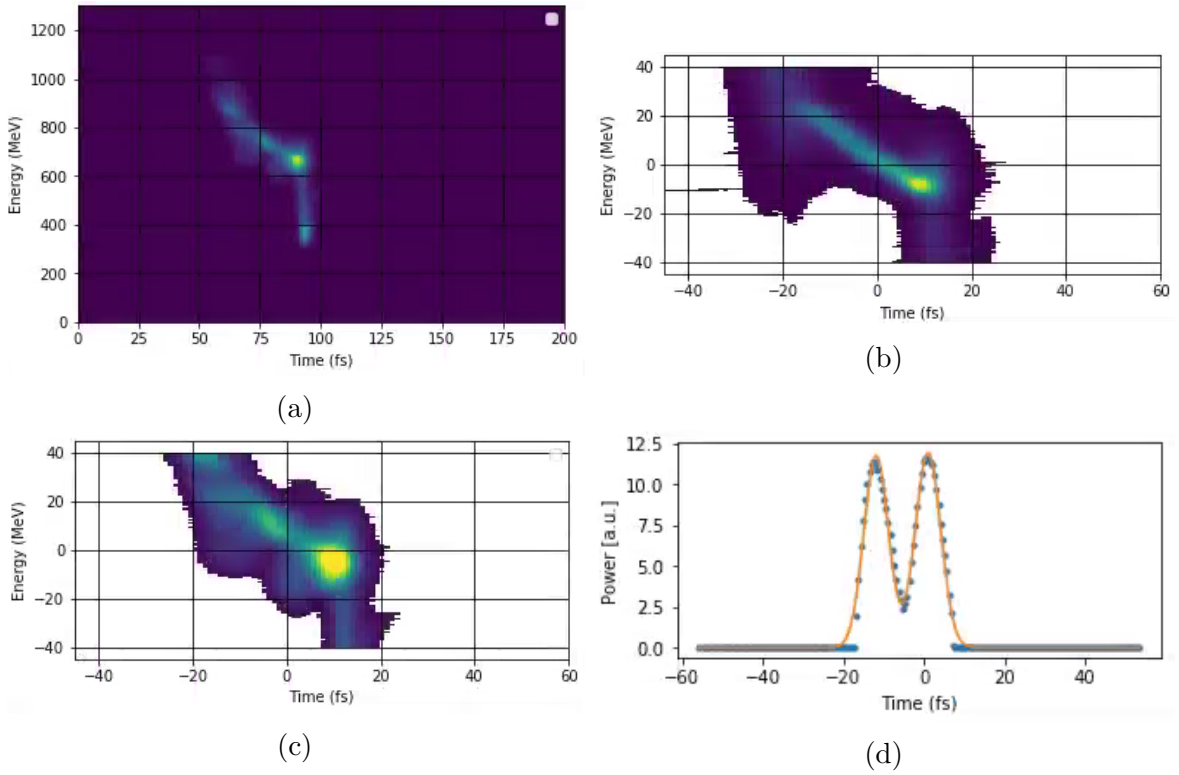



Figure 4.8: Processing steps of XTCAV retrieval. (a) A raw image of an electron bunch from shot with lasing (b) As in (a), but cropped and centred to the desired region of interest; (c) As in (b) but for an average of comparable shots without lasing; (d) Pulses retrieved from (b) and (c). Blue points show retrieval with orange line showing fit of two Gaussian pulses.

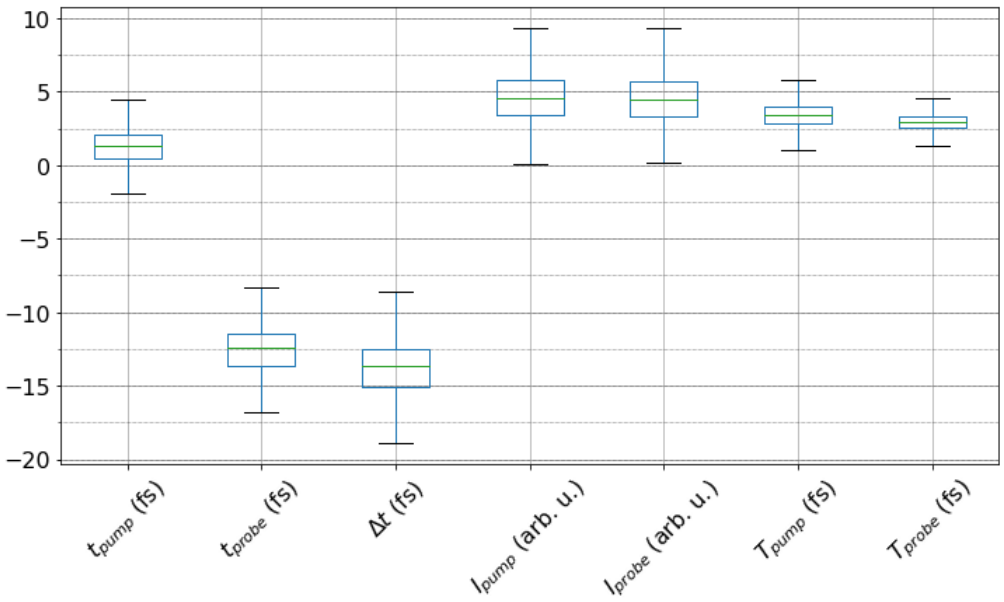



Figure 4.9: Box and whisker plot showing the pulse parameters (pulse timings, pump-probe delay within electron bunch, pulse intensities, and pulse temporal standard deviations) for the pump and probe across Series 1, as retrieved from the XTCAV diagnostic. Blue boxes demarcate the inter-quartile-range; green lines show the median, and black whiskers demarcate the range of outliers defined by exceeding value 1.5 times the inter-quartile-range from the median. Units for the vertical axis are shown in brackets after the parameter labels.

## 4.3 Normalisation, sorting, and selection of pulses

A second stage of processing was then done, with the aim of resolving a noise and artefact free time dependent Auger yield. The main function of this round of processing was to normalise the data to the fluctuating parameters of the FEL, to remove anomalous shots for which the parameters are not useful for the measurement, and to sort the remaining shots according to the shot parameters (pump and probe energies, delay, etc.).

FEL data is intrinsically noisy due to the dependence of pulses on the electron injection into the undulators and the tuning of the FEL. Shot-for-shot fluctuations lead to noisy signals, thus requiring increased statistics; and slower changes such as those when tuning the FEL to change the time delay, can lead to time dependent artefacts. Suppose that the time dependent signal $f(\tau)$ also depends on the fluctuating experimental parameters $X_i$, such as the pulse energy, pump-probe ratio, photon spectrum, etc.

$$f(\tau) = f(\tau, X_1, X_2, ...) \tag{4.4}$$

The data analysis process aims to find the best estimate for the population mean of $f$ given the sample of shots during the experiment. The error of the mean is typically $\sqrt{s_f^2/(N-1)}$ where $s_f^2$ is the variance and $N$ is the total number of shots. The variance of the signal at fixed time delay depends on the variance of the parameters it depends on and how strong the dependence is, according to

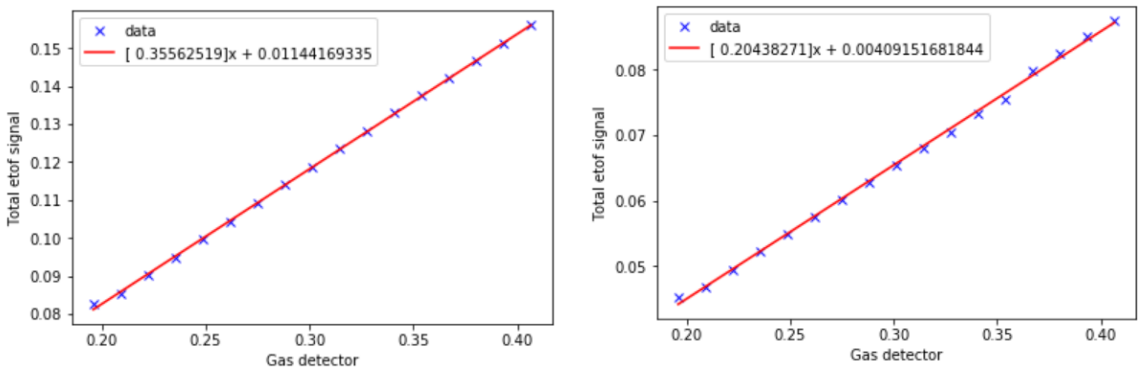
$$s_f^2(\tau) = \left(\frac{\partial f}{\partial X_1}\right)^2 {s_{X_1}}^2 + \left(\frac{\partial f}{\partial X_2}\right)^2 {s_{X_2}}^2 + ... \tag{4.5}$$

Furthermore, time dependent artefacts due to the FEL tuning can be expressed as time dependence of the parameter means, $\bar{X}_i(\tau)$. Shot normalisation, which multiplies the signal by a parameter dependent factor, aims to reduce the dependence of the signal on the fluctuating parameters, $\partial f/\partial X_i$. Removal of shots with undesirable properties, referred to here as shot discrimination, aims to remove the parameter dependence on time and reduce the variance of each parameter. It also allows for the shifting of parameter means to desirable values (short pulse lengths, high pulse energies etc.).

The effectiveness of both normalisation and shot discrimination depends on the quality of the diagnostics, and can be measured by looking at the variance of the signal. For the normalisation, this means finding the functional dependence of the signal, i.e. the electron kinetic energy spectra, on the diagnosed parameters. The two most important parameters to correct for were the pulse energy, as measured by the gas detector, and the pump-probe-ratio, as measured by the X-ray spectrometer.

One would expect the electron signal to vary approximately linearly with the pulse energy (assuming the nonlinear signal to be small). Figure 4.10 shows the dependence of the gas detector with the total electron signal for Series 1 and 2. An important step in normalisation was recognising that there is a non-zero y-intercept in this relationship. Correcting for this led to a reduction of the variation of the total electron signal across the range of gas detector values from 7.2% to 1.0% for Series 1 and from 4.5% to 1.5% for Series 2.

Variation in the pump-probe intensity ratio required more complicated normalisation as the dependence of the electron spectra on the pump-probe signal varies across the binding energy range of the electrons. I.e, parts of the spectrum dominated by pump excited electrons will




(a) (b)

Figure 4.10: Linear dependence between the pulse energy measurement of the gas detector and the unnormalised total electron signal for (a) Series 1 and (b) Series 2. These were obtained by binning the shots according to their gas detector values and averaging the electron spectra and summing them.

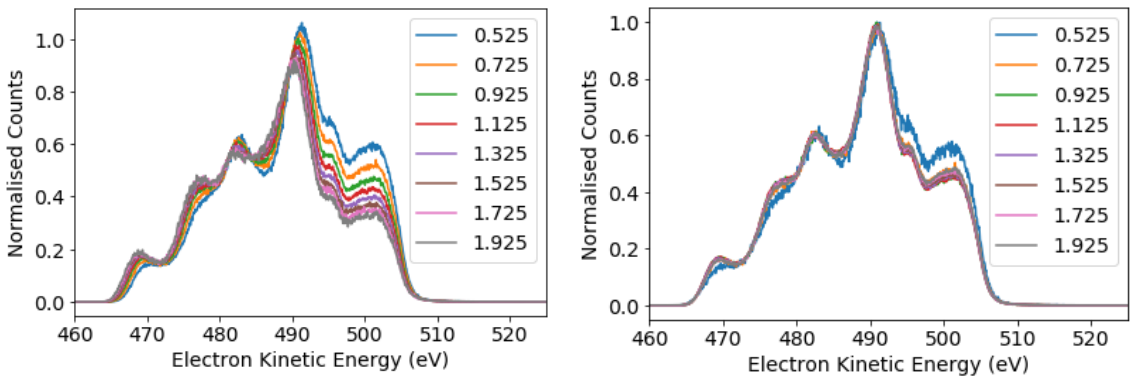
increase with pump-probe ratio whilst probe dominated regions will decrease. Figure 4.11a shows the photoelectron spectrum at various pump-probe-ratios. Therefore, a linear dependence was found individually for every energy bin, resulting in a 'spectrum' of gradients, $m(E)$, and intercepts, $c(E)$. For every shot and energy bin, modifying the spectrum

$$f(E) \to \frac{f(E) - c(E)}{\mathrm{PPR}} + c(E), \tag{4.6}$$

the result is a spectrum as it would be with a pump-probe-ratio of 1. Figure 4.11b shows normalised electron kinetic energy spectra, demonstrating that the normalisation works for all but the most extreme cases.

The scientific case for normalising to total energy and pump-probe ratio is clear. Other factors, such as the spectral widths and relative energies between the pulses, have less trivial effects on the electron spectra and are thus more difficult to correct for. Fortunately, the pulses are generated from the same electron bunch; therefore the variance of the relative energies is much smaller than the variance of the individual energies, and has little effect on the result. Figure 4.12 shows the correlation between the pump and probe photon energies by looking at the average probe photon energy for shots binned by pump photon energy.

Despite the normalisation and the randomisation of the order of the run delays, there was still




(a) (b)

Figure 4.11: Electron kinetic energy spectra for various pump-probe ratios from Series 1, before (a) and after (b) normalising to the pump-probe-ratio. In (b), only for data in the lowest pump-probe-ratio bin does the spectrum deviate greatly from the other shots.

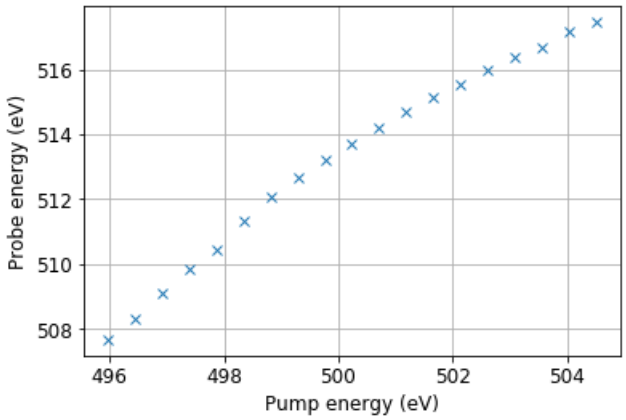



Figure 4.12: Dispersion of the pump photon energy with probe photon energy in Series 1.

concern that variation of the FEL parameters between runs could have led to artefacts in the data. The pump-probe ratio was of particular concern. The variation of pump-probe ratio with the measured delay in Run 5 - Shift 1 is shown in Figure 4.14a.

The simplest method of reducing this variation is to only allow shots within a specified, narrow band of values. This was done for the gas detector and the XTCAV delay. Doing this is effective, but some delay dependence persists as there may be a skewed distribution within this narrow band, and there is an expensive reduction in the statistics. Therefore, an improved method was used: Firstly, a desired pump-probe ratio was chosen (1). Then shots outside of a broader band ($0.9 < PPR < 1.1$) were discarded. Remaining shots were binned according to their pump-probe ratio, then the bin bounding the desired value was identified. The minimum of

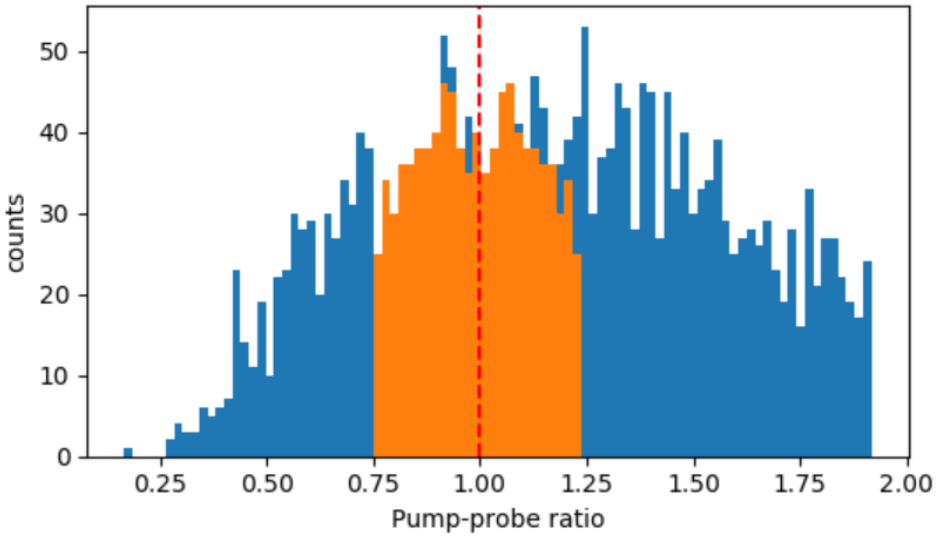
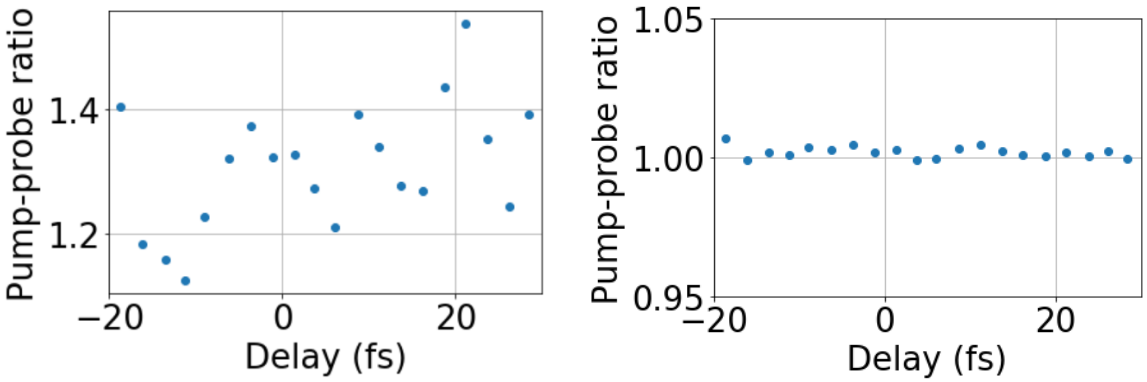



Figure 4.13: Example of down-selection of shots based on their pump-probe ratio. The blue histogram shows the original distribution of pump-probe ratios for the first 4000 shots of Run 213. First, the data is reduced to those shots which lie in a given range. In this graphic, the range is 0.75 to 1.25, but a range of 0.9 to 1.1 was used in the analysis. Then, the bin containing the desired mean, 1, is identified and can be labelled as $x_m$. Then, the bin to the left, $x_{m-1}$, and to the right, $x_{m+1}$, of this are found. The bin to the left has $y_{m-1}$ shots in it whilst the bin on the right has $y_{m+1}$. If $y_{m+1} > y_{m-1}$, $y_{m+1} - y_{m-1}$ shots are thrown away from bin $x_{m+1}$. Conversely, if $y_{m-1} > y_{m+1}$ , so $y_{m-1} - y_{m+1}$ shots are thrown away from bin $x_{m-1}$. This is repeated for bin pairs $[x_{m+2}, x_{m-2}], [x_{m+3}, x_{m-3}]$, etc.

the counts in the bin to the left of this bin and the counts in the bin to the right of this bin was then found and excess shots discarded from the more numerous bin. This was repeated for the bins 2 to the left/right, 3 to the left/right, etc. In this way, a symmetric distribution of shots centred around a desired value was reached. Figure 4.13 shows graphically how this method works. Typically, 5-10% of shots are thrown away at this stage. Figure 4.14b shows the variation in the pump probe intensity with delay after adopting this method.

Time-dependent spectra were found by binning the shots into time and probe energy bins, creating large 3-D arrays with axes corresponding to delay, probe energy, and electron energy and each element containing the normalised number of electron counts in that bin. A second, 2-D array of time and probe energy contains the number of shots in each bin, necessary for weightings in the further analysis. The time delays were determined by accounting for the chicane delay (which was changed to change the delay), the temporal spacing of the lasing within each bunch, and the slippage between the generation of light and the electron bunch




(a) (b)

Figure 4.14: Mean pump-probe ratio in each measured time bin (a) before shot discrimination and (b) after shot discrimination. Note that the arithmetic mean, which is used here, skews the mean to higher values and gives the impression that the pump is stronger than the probe - e.g. the arithmetic mean of 0.5 and 2 is not 1.

(approximately 2 fs).

The process being investigated as the probe is resonant, so the approach taken was to define a resonant region and look for relative time-dependent dynamics at this resonance as compared to off of the resonance. The resonance is expected to be broad due to the short lifetime of the core excited state. This means that the region identified as off-resonance may in fact be in the tail of the resonance and may also be time-dependent. Nonetheless, the dynamics should be stronger at the peak of the resonance so looking at their difference still identifies signal. It is also useful to subtract a large negative time delay ($\tau = \tau_-$) or a large positive time delay ($\tau = \tau_+$) in order to set a baseline for an increase or decrease in counts. If the on-resonance (off-resonance) electron kinetic energy ($E_\mathrm{e}$) signal at delay $\tau$ is $f(E_\mathrm{e}, \tau)_\mathrm{on}$ ($f(E_\mathrm{e}, \tau)_\mathrm{off}$), the signal is then

$$\Delta f(E_\mathrm{e}, \tau) - \Delta f(E_\mathrm{e}, \tau = \tau_{+/-}); \tag{4.7}$$

$$\Delta f(E_\mathrm{e}, \tau) = f(E_\mathrm{e}, \tau)_\mathrm{on} - f(E_\mathrm{e}, \tau)_\mathrm{off}. \tag{4.8}$$

## 4.4 Results

During the experiment, runs of data with lasing only in the pump undulators were taken intermittently. Unfortunately, it was not possible to do the same for the probe, but nonetheless,

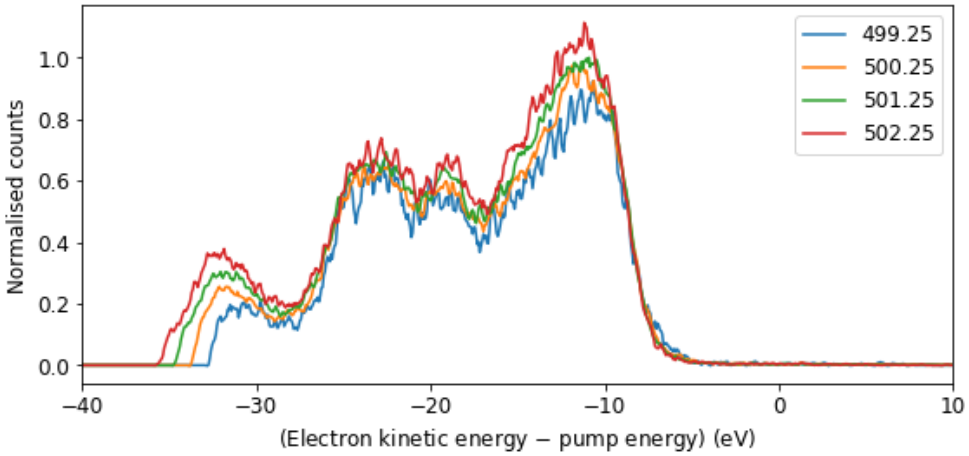



Figure 4.15: Pump only electron kinetic energy spectra shifted with the pump photon energy. Pump spectra are binned into 0.5 eV bins and then averaged. The averages of four bins are displayed, with the bin centre shown in the key.

the pump only spectra provide useful information for interpretation of results. Figure 4.15 shows the pump-only spectrum taken concurrently to Series 1. The single shot spectra were binned according to photon energy and averaged. Before doing so, the single shot spectra were shifted according to the pump photon energy as the kinetic energy of photoelectrons and resonant Auger electrons typically increase linearly with the photon energy.

Figure 4.16 shows typical spectra for different probe energies where both the pump and probe pulses are present. The result is a superposition of the pump spectrum in Figure 4.15 and a similar spectrum translated by the difference in the pump and probe energy, approximately 14 eV. The electron kinetic energies are shifted by the probe photon energy. For the probe photoelectrons and resonant Auger electrons, this corresponds to the binding energy. This is not true of the pump driven part of the signal but, as the pump and probe disperse almost linearly, is approximately the binding energy offset by 14 eV.

The larger number of shots acquired in Series 1 makes it suitable for the identification of resonances within the probe signal. To do this, the shots were binned into larger bins in the probe photon energy (1 eV) to increase the statistics in each bin and the magnitude of the transient signal was found by summing spectra for small time delays and subtracting averaged spectra from large negative time delays. The resulting absorption spectrum, plotted in Figure 4.17a, identifies spectral regions with transient dynamics. Three regions are shaded. The blue

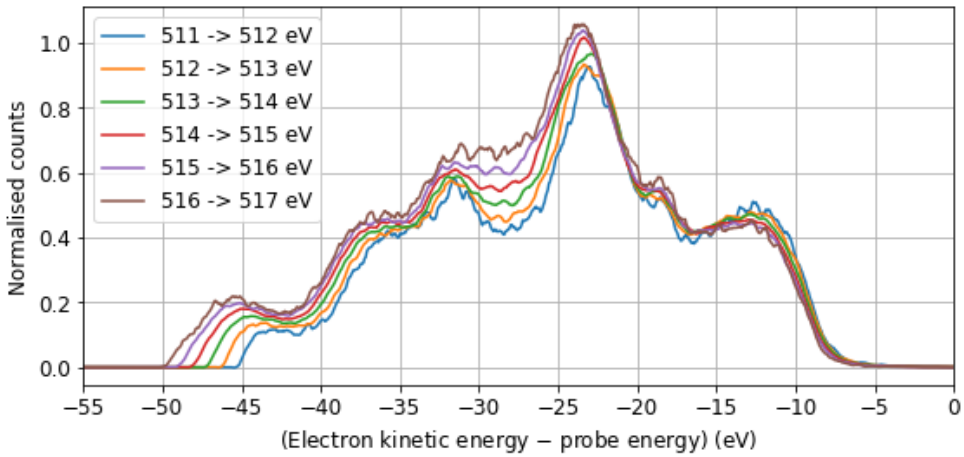



Figure 4.16: Pump and probe electron kinetic energy spectra shifted with the probe photon energy. Spectra are binned into 0.5 eV bins and then averaged. The averages of six bins are displayed, with the bins shown in the key. Pump photolines also move with the probe with dispersion of almost 1.

and green regions have a positive transient signal and correspond to where the resonances corresponding to the oxygen 1s → 6a and oxygen 1s → 7a transitions were predicted to occur. The grey shaded region corresponds to a region away from resonance with a significant number of shots which can be used to subtract the off-resonant signal. Looking specifically at these regions, Figures 4.17b and c show the transient Auger yield (see Eqn. 4.8) associated with the filling of the 6a and 7a holes (colour coded to Figure 4.17a), which corresponds to the hole population and can interpreted as mapping the hole lifetime following ionisation.

The lesser statistics in Series 2 makes a similar analysis of the transience difficult; however, the shorter pulse duration makes it more suitable for the study of the faster migration of the 6a hole. The advantage is two-fold: a shorter pulse is able to better resolve the state lifetime and the peak signal is larger due to the reduction in time-averaging of a rapid decay. Series 2 shows a clear time-dependent signal centred at approximately −20 eV, on the right shoulder of the largest peak of the spectrum. Summing along the energy axis between −15 eV and −25 eV, a time dependent 'total signal' can be found. Figure 4.18 shows this signal. The signal has been divided by the sum of the average spectrum in this region to find a fractional change. The peak change of just over 2% is in line with expectations prior to the experiment, given the collection efficiency of the detector. Note that whilst fractionally smaller than the peak transient signal found for Series 1, this electron energy region sits on a larger background of

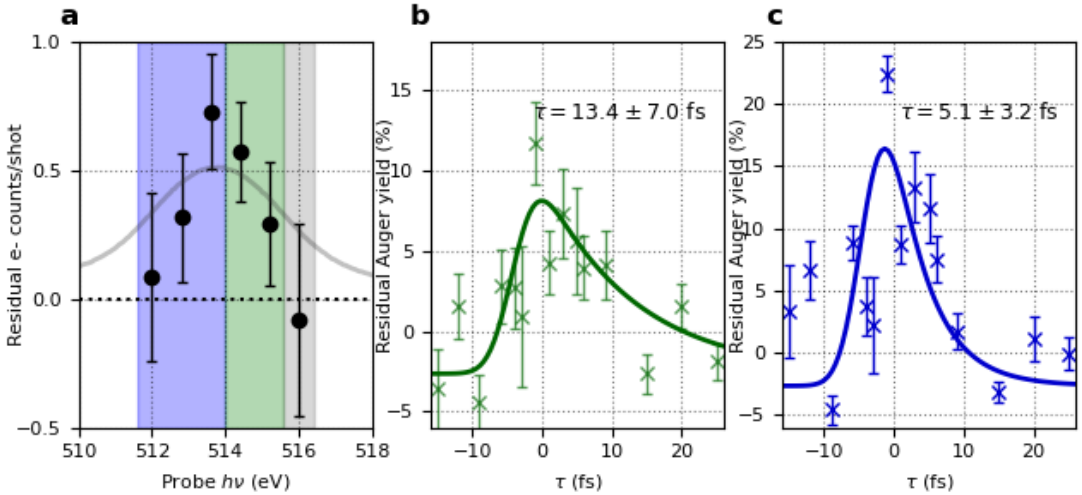



Figure 4.17: (a) Probe central photon energy dependence of residual signal at delay ∼0 fs. (b) Time dependence of residual resonant high kinetic energy electron signal at higher probe photon energy, about expected $1a \rightarrow 7a$ transition (green), and (c) time dependence of residual resonant high energy electron yield at lower probe photon energy about expected $1a \rightarrow 6a$ transition (blue). Fits to an exponentially modified Gaussian functional form are shown in black and the extracted decay time is given in each panel.

direct photoelectrons and is, in fact, approximately twice as large when normalised to the total photoelectron signal. Figure 4.18c shows the residual signal at small positive time delays. A ∼8 eV peak centred at ∼21 eV binding energy can be seen, despite the small signal-to-noise ratio.

Up to four electronic states are involved in the resonant decay: the Oxygen 1s and the 6A state which it is excited to; a second valence state which decays to the Oxygen 1s hole; and a third valence state from which an Auger electron is emitted, c.f. Figure 4.4. The Auger electron kinetic energy is $E_3 + E_2 - E_{\mathrm{O1s}}$ where $E_3$, $E_2$, and $E_{\mathrm{O1s}}$ are the binding energies of the third valence state, second valence state, and Oxygen 1s state respectively. A binding energy of 21 eV corresponds to $E_3 + E_2 = \approx 45$ eV. This could correspond to e.g. two electrons from the 7a orbital, or 1 electron from the 5a orbital and one from the 9a orbital (see Figure 4.2).

## 4.5 Discussion

The importance of this result lies both in the experimental method, which lays precedent for site-specific probing of hole dynamics in a molecular system and in the result obtained in this

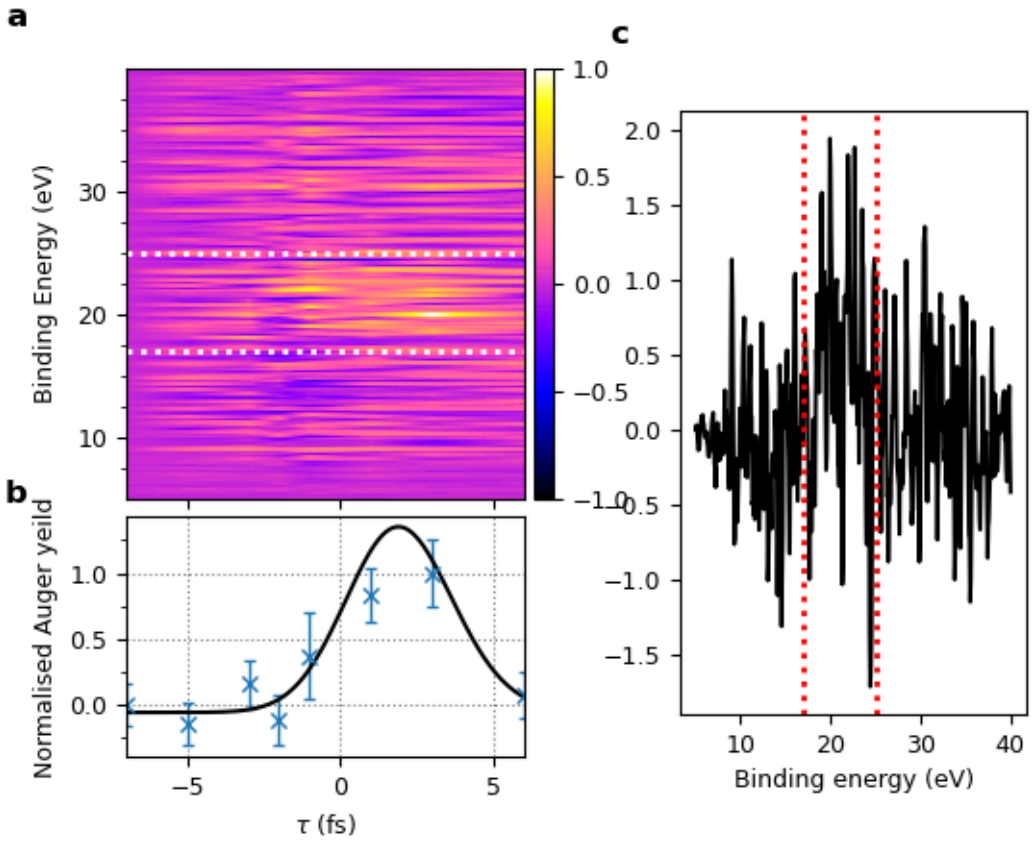



Figure 4.18: (a) Residual electron spectrum of Series 2, between −25 eV and −15 eV, shown as a fraction of the average (on and off) signal in this region. The average of delays less than −1 fs is subtracted. (b) The residual electron yield integrated between −15 eV and −25 eV, as a function of time delay. (c) The kinetic energy spectrum of the residual electron yield, found by integrating over all time delays. A peak between −15 eV and −25 eV is found. (a) and (b) share their horizontal axis.

specific system, isopropanol, which is itself if interest from a theoretical viewpoint.

The key element to the experimental method is the use of a resonant probe process which utilises many of the fundamental principles outlined in Section 2: by selecting a probe which lies energetically just below the oxygen K-edge, the existence of virtual orbitals within the energy range of the continuum allowed us to use the resulting resonant decay as a fingerprint for measuring state populations. This is significant as the non-resonant pump excites a broad range of dynamics within the target ensemble. Typical probes are unable to unravel this multitude of dynamics and interpretation is challenging. However, in this experiment, by utilising this resonant probe and by sorting statistics acquired with different energy probes, the hole lifetime signatures from different ionisation channels have been separated unambiguously. This can be

seen in the different time traces from the 6a and 7a states in Figure 4.17. This measurement gives precedent for the study of correlation driven dynamics in extended quantum systems where the interpretation of results is complicated by the size of the system, e.g. in polymers or biological systems.

This can be described as a data driven approach, utilising high volumes of data which covers a large phase space of pump and probe pulses. This puts an emphasis on the importance of effective diagnostics, data collection, and data processing. Higher repetition rates (tens of MHz) are now readily achieved using superconducting LINACs and require development of new detectors to allow single-shot accumulation, but are able to produce even higher volumes of data and increases the practicability of these analysis methods, which may become increasingly common.

Another benefit of this method is that is is able to utilise the large shot-to-shot instability of the SASE mode of operation, which XFELs use to reach the highest pulse energies. These fluctuations are typically unwanted and when looking at a resonant signal many shots are often thrown away during data analysis. In contrast, the fluctuations in this experiment allowed us to cover two resonances as well as acquire off resonant data, temporally integrated into the acquisition, for comparison. With larger fluctuations (or some additional tuning) and greater statistics, it may have also possible extract the dynamics associated with the 5a and 8a holes (see Figure 4.2). This experimental outlook, favouring measurement over control, is well suited to XFEL light-sources and is best exemplified in the spectroscopic analogue to ghost imaging [19], spooktroscopy [20].

With regards to the insight provided by this measurement on the inner valence hole migration of isopropanol, this measurement provides confirmation of the behaviour found from theory for the 6a IVH, demonstrating that this is an extremely transient hole state with only a few-femtosecond lifetime before relaxing into other states. Consistent lifetimes of $5.1 \pm 3.2$ fs and $1^{+2}_{-1}$ fs were measured in the two series of measurements with longer and shorter probe pulses respectively. The timescale of this measurement, an order of magnitude faster than nuclear dynamics, suggest purely electron correlation driven charge motion, i.e. charge migration. However, in comparison

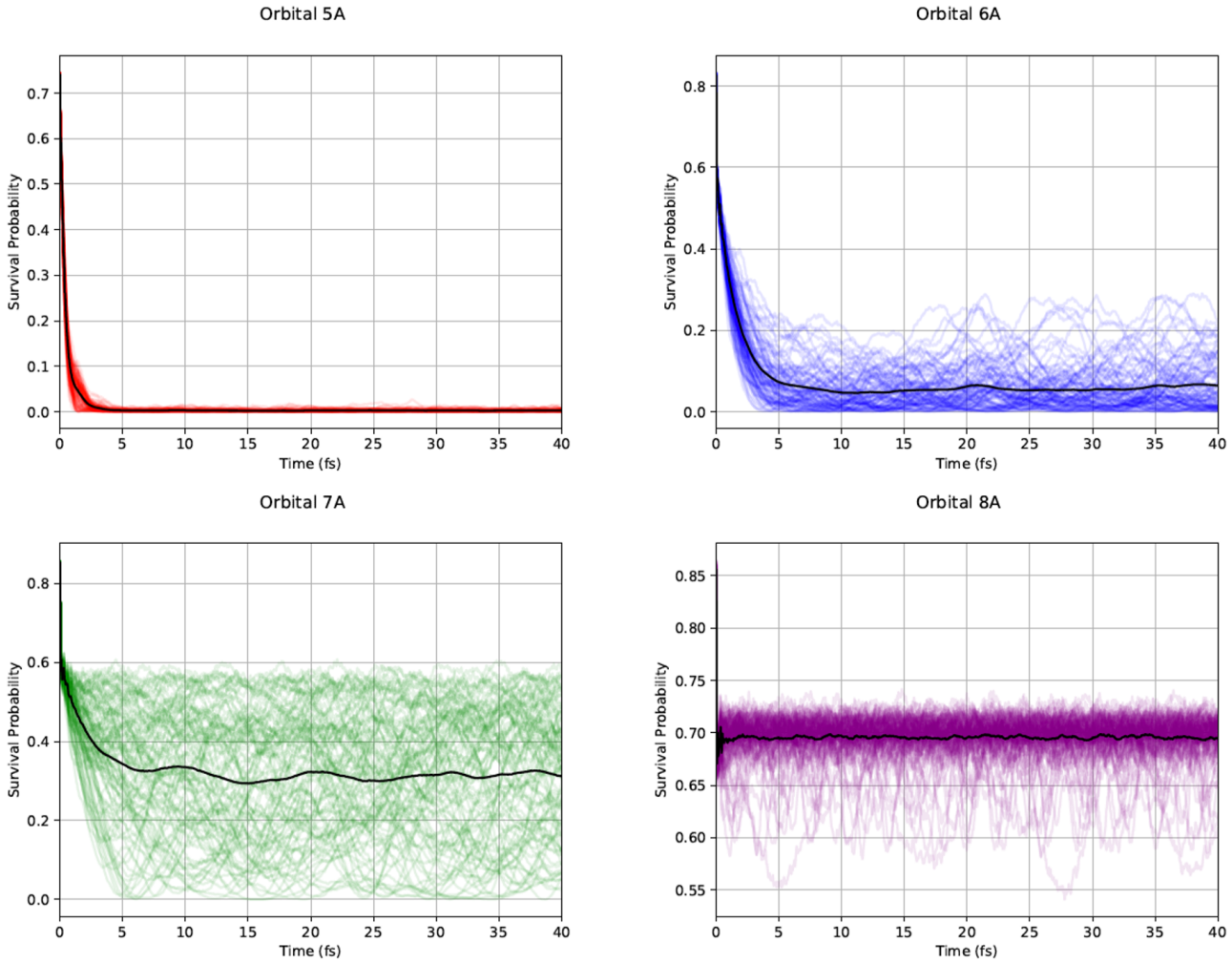



Figure 4.19: Inner valence hole lifetimes 5a, 6a, 7a, and 8a, considering the initial spread in nuclear geometries. For each IVH, single trajectories corresponding to one geometry are plotted coloured and in low alpha. The sum of these geometries is shown in black for each plot. The ensemble averaging is shown to 'wash out' the partial revivals which can be seen in individual molecules, as is particularly visible in the 7a IVH. Image credit: Bridgette Cooper

to the ab intio calculations shown in Figure 4.3, the dynamics are shorter-lived and lack revivals coherent revivals of the IVH population.

To understand this, calculations were made of the hole lifetimes which include non-zero spreading of the initial nuclear geometries by averaging over an ensemble of approximately 500 nuclear geometries for each IVH[1]. Even when considering fixed nuclei following excitation, the precise nuclei position at the time of impulsive ionisation changes the resulting dynamics. This is unsurprising when considering the significant differences between visually similar conformers

[1]Calculations were made by theory collaborator Bridgette Cooper, not the author.

which can be seen in, for example, the spectral intensities of the 7a holes for the gauche and anti conformers of isopropanol (c.f. Figure 4.2). The result of these calculations is that the zero-point geometry masks the partial revival dynamics due to a phase spread between the revivals of different geometries, as can be seen in Figure 4.19.

For the 7a state the experimental measurements show contrasting dynamics to both the calculations considering and not considering the initial nuclear spread. The former predict an initial rapid decay followed by a quasi-stable hole population of approximately 0.3. These calculations fix the nuclear positions during the charge migration; in reality, there is significant nuclear motion on the $\sim 10\,\mathrm{fs}$ timescale which explains the decoherence measured in the experiment. For instance, this could be caused by a lengthening of the carbon-carbon bond coupling to the electronic wavepacket.

The contrast in the success of calculations of the 6a and 7a IVH dynamics emphasises the role of nuclear coordinates. In both cases, it is important to consider the initial spreading in nuclear geometries. Despite referring to charge migration as 'purely electronic', when fixing nuclei and separating nuclear and electronic motion as in the Born-Oppenheimer approximation, it is after all the chemical environment set by the nuclei which determine the electron wavepacket. In the case of charge migration occurring on the timescale of even slight nuclear motion, the motion cannot be ignored.

This also suggests that nuclear motion imposes a limit on the lifetime of electron coherences in molecular systems. It remains an open question whether charge migration — again, note that this is charge movement of the electronically driven type — can play a role in the efficient charge transfer across large molecular systems. This may be possible if, for instance, stable nuclear arrangement can be found which restricts more the freedom of nuclei, such as those on aromatic rings.

# References


[1] L. S. Cederbaum and J. Zobeley. Ultrafast charge migration by electron correlation. *Chemical Physics Letters*, 307(3-4):205–210, jul 1999. ISSN 00092614. doi: 10.1016/S0009-2614(99)00508-4.

[2] J Breidbach and L S Cederbaum. Universal attosecond response to the removal of an electron. *Physical Review Letters*, 94(3), 2005. ISSN 00319007. doi: 10.1103/PhysRevLett.94.033901.

[3] Alexander I. Kuleff and Lorenz S. Cederbaum. Charge migration in different conformers of glycine: The role of nuclear geometry. *Chemical Physics*, 338(2-3):320–328, sep 2007. ISSN 03010104. doi: 10.1016/j.chemphys.2007.04.012.

[4] Andrew J. Jenkins, Morgane Vacher, Rebecca M. Twidale, Michael J. Bearpark, and Michael A. Robb. Charge migration in polycyclic norbornadiene cations: Winning the race against decoherence. *Journal of Chemical Physics*, 145(16):164103, oct 2016. ISSN 00219606. doi: 10.1063/1.4965436. URL `http://aip.scitation.org/doi/10.1063/1.4965436`.

[5] Andrew J. Jenkins, Morgane Vacher, Michael J. Bearpark, and Michael A. Robb. Nuclear spatial delocalization silences electron density oscillations in 2-phenyl-ethyl-amine (PEA) and 2-phenylethyl-N,N-dimethylamine (PENNA) cations. *Journal of Chemical Physics*, 144(10):104110, mar 2016. ISSN 00219606. doi: 10.1063/1.4943273. URL `http://aip.scitation.org/doi/10.1063/1.4943273`.

[6] Morgane Vacher, Michael J. Bearpark, Michael A. Robb, and João Pedro Malhado. Electron Dynamics upon Ionization of Polyatomic Molecules: Coupling to Quantum Nuclear Motion and Decoherence. *Physical Review Letters*, 118(8):083001, feb 2017. ISSN 10797114. doi: 10.1103/PhysRevLett.118.083001. URL `https://link.aps.org/doi/10.1103/PhysRevLett.118.083001`.

[7] Morgane Vacher, Michael J. Bearpark, and Michael A. Robb. Communication: Oscillating charge migration between lone pairs persists without significant interaction with nuclear motion in the glycine and Gly-Gly-NH-CH3 radical cations. *Journal of Chemical Physics*,

140(20):201102, may 2014. ISSN 00219606. doi: 10.1063/1.4879516. URL http://aip.scitation.org/doi/10.1063/1.4879516.

[8] Alexander I Kuleff and Lorenz S Cederbaum. Ultrafast correlation-driven electron dynamics, jun 2014. ISSN 13616455. URL http://stacks.iop.org/0953-4075/47/i=12/a=124002?key=crossref.e21d15de7e171e6ebe378451ffbb8bf8.

[9] M Lezius, V. Blanchet, Misha Yu Ivanov, and Albert Stolow. Polyatomic molecules in strong laser fields: Nonadiabatic multielectron dynamics. *Journal of Chemical Physics*, 117 (4):1575–1588, 2002. ISSN 00219606. doi: 10.1063/1.1487823. URL https://doi.org/10.1063/1.1487823.

[10] Chunlei Guo, Ming Li, and George N Gibson. Charge asymmetric dissociation induced by sequential and nonsequential strong field ionization. *Physical Review Letters*, 82(12): 2492–2495, 1999. ISSN 10797114. doi: 10.1103/PhysRevLett.82.2492.

[11] J. Breidbach and L. S. Cederbaum. Migration of holes: Formalism, mechanisms, and illustrative applications. *Journal of Chemical Physics*, 118(9):3983–3996, mar 2003. ISSN 00219606. doi: 10.1063/1.1540618. URL http://aip.scitation.org/doi/10.1063/1.1540618.

[12] Joseph Duris, Siqi Li, Taran Driver, Elio G. Champenois, James P. MacArthur, Alberto A. Lutman, Zhen Zhang, Philipp Rosenberger, Jeff W. Aldrich, Ryan Coffee, Giacomo Coslovich, Franz Josef Decker, James M. Glownia, Gregor Hartmann, Wolfram Helml, Andrei Kamalov, Jonas Knurr, Jacek Krzywinski, Ming Fu Lin, Jon P. Marangos, Megan Nantel, Adi Natan, Jordan T. O'Neal, Niranjan Shivaram, Peter Walter, Anna Li Wang, James J. Welch, Thomas J.A. Wolf, Joseph Z. Xu, Matthias F. Kling, Philip H. Bucksbaum, Alexander Zholents, Zhirong Huang, James P. Cryan, and Agostino Marinelli. Tunable isolated attosecond X-ray pulses with gigawatt peak power from a free-electron laser. *Nature Photonics*, 14(1):30–36, jan 2020. ISSN 17494893. doi: 10.1038/s41566-019-0549-5.

[13] Alberto A Lutman, Timothy J Maxwell, James P. MacArthur, Marc W Guetg, Nora Berrah, Ryan N Coffee, Yuantao Ding, Zhirong Huang, Agostino Marinelli, Stefan Moeller,

and Johann C.U. Zemella. Fresh-slice multicolour X-ray free-electron lasers. *Nature Photonics*, 10(11):745–750, 2016. ISSN 17494893. doi: 10.1038/nphoton.2016.201. URL www.nature.com/naturephotonics.

[14] Bridgette Cooper, Přemysl Kolorenč, Leszek J Frasinski, Vitali Averbukh, and Jon P Marangos. Analysis of a measurement scheme for ultrafast hole dynamics by few femtosecond resolution X-ray pump-probe Auger spectroscopy. *Faraday Discussions*, 171:93–111, 2014. ISSN 13645498. doi: 10.1039/c4fd00051j.

[15] J. D. Bozek. AMO instrumentation for the LCLS X-ray FEL. In *European Physical Journal: Special Topics*, volume 169, pages 129–132. Springer, may 2009. doi: 10.1140/epjst/e2009-00982-y.

[16] S. P. Hau-Riege, R. M. Bionta, D. D. Ryutov, and J. Krzywinski. Measurement of x-ray free-electron-laser pulse energies by photoluminescence in nitrogen gas. *Journal of Applied Physics*, 103(5):053306, mar 2008. ISSN 00218979. doi: 10.1063/1.2844478. URL http://aip.scitation.org/doi/10.1063/1.2844478.

[17] Yuantao Ding, Franz-Josef Decker, V A Dolgashev, Josef Frisch, Zhirong Huang, Patrick Krejcik, Henrik Loos, A Lutman, Agostino Marinelli, T J Maxwell, Daniel Ratner, James Turner, Juwen Wang, M Wang, James Welch, Juhao Wu, Slac National, Menlo Park, and Christopher Behrens. Results From the Lcls X-Band Transverse Deflector With Femtosecond Temporal Resolution. In *27th International Linear Accelerator Conference*, number 1, pages 2–6, 2014. URL http://inspirehep.net/record/1363526/.

[18] Patrick Krejcik, F J Decker, Y Ding, J Frisch, Z Huang, J Lewandowski, H Loos, J Turner, M H Wang, J Wang, and Others. Commissioning the new LCLS X-band transverse deflecting cavity with femtosecond resolution. *Proceedings of IBIC2013, Oxford, UK*, 2013.

[19] Yaron Bromberg, Ori Katz, and Yaron Silberberg. Ghost imaging with a single detector. *Physical Review A - Atomic, Molecular, and Optical Physics*, 79(5):053840, may 2009. ISSN 10502947. doi: 10.1103/PhysRevA.79.053840.

[20] Siqi Li, Taran Driver, Oliver Alexander, Bridgette Cooper, Douglas Garratt, Agostino

Marinelli, James P. Cryan, and Jonathan P. Marangos. Time-resolved pump-probe spectroscopy with spectral domain ghost imaging. *Faraday Discussions*, 228(0):488–501, may 2021. ISSN 13645498. doi: 10.1039/d0fd00122h.

# Chapter 5

# Towards X-ray spectroscopy in liquid targets

The previous chapter demonstrated the use of ultrafast spectroscopy in isopropanol vapour. Although that study provides insight into electron dynamics and helps to advance our general understanding, vapourised isopropanol is not of specific interest to many applications. Many systems are of more interest due to their role in chemistry, and most chemistry occurs in the liquid or solution phase. This presents a challenge for X-ray science due to the difficulties in delivering liquid targets in vacuum. Liquid cells with windows on the order of 100 nm thick have been successfully used for soft X-ray absorption measurements [1], but are costly to X-ray flux and are unsuitable for most pump-probe measurements due to damage from strong-field pump and very low transmission of UV pumps.

More recently, free-flowing in-vacuum liquid targets have been designed. This chapter focusses on the delivery of these targets with specific reference to time-resolved (pump-probe) XAS measurements. Section 5.1 looks at the necessary features of a liquid target, and summarises by identifying a few of the available solutions. Of those solutions, two are particularly suitable for the applications, one which is commercially available and one which can be fabricated in-house. Section 5.2 details the methods used for fabricating the latter; Section 5.3 covers the development of a vacuum chamber for liquid phase XAS; and finally, Section 5.4 discusses the

design and commissioning of a flatfield spectrometer for XAS and presents an XAS spectrum of liquid ethanol.

## 5.1 Liquid Target Requirements

An important factor in the success of any absorption measurement is the thickness of sample being measured. The sample being studied must be thick enough that the length of the beam-path within the sample, $L$, divided by the attenuation length, $\mu^{-1}$, provides significant contrast between the absorbed and unabsorbed spectra. However, the absorption length must be small enough that at the most strongly attenuated photon energy of interest, the measured signal is resolvable above any detection noise. In a time resolved measurement, it is the difference in optical density (absorption) that is of importance. The measurable change in optical density is determined by the resolution of the measurement. Therefore, an estimation of the required thickness to maximise resolution is required.

The transmission of an X-ray pulse through sample at a given frequency, $\omega$, in an ideal measurement is governed by Beer's law,

$$T = \frac{A_T(\omega)}{A_0(\omega)} = e^{-\mu L}, \tag{5.1}$$

where $A_T(\omega)$ and $A_0(\omega)$ are the amplitudes of the transmitted and incident pulses respectively, and $\mu$ is the attenuation coefficient. $\mu$ is proportional to the cross-sections for transitions in the sample and is therefore the quantity to be measured. Simply rearranging,

$$\mu(\omega) = \frac{1}{L} \ln \frac{A_0(\omega)}{A_T(\omega)}. \tag{5.2}$$

Therefore, $\mu$ can be determined for a given frequency if the spectral amplitude of the incident and transmitted pulse is known. Changes in the attenuation coefficient due to a pump are similar, but with the input and transmitted amplitude replaced by the unpumped and pumped sample respectively, and the same arguments hold.

The thickness of a target should be chosen to minimise the fractional error in measuring $\mu$. Specifically, the thickness of the target should be chosen to minimise the standard error of a maximum likelihood estimate of $\mu$, which is related to the variance, $\mathrm{Var}\,(\mu)$, and number of measurements, $N$, by

$$\mathrm{SE}\,(\hat{\mu}) = \frac{\mathrm{Var}\,(\mu)}{\sqrt{N}} \tag{5.3}$$

Variance is introduced by errors which propagate from many sources. Firstly, coherent states of light are subject to poissonian counting statistics, and any measurement of the amplitude is therefore subject to a minimum error in its measurement. Additionally, any real detection method has error in the readout of the detector. These errors are of similar consequence and can combine to shot-for-shot noise, $\epsilon_{\mathrm{sfs}}$. Furthermore, it is not possible to simultaneously measure $A_0$ and $A_T$. Instead, measurements of the spectrum are made with and without sample alternately (or pumped and un-pumped) and it is assumed that consecutive spectra are on-average the same. As a consequence of the lab-time separation of these measurements, any instability in the XUV source will lead to a discrepancy in the measured incident amplitude and the actual amplitude. If the fractional error between these two values is $\epsilon_{\mathrm{stab}}/A_0(\omega)$, the measurement from one sequence of consecutive spectra is given by

$$\mu_i = \frac{1}{L} \ln \frac{A_0(\omega) + \epsilon_{0,\mathrm{sfs},i} + \epsilon_{\mathrm{stab},i}}{A_T(\omega) + \epsilon_{T,\mathrm{sfs},i}}, \tag{5.4}$$

This maximum likelihood estimator of $\mu$ after $N$ repeats is given by

$$\hat{\mu} = \frac{1}{L} \ln \frac{\sum_i A_0(\omega) + \epsilon_{0,\mathrm{sfs},i} + \epsilon_{\mathrm{stab},i}}{\sum_i A_T(\omega) + \epsilon_{T,\mathrm{sfs},i}}. \tag{5.5}$$

Its variance is

$$\begin{aligned}
\mathrm{Var}(\mu) &= \left(\frac{1}{L}\right)^2 \left( \frac{\mathrm{Var}\,(\epsilon_{0,\mathrm{sfs}}) + \mathrm{Var}\,(\epsilon_{\mathrm{stab}})}{A_0(\omega)^2} + \frac{\mathrm{Var}\,(\epsilon_{0,\mathrm{sfs}})}{A_T(\omega)^2} \right) \\
&= \frac{1}{(LA_0)^2} \left( \mathrm{Var}\,(\epsilon_{\mathrm{stab}}) + \left(1 + \frac{1}{T^2}\right) \mathrm{Var}\,(\epsilon_{0,\mathrm{sfs}}) \right) \\
&= \frac{1}{(LA_0)^2} \left( \mathrm{Var}\,(\epsilon_{\mathrm{stab}}) + \left(1 + e^{2\mu L}\right) \mathrm{Var}\,(\epsilon_{0,\mathrm{sfs}}) \right).
\end{aligned} \tag{5.6}$$

This is in line with intuition: for very low thicknesses, the error is resulting in a greater change between the sample-in and sample-out spectra than the absorption; and for long lengths, the sample-in spectra have intensity comparable to, or smaller than the shot-for-shot noise which dominates the error in the result. A balance must therefore be found which depends on the relative magnitude of the errors and $A_0$.

These are estimated from test data of harmonic spectra at the sulphur L-edge and carbon K-edge. The magnitude of $\epsilon_{\text{stab}}$ depends on the time between acquisitions and the frequency of drifts in the harmonic spectrum. For 1% energy intervals at the sulphur L-edge and carbon K-edge, the magnitude of drifts increases below approximately 5 Hz [2]. Acquiring at 5 Hz therefore gives most of the benefit in reducing the drift whilst minimising the ratio of readout noise to signal. The poissonian component of $\text{Var}\left(\epsilon_{\text{sfs}}\right)$ is known from the number of photons. For 200 ms exposures (i.e. at 5 Hz), there are approximately 8000 photons in a 1% bandwidth at the sulphur L-edge and 800 photons in a 1% bandwidth at the carbon K-edge. Accounting for the different number of pixels in each spectral region, the read-out noise in the CCD in its 1 MHz readout mode is the equivalent of 117 photons at the sulphur L-edge and 148 photons at the carbon K-edge. The remainder can be attributed to drift, and for 200 ms exposures has a standard deviation of 80 photons at the sulphur L-edge and 350 photons at the carbon K-edge.

Figure 5.1 shows how the fractional error varies as a function of the transmission for a range of input errors. The measured values of $\text{Var}\left(\epsilon_{\text{stab}}\right)$ and $\text{Var}\left(\epsilon_{\text{sfs}}\right)$ are $0.015A_0^2$ and $0.065A_0^2$ at the sulphur L-edge and $0.019A_0^2$ and $0.42A_0^2$ at the carbon K-edge. At both edges, the optimum transmission is approximately 33%, where the signal to noise ratio is 7.5% at the sulphur L-edge and 18.9% at the carbon K-edge. Given that typical absorption lengths of organic materials in the soft X-ray are between a few and ten micrometres off resonance and typically of the order of one micrometre on resonance, targets of this order are required. For example, isopropyl alcohol (IPA, $C_3H_8O$) has an attenuation length of $\approx 5\,\mu\text{m}$ at 190 eV [3], which is close to the sulphur L-edge and below the carbon K-edge.

Another important point to consider which limits the thickness of a target is temporal walk-off. Pump-probe experiments rely on a a fixed temporal spacing between the pump and probe,

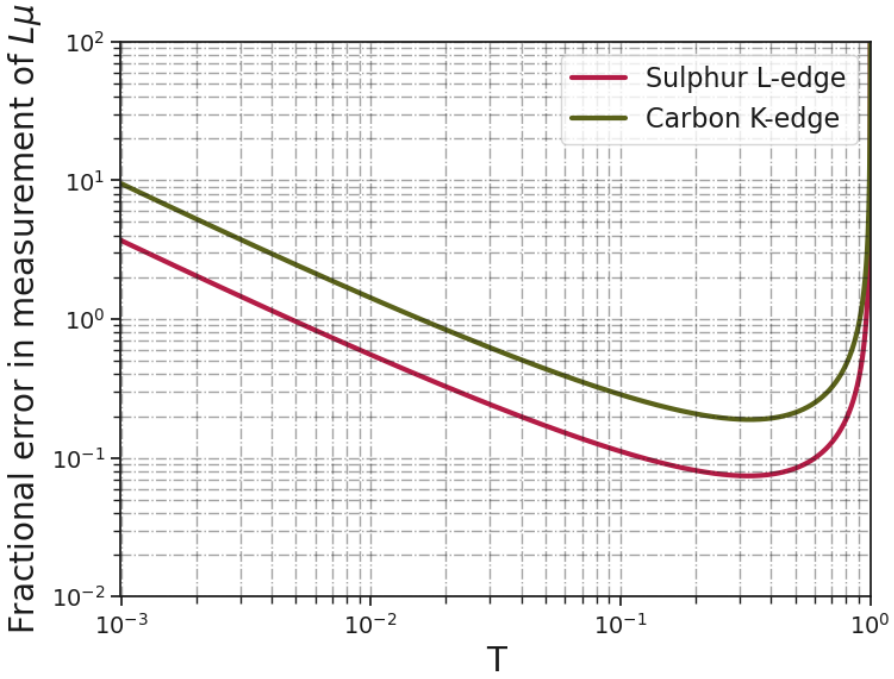



Figure 5.1: Calculated fractional error in a 200 ms measurement of $\mu L$ (i.e. absorption) in a 1% bandwidth range, as a function of transmission, $T$, at the sulphur L-edge and carbon K-edge. In both cases, error is minimised for $T$ at approximately 33% and a workable range is roughly between 10 and 50%.

which must be maintained throughout the sample. However, given that the pump and probe have wavelengths that differ by orders of magnitude, their refractive indices in a target will vary significantly and the pulses will separate, limiting temporal resolution. For example, taking typical refractive indices to be approximately 1 and 1.5 for the probe and pump respectively, the temporal walk-off in the time taken for a probe to traverse a one micron thick sample is 1.6 fs. This also limits the sample thickness to approximately microns, with the exact amount depending on the resolution required for the experiment, the length of the pump and probe pulses, and the refractive indices.

In addition to the thickness of the target, there are other important design considerations. Firstly, it is necessary that the jet is flat over the size of the incident X-ray beam. If the jet is not flat, the wavefront of the X-rays will be distorted and will reduce the resolution of the spectrometer. It is also important that the liquid is collectable, and as previously discussed, the target must be delivered in vacuum. Therefore, it is necessary that the liquid can be efficiently collected whilst maintaining a vacuum. With a thin, stable cylindrical jet of liquid, this can

be achieved using a cone with a small hole underneath the jet and pump to remove liquid and maintain a vacuum. Finally, it is also desirable that the liquid have a high enough velocity that each successive laser shot irradiates a new portion of the sample - i.e. such that the target can be considered 'self-healing'. Taking a conservative estimate of beam size to be 1 mm and a pulse repetition rate of 1 kHz, this then requires a velocity of at least $1\,\mathrm{m\,s^{-1}}$.

### 5.1.1 Methods of creating micrometer flatjets

There are a number of methods available for the creation of the thin, flat, free-flowing liquid targets required, which can be referred to as flatjets. They each work on a similar principle from fluid dynamics, which has been known since the early work of Taylor [4]. As two equal cylindrical jets combine, their momentum components on the axis of the collision cancel out, and due to the incompressibility of the liquid, momentum is produced in orthogonal directions. The result is a spreading of the liquid into a thin sheet. The sheet then reforms into a leaf shape, due to the surface tension of the liquid. This can be scaled to the micro-scale, with the initial momentum, specific geometry and physical properties of the liquid determining the properties of the sheet. An in-depth analysis can be found in [5].

The earliest published example is from 2015, which most closely follows the work of Taylor, by colliding micrometer thin cyclindrical jets [6]. Whilst this technique is capable of producing suitable flatjets, there are simpler methods available.

Galinis et al. developed a simpler method [7], which uses the geometry of a nanofabricated nozzle to emulate the flow of a colliding jet. Internal walls of the nozzle direct opposing liquid flows such that they meet at the nozzle exit, and a flatjet is formed. The nozzles are referred to as fan spray nozzles, due to their similarity with macroscopic nozzles of the same name used in a number of engineering applications which require large surface area to volume ratios [8].

Recently, an alternative commercially available method developed by the DePonte group [9] has become available. The principle is similar, requiring a transverse momentum to 'open' the leaf; however, the transverse momentum for the nozzles is created instead by micro-channels of high pressure gas interfacing with a cylindrical microjet at an angle. The gas and liquid channels are

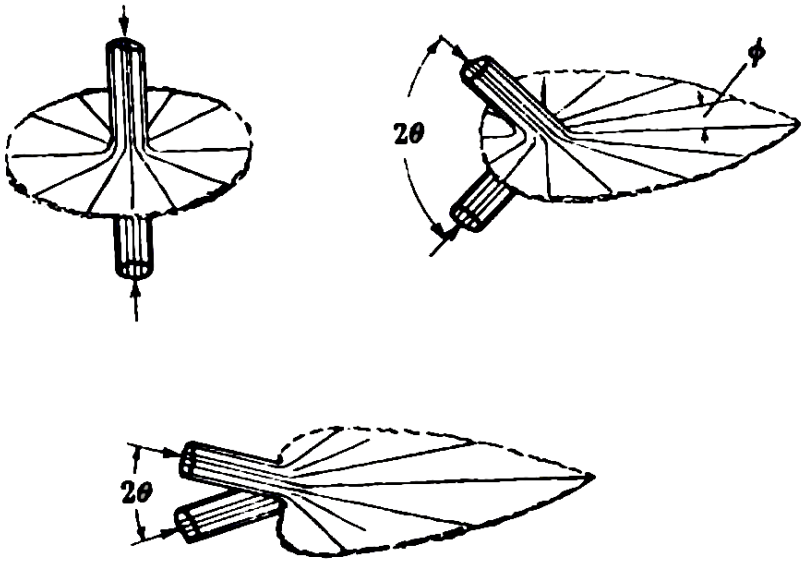



Figure 5.2: Sketches of macroscopic liquid sheets formed by the collision of two macroscopic cylindrical jets, for three difference collision angles, reproduced from [4]. The principle for microscopic jets is similar, in the low angle regime of the bottom sketch. Figure reproduced with permission from the license holder Royal Society (Great Britain).

etched into glass, using the existing technology for microfluidics. The properties of the jet can be controlled by the relative flow volumes in the gas and liquid channels. These nozzles are referred to as gas dynamic nozzles and are fabricated in nano-fluidic glass devices: two glass substrates have channels etched into them on their surface, and the etched surfaces are adhered to form channels at their interface. A through-hole is etched into one the halves for connecting the gas and liquid channels. These small liquid channels require low flow volumes but high pressures ($\sim$10 bar), which can be generated using an HPLC pump. An interesting second use of these nozzles is that if liquid is projected from the nominal gas channels, due to the geometry of the nozzles, they will collide. These colliding cylindrical liquid microjets will also form a flat liquid sheet. This offers another possibility for creating flatjets.

The gas dynamic nozzles in the colliding geometry and the fan-spray nozzles are particularly suited for XAS measurements. Neither require alignment, other than their positions and rotation, and are capable of producing stable and repeatable flatjets; they also do not require the additional use of gas, which will also absorb; and they are capable of producing optically flat sheets on the order of 1 µm. There are differences in the flatjets they produce, which are explained in detail in [10] along with details on the operation of those flatjets. The fan spray

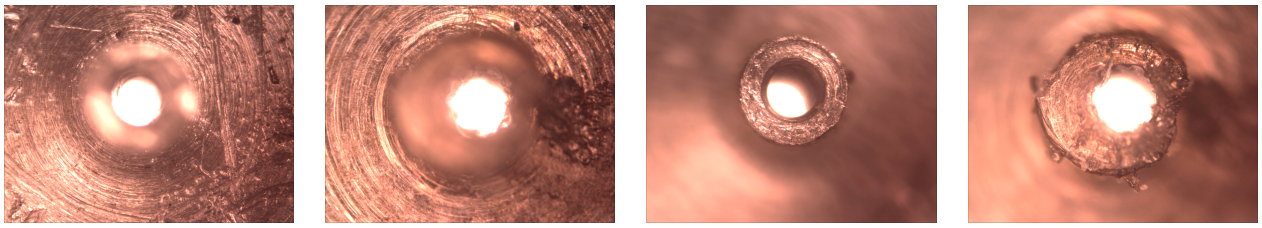
nozzles produce larger flatjets, approximately by a factor of 2 in each dimension. The structure of the fan spray nozzles is also designed to guide the expansion of the liquid sheet after the collision, which dampens surface wave formation, but also means that the internal geometry must be optimised for the liquid physical properties and cannot be used generically.

Fan spray nozzles were used for all of the measurements shown in Chapter 6 and gas dynamic nozzles in the colliding geometry were used for the absorption measurements shown in Section 5.6.

## 5.2 Nano-fabrication of fan spray type nozzles

The manufacture of fan spray nozzles was completed via 3D printing using a photoresist. A photoresist is a material which changes either its structural or chemical properties, or both, in response to exposure to light. They are commonly used in photolithography, most notably for the microfabrication of semiconductor integrated circuits. For this work, the photoresist IP-S (Nanoscribe GmbH) was used. IP-S is a viscous liquid monomer which polymerises when it interacts with 390 nm light. It is a negative resist which, when polymerised, is rigid and cannot be dissolved in common solvents. The typical method is for a photoresist to be applied to a substrate, and for designated areas (typically controlled using a mask) to be exposed to light. The substrate and resist are then developed in solvent to remove the unexposed (for a negative resist) photoresist, leaving a 2 dimensional pattern on the substrate.

Extending this method to the manufacture of 3D structures poses some technical difficulties in exposing a precise volume within a thick layer of resist. Clearly, a mask cannot be used. It then seems intuitive to use the focus of a laser to create high resolution structures. However, the rate of one-photon polymerisation is linearly dependent on the laser intensity and despite a laser being most intense at its focus, there is still a appreciable amount of polymerisation beyond the Rayleigh range. To solve this problem, two-photon polymerisation using a 780 nm laser creates a quadratic dependence on the laser intensity, which is sufficient to confine polymerisation to a spot smaller than the focus.



(a) (b) (c) (d)

Figure 5.3: Microscope images of two substrates under a 10× microscope objective. Four images are shown due to the depth of field achievable with the microscope only allowing viewing of the base of the substrate or the peaked structure. (a) and (b) show the base of the substrates drilled on aluminium and laser cut in stainless steel respectively. In aluminium, some scratches and digs are visible; however, in general the surface is is smoother than in stainless steel, which often features damage from the laser drill as can be seen on the right of (b). (c) and (d) show microscope images of the same substrates as (a) and (b) respectively, but with the microscope focus further from the substrate, on the top of the peak structure. Clearly, the hole formed in the aluminium substrate is more symmetric; in (d), crater-like damage from the laser cutting has cause a thicker, uneven edge.

The method for producing liquid flat sheet nozzles using such a printer was developed in house by Galinis et al. [7] and works as follows: Firstly, due to the long time taken to print large structures, mountable substrates for the nozzles were made in the physics department workshop at Imperial College. In order to make the substrates, a 150 µm hole is made in sheet of aluminium. A lathe is then used to form a small peak around the hole and the substrate is then milled to form an oval, 1 mm by 3 mm. The use of a 150 µm drill-bit is technically challenging, so attempts were made to laser drill holes on stainless steel substrates, with the hole drilled after forming the peak and milling. Figure 5.3 shows microscope images of the drilled and laser cut substrates, for comparison. Though offering a simpler method for manufacture, the laser cutter used creates a less precise hole than the drilled holes in aluminium and most samples are unusable.

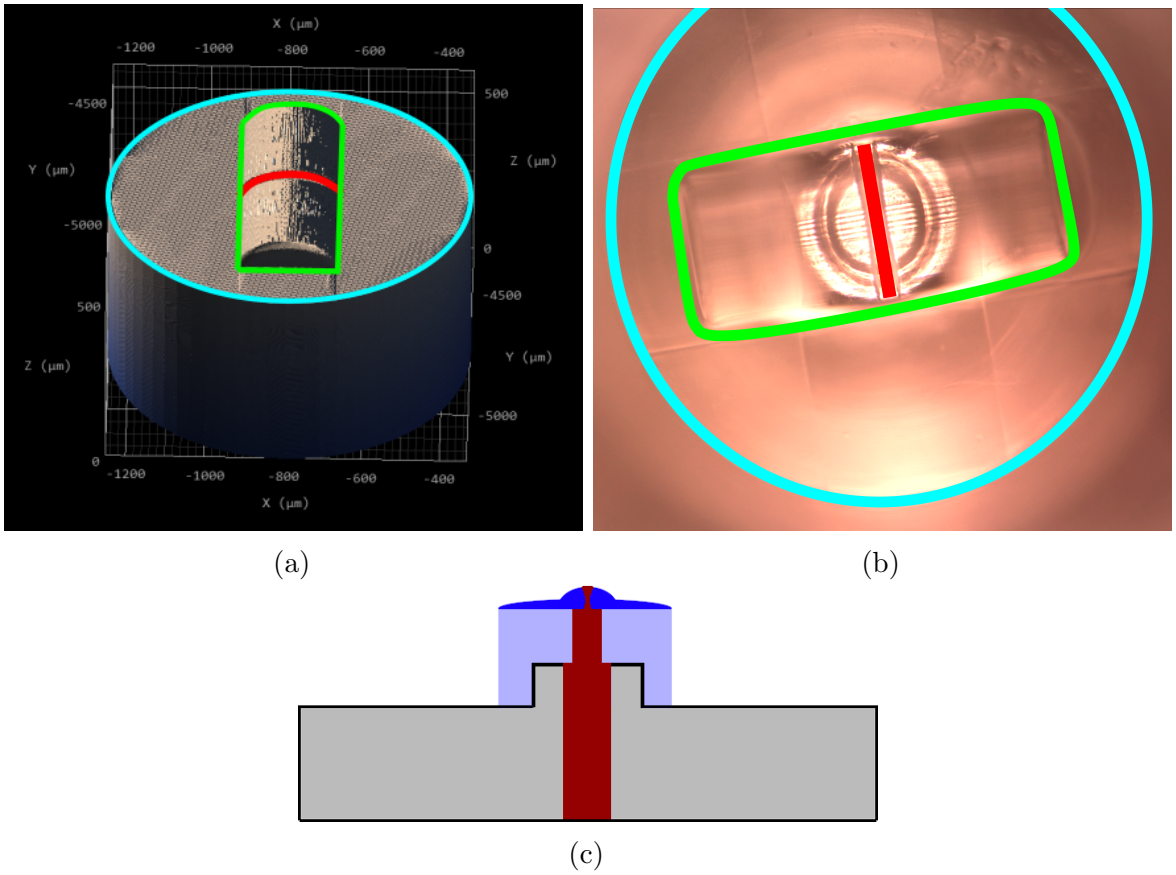
Up to eight substrates are then loaded into a larger mount, which in turn fits the specifications for mounting into the 3D printer (Nanoscribe GmbH). The substrates are cleaned by submerging in isopropanol for approximately 2 minutes and dried with nitrogen gas before coating with a thick layer of the photoresist and mounted with the substrate inverted. A microscope objective is then raised from beneath the substrates into contact with the photoresist. The substrate is then illuminated from below and can be viewed via a camera behind the microscope objective.

The printing of the nozzles is done in a layer-by-layer fashion. First, the focus of the laser is raised to the highest point in the job, in contact with the substrate. It then prints the lowest layer (when turned upright) of the nozzle design, then the focus is lowered by less than the beam focus size, and the process repeats.

Particular care must be taken in the initial stages to ensure adhesion of the nozzle to the substrate. During the printing process, the position of the interface between the photoresist and the substrate is found using interferometry to detect a step in refractive index. With the substrates used, this can cause issues due to the rough metallic surface from machining (typically, glass or similar substrates are used in the printers applications). The printer must therefore be guided to a region close to the interface within the script specifying the printing job.

It is also necessary to add some tolerance to the interface, such that the printing begins behind the surface. This is because the laser focus is most intense at its centre, so the printed structure may not adhere properly if the focus is even slightly misaligned from the surface. Furthermore, the interface must be found at the appropriate position; the base of the nozzle is relatively large and the height of the interface relative to the laser focus might vary significantly over its area. It is therefore important that for the large base, the interface is found at the lowest point and that there is enough redundant height in the nozzle support structure such that the bottom section can be printed behind the surface.

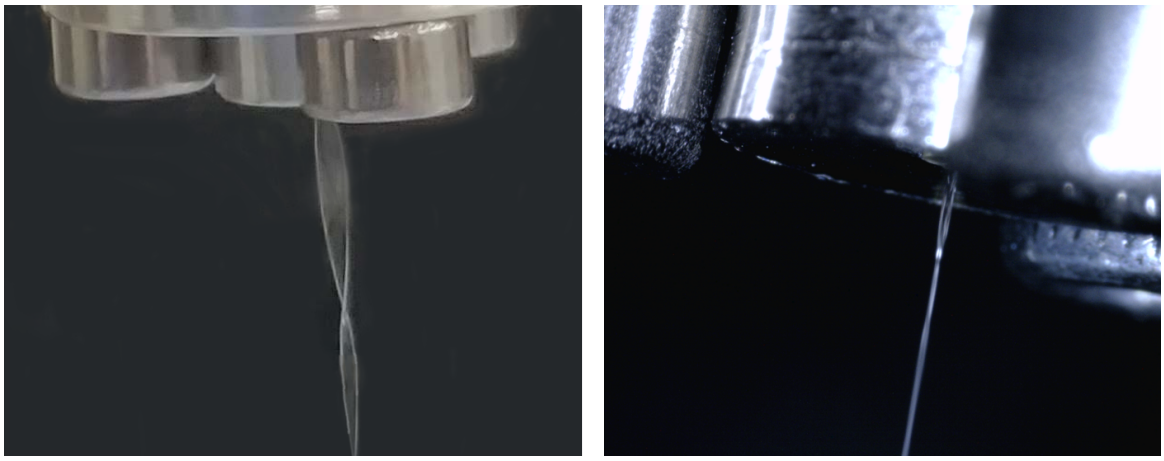
Once the nozzles are printed, they are left in propylene glycol methyl ether acetate (PGMEA) solvent for twenty minutes so that the unpolymerised photoresist can dissolve. They are then rinsed with isopropyl alcohol for two minutes and dried using clean nitrogen gas. Printing structures on the scale of the nozzles takes approximately eight hours per nozzle. For this reason, attempts were also made to greatly reduce the printing time by instead printing a scaffolding for the structure with a surface layer to containing monomer photoresist. After printing and removing the external photoresist, the nozzles can then be baked at 200 °C for thirty minutes to polymerise the remaining monomer contained within the scaffolding. The nozzles are then inspected under a microscope. Figure 5.4 shows an annotated CAD drawing and microscope image of a nozzles for comparison as well as a diagram showing how the nozzles are positioned




(a) (b)

(c)

Figure 5.4: A comparison between a 3D CAD rendering of a nozzle (a) and a microscope image of a completed nozzle, taken from an aerial view and illuminated from below (b). Highlighted in both cases are three components of the nozzle structure. They are: (cyan) The support structure, which adheres to the substrate; (green) the main structure of the slit; and (red) the slit itself, positioned on top of the substrate hole, visible on the microscope image as the bright area underneath the slit. (c) Diagram, showing a not-to-scale cross section of a nozzle printed onto a substrate. In this diagram the flow direction would be from bottom to top. The substrate (grey) has a hole drilled through it (red) and a peaked region on the upper surface. The nozzle structure shown in (a) is printed onto the top of the substrate (blue) and also has a hollow channel with internal structure at the exit designed to create a flat liquid sheet.



(a) (b)

Figure 5.5: (a) Two flat sheets of isopropanol in a chain produced from a 3-D printed nozzle. Similar jets have been 1-2 µm thick as measured via white light interferometry and are optically flat as measured with monochromatic interferometry. (b) A small water liquid sheet formed by a 3-D printed nozzle. For each photograph, the background has been removed digitally.

on the substrates.

Several issues in the printing need to be considered, including:

- Detachment of nozzles from their substrates. This can be caused by a number of things and usually solved by finding the appropriate depth at which to print onto the substrates for strong adhesion and by ensuring that the polymer being used has not decayed.

- Variability in the nozzle slit (exit) width. This was solved by adding additional and longer wash cycles in the development of the nozzles.

- Very rapid blocking of nozzles due to small particles in the back-stream of the liquid delivery system. This has been mostly resolved through the addition of extra microparticle filters, thorough rinsing of the lines at high pressure, and sonication of parts in the system after the filters.

Figure 5.5a shows an isopropanol flatjet produced by a fan spray nozzle. Water flatjets can also be produced; they are smaller in size, only a few square millimetres, which will make precise alignment critical for XAS measurements. Figure 5.5b shows a typical water jet.

## 5.3 Development of a target chamber for liquid-phase NEXAFS

The mass attenuation coefficient, $\mu/\rho$, of air between 100 eV and 600 eV ( photon energies spanning the most important atomic edges) is of the order of $1 \times 10^3\,\mathrm{m^2 kg^{-1}}$ [11]. Using Beer's law, the distance over which the signal would be attenuated to 0.1 % in air at atmospheric pressure ($\rho = 1.225\,\mathrm{kg}$) is therefore <5 mm. According to Boyle's and Avogadro's gas laws, the pressure required to reduce the attenuation length to ∼10 m is $\sim 1 \times 10^{-1}$ mbar. Therefore, it is necessary for the jet to operate in a vacuum. This is technically challenging due to the fact the liquid jet itself contributes a significant amount of vapour to its surroundings, via both evaporation and imperfect collection of the liquid in any catcher. Water, for example, has a similar mass attenuation coefficient to air at the photon energies of interest, i.e. $\sim 1 \times 10^3\,\mathrm{m^2 kg^{-2}}$ [11].

As such, before any work could begin on X-ray experiments it was necessary to construct a purpose built vacuum chamber for liquid targets with affecting delivery and collection of the liquid target as well as sufficient pumping (through the use of turbomolecular pumps and liquid nitrogen cold traps) to maintain a low vacuum. A large (DN275CF) six-way-cross was used as the main structure for the chamber. Breadboards were clamped to the four horizontal elements of the cross, to be used for mounting optics or diagnostics. A $1360\,\mathrm{Ls^{-1}}$ capacity magnetically levitated turbomolecular pump (ATH1603M, Pfeiffer Vacuum) was mounted on one horizontal flange and on the opposite flange, a hatch was installed for ease of access when venting to access the chamber.

The other horizontal axis was aligned along the laser axis. Gate valves, pinholes, and differential pumping sections were installed at the laser entrance and exits. On the top flange a rotating adaptor flange was installed, and to that, a manipulator was added with 3 translational degrees of freedom. To this, a feed-through was installed for the liquid target, which then has full translational movement available to it and rotation around the vertical axis. This is necessary as the target must be aligned to the laser propagation axis, which is fixed by the pinholes at

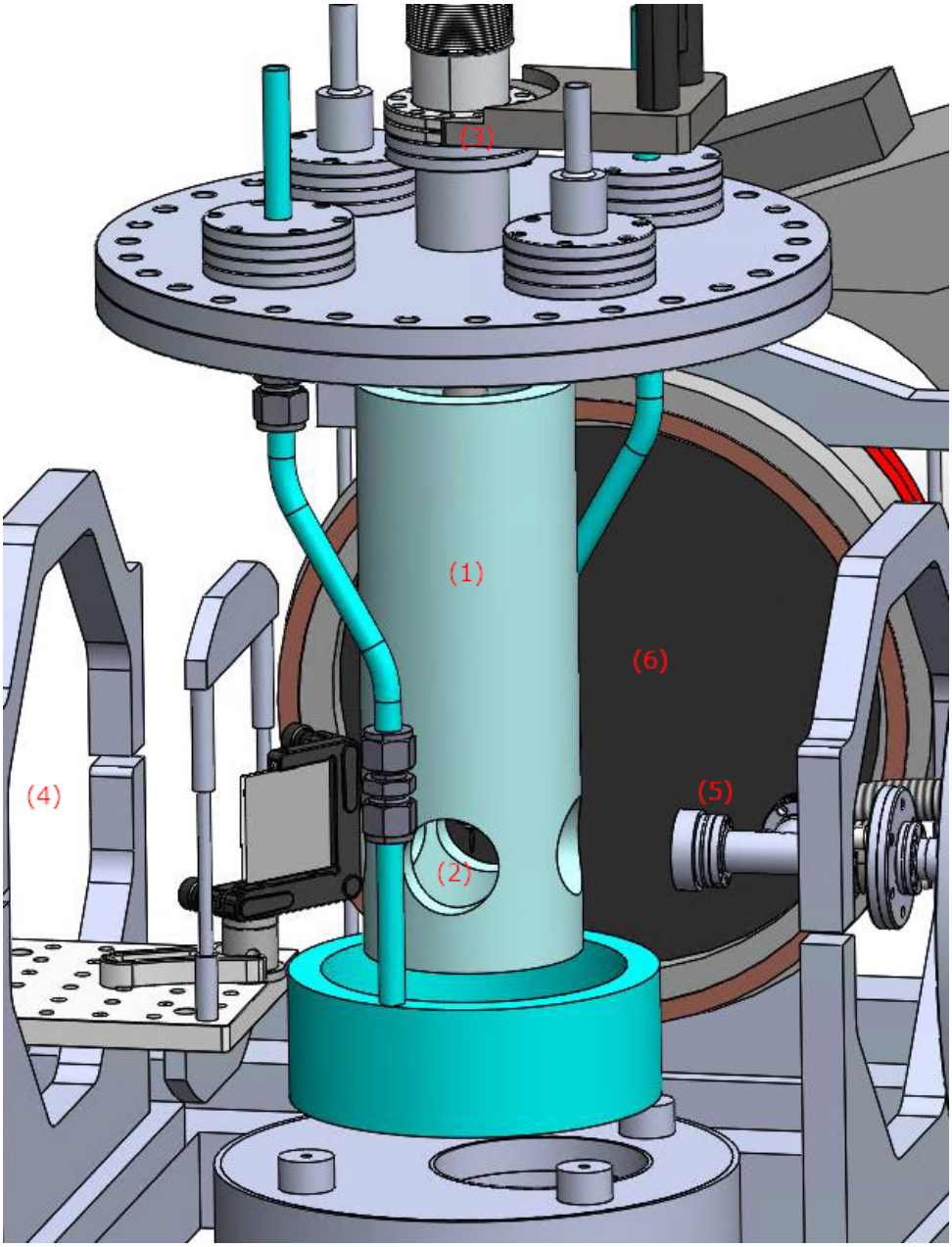



Figure 5.6: An annotated diagram of the installations on the six-way-cross target chamber to be used for liquid target NEXAFS. The perspective is that of the access hatch. A liquid nitrogen cold trap (1) encloses a liquid flat-sheet target (2) which is provided via a feed-through (3) on the top flange of the chamber, and is mounted on a manipulator for translation in three axes. The laser enters the chamber from the left (4), with a differential pumping section on the outside of the chamber, and exits via a pinhole (5) which connects to a differentially pumped tube-section. The chamber is pumped via a turbomolecular pump (6). Diagram courtesy of Clement Ferchaud.

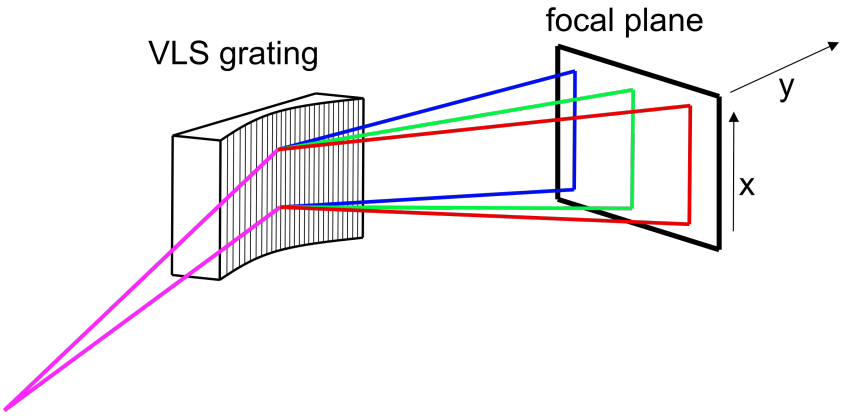



Figure 5.7: A diagram showing the working principle of a flatfield spectrometer. A variable line spacing reflective grating images broadband light originating from a point. The toroidal shape of the grating surface focuses in the horizontal axis, but adds wavelength dependent dispersion. In the vertical axis, each wavelength continues to disperse. Therefore, the grating maps each wavelength to a vertical line and with the correct line spacing and angle of incidence, $\alpha$, those lines form a flat plane.

the laser entrance and exit. On the bottom flange a similar translation stage was installed with a feed-through for the liquid target collector. Translation here allows the bottom flange to be aligned onto the liquid target. In the centre of the chamber, a cylindrical liquid nitrogen cold-trap was installed with feed-throughs to the top flange which allow it to be filled with liquid nitrogen. The cold-trap encompasses the liquid targets to collect any evaporation. The cold-trap has four windows at the height of the liquid target, two to allow the laser through and to image the targets. Figure 5.6 is an annotated diagram of the installations on the six-way-cross chamber.

## 5.4 Design considerations for a flatfield spectrometer

The final step towards measuring liquid-phase XAS was the design and installation of an appropriate spectrometer. The proposed experiments are very 'photon-hungry' and the conversion efficiency of HHG, especially when pushing towards higher cut-off energies is very limited. Therefore, gains in signal and reduction in noise must be sought elsewhere and one of the prime candidates is the spectrometer.

The most suitable spectrometer for this application is a flatfield spectrometer which consists of a toroid-shaped reflective grating which images a point onto a plane (see Figure 5.7). The grating does not focus on one axis, typically the vertical axis ($x$), so preserves the divergence of the source in that direction. On the other axis, the toroidal shape of the grating images a point source of a single wavelength to a point. However, the horizontal ($y$) position of that depends on the wavelength of the light source, due to the diffraction from the grating. Note that $x$ and $y$ are defined relative to the grating surface, and are not the conventional coordinates for laser beam propagation (i.e. $z$ is not the direction of beam propagation). Importantly, gratings for these applications must image to a flat plane (the focal plane) as the detector will typically be flat; the diffraction adds an aberration to the focal plane which means that for gratings with linearly spaced grooves, this is not the case - they are astigmatic. In order to correct for this, gratings with variable line spacing (VLS) are employed [12, 13, 14]. To first order, the width of a groove spacing can vary linearly with position on the grating, according to

$$\sigma = \frac{\sigma_0}{1 + \frac{2b_2}{R} w} \tag{5.7}$$

where $\sigma$ is the groove spacing, $\sigma_0$ is the groove spacing at the centre of the grating, $R$ is the radius of curvature of the grating, w is the groove position, and $b_2$ determines the amount of variation applied. $b_2$ and R are the variable parameters which can be used to flatten the field for the desired wavelength range. Then, to calculate the focal curve, one can employ the equation derived in [14],

$$r' = \frac{rR\cos^2(\beta)}{r[(\cos\alpha + \cos\beta - 2(\sin\alpha - \sin\beta)b_2)] - R\cos^2\alpha}, \tag{5.8}$$

where $\alpha$ and $\beta$ are the angles of incidence and diffraction respectively.

Physical constraints were such that the working distance between the target/slit for imaging and the original grating was no longer suitable. For this reason, the focal plane of the grating was calculated at various incidence angles, $\alpha$. The results are plotted in Figure 5.8. As can be seen from this plot, the focal plane transverses approximately 1 cm over a typical energy range.

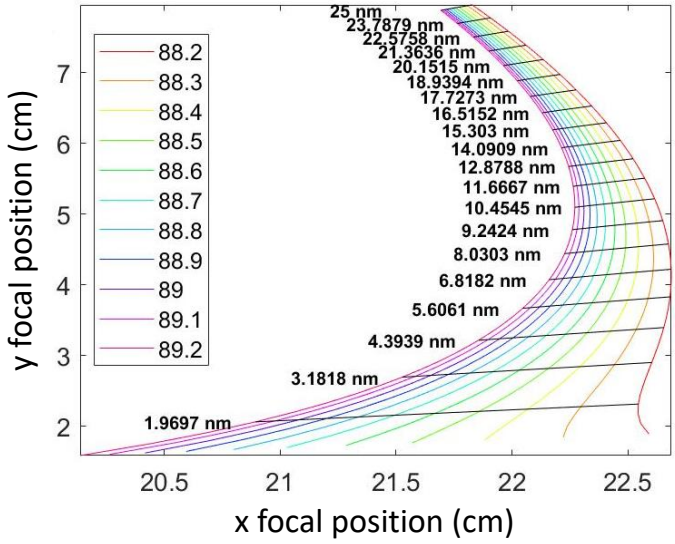


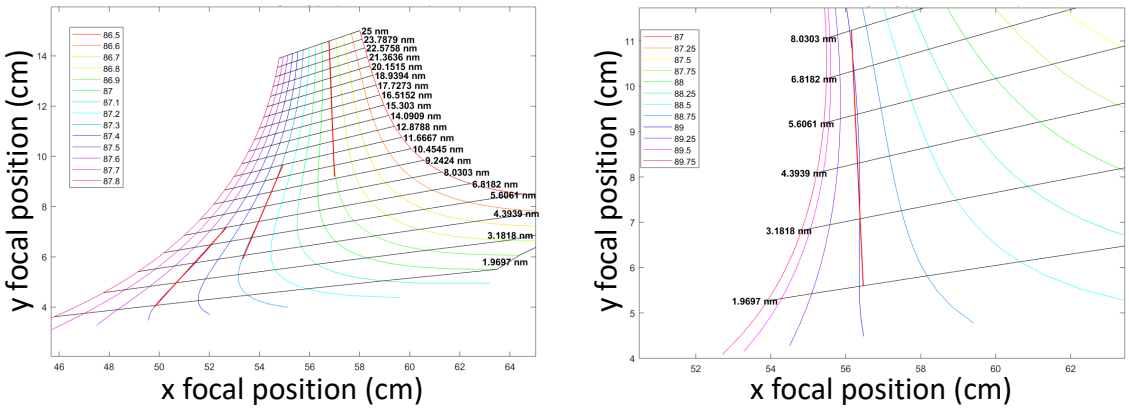

Figure 5.8: Focal plane calculations at different incident angles, $\alpha$, for the previously used VLS grating. The fixed parameter in these calculations is the distance from source to grating ($r + r' = 75\,\text{cm}$)

With a typical divergence of $\sim$2 mrad, distance from source to grating of 525 mm, and distance from grating to focal plane of 225 mm, the spot size is then approximately 50 µm for the most out of focus wavelengths.

Therefore, it was decided to install new flatfield gratings with longer working distances to optimise the spectrum. In practice, the choice of $b_2$ and $R$ is limited by what is commercially available; gratings made to a specification require a master grating to be manufactured and this multiplies the price. Two gratings supplied by Hitachi, Ltd. were identified as candidates for the new spectrometer. Figure 5.9 shows focal plane calculations for each of these gratings. The grating with 1200 average grooves per millimetre is ideally suited for the higher wavelengths of interest whilst the 2400 average grooves per millimetre grating is ideally suited down to 2 nm.

An additional check that had to be made was that the harmonic source would not clip on the gratings, reducing the transmission of harmonic flux. In order to do this, the divergence of the harmonic source was measured. This could be done by assuming the $x$ and $y$[1] divergence is the same and integrating over the spectral axis of an HHG spectrum; then, the divergence is the ratio between the size of the beam at the detector and the distance from the HHG source to the

[1]Here, the conventional coordinates for horizontal laser propagation are being used, where $z$ is the propagation axis, $x$ is the vertical axis, and $y$ is the transverse horizontal axis




(a) (b)

Figure 5.9: (a) Focal plane calculations at different incident angles, $\alpha$, for the upgraded 1200 lines per millimetre grating. The fixed parameter in these calculations is the distance from source to grating ($r + r' = 112.7\,\text{cm}$). The red lines identify flat portions of the focal plane with size of the detector (CCD chip). (b) Similar calculations for the upgraded 2400 lines per millimetre grating with the same fixed parameter.

detector. Figure 5.10 shows the $x$ profile of the HHG source at the detector. A divergence of 2.2 mrad was extracted from the $1/e^2$ half-width of a Gaussian fit.

Figure 5.11 shows the transmission, which only accounts for clipping of the beam, of the previous (left) and new (right) gratings for the current HHG source accounting for the divergence and spatial distribution (approx. Gaussian) of the HHG source. As can be seen, in the old configuration it is probable that there was a significant amount of clipping, which has also been improved by moving to larger gratings.

## 5.5 Experimental design overview

Figure 5.12 shows the designed implementation of all of the discussed elements in this section. Soft X-rays are generated in vacuum via HHG in a short interaction (few mm) target of $\sim$0.5 bar argon gas or $\sim$2 bar neon gas, using a few cycle NIR pulse (see Appendix A). The NIR is filtered from the X-rays using a thin metal film (aluminium, tin, zirconium, or titanium). A toroidal mirror, which is housed in its own chamber so that it can be differentially pumped, re-images the high harmonic source onto a liquid target. The liquid target is delivered from above via standard tubing supported by a rigid structure and mounted on a vacuum manipulator. Two

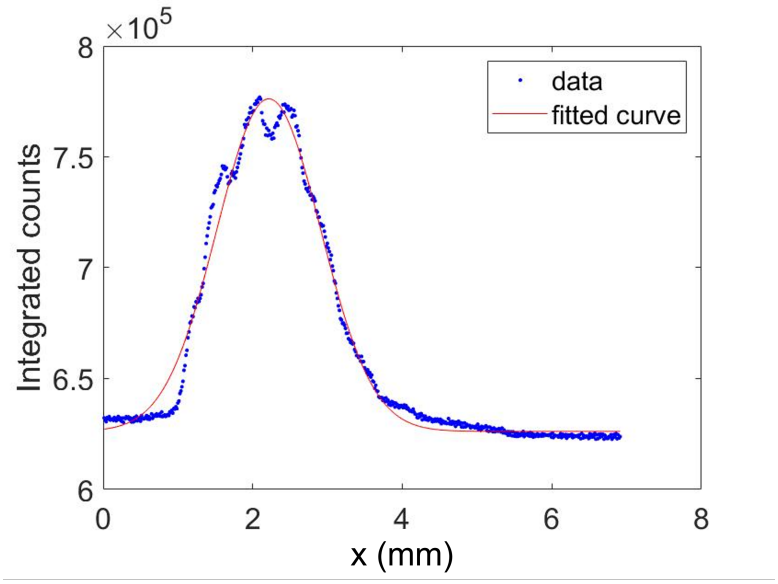
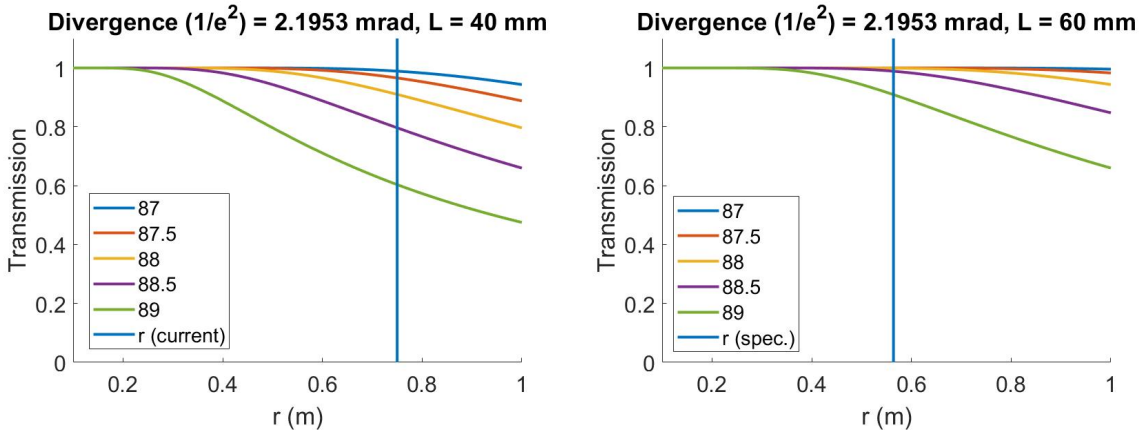



Figure 5.10: Transverse profile of the the high harmonics produced at the source planned for experiments. The Gaussian fit at the working distance from the source gives a $1/e^2$ divergence of 2.20 mrad.




(a) (b)

Figure 5.11: (a) Transmission, only considering loss from clipping) of the previous grating in use with the current HHG profile as a function of working distance, $r$. The blue line marks the current working distance. (b) A similar plot for the proposed gating, which is larger (length, $L$ =60 mm). The blue line marks the planned working distance.

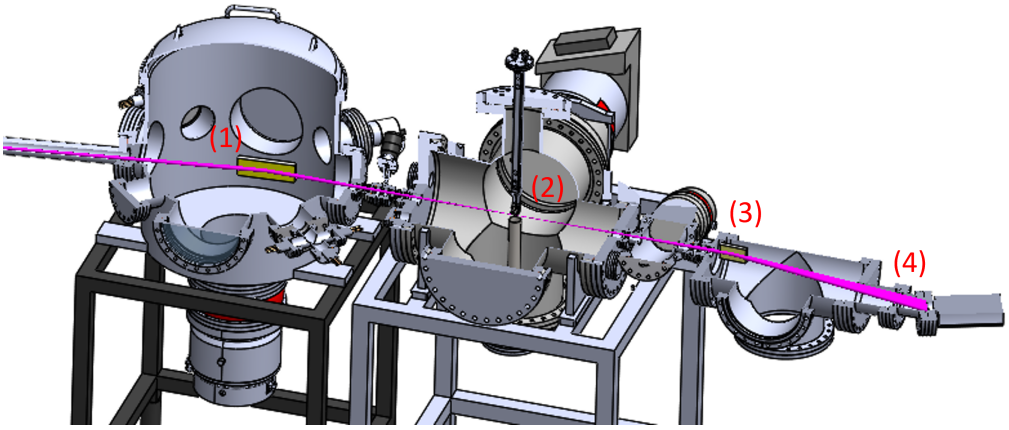



Figure 5.12: Design drawing (courtesy of Clement Ferchaud) of new experimental setup, including the original re-imaging optics (toroidal mirror chamber), the new six-way-cross target chamber, and the flat-field spectrometer. The VUV/X-ray source propagates from left to right and comes from the out-of-picture differentially pumped HHG source. It is then incident on a toroidal mirror, passes through a differential pumping section to the liquid target and is then propagates through another differential pumping section to the flat-field spectrometer. The toroidal mirror is positioned at (1), the target at (2), the flatfield grating at (3) and the detector at (4).

inline filters rated to 5 µm are upstream of the jet and the nozzle. The flange is rotatable to allow for the jet surface to be aligned to the laser axis as desired. After passing through the target, the high harmonic beam passes through a second differential pumping section, pumped via a $67\,\mathrm{L\,s^{-1}}$ turbomolecular pump (Pfeiffer HiPace 80), into the flatfield spectrometer. In Figure 5.12 the camera is shown to be mounted at a slight angle from the beam propagation. This is to accommodate for the fact that the flat-field plane is not along in the laser axis when observing some energy ranges in an optimal configuration. This can be seen from the left panel of Figure 5.9 in the higher energy (lower wavelength) regime.

## 5.6 Commissioning

The new flat field spectrometer was installed and adjustments made to the path lengths between chambers (using vacuum bellows) and absorption measurements were made on a thin film polymer, P3HT, which was used to optimise the spectrometer configuration to the correct energy range and best resolution. The new target chamber was then installed and again, adjustments to the alignment were made using P3HT as a test target to verify the spectrometer optimisation.

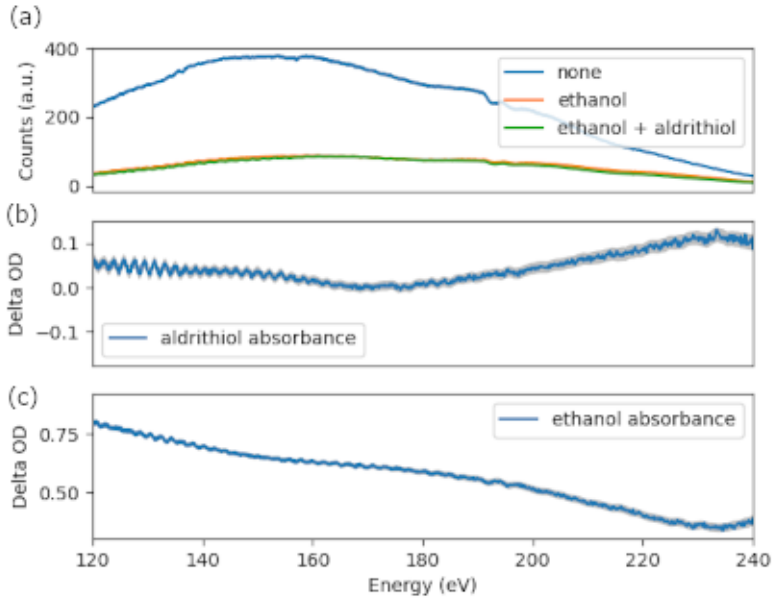



Figure 5.13: X-ray absorption of solvated aldrithiol close to and at the sulphur L-edge. (a) Soft X-rays generated via HHG in neon with no absorbing medium, liquid ethanol, and a solution of aldrithiol in ethanol. (b) The measured absorbance of aldrithiol and (c) ethanol.

The first liquid sample tested was ethanol, which has favourable properties. Its viscosity and surface tension are such that a large surface area, thin jet can be formed and its freezing point is far below zero. As such, freezing on the catcher due to evaporative cooling and radiative cooling from the cold trap is less of an issue. Figure 5.13 shows some first measurements made of the transmission of ethanol.

Whilst this is an important enabling step, ethanol itself is of little chemical interest; time resolved XAS studies of alcohols [15] (the only ultrafast XAS studies in a liquid to date) appear to show the slower, order 100 fs, settling of nuclear coordinates following multi-photon ionisation. However, ethanol opens up the opportunity to study a number of solutes. One such solute is aldrithiol, which excites at 267 nm and leads to bond cleaving of the sulphur–sulphur bond [16]. Similar bonds are important to the stability of proteins and enzymes in biological samples, and understanding these dynamics is therefore of interest.

Experimentally, aldrithiol makes a good choice for early investigation as the dynamics should be visible at the sulphur L-edge (∼163 eV), where a higher amount of flux is achievable than, for example, the carbon K-edge. Solubility tests found that a 0.15 M solution in ethanol is readily

made and that 0.2 M can be achieved with more intensive mixing and sonication. Figure 5.13 shows first measurements of the absorption of aldrithiol in our system at the sulphur L-edge. Absorption is shown in OD, which is defined as $\log_{10}(1/T)$ and has prefixes which follow the normal conventions for units, i.e. $1\,\text{mOD} = 1 \times 10^{-3}\,\text{OD}$. The lack of a strong absorption edge or pre-edge features suggests that the absorption lower than the sensitivity of the measurement. The change in absorbance that is seen can be explained by slower fluctuations in the harmonic source spectrum, and the stabilisation of the harmonic source remains one of the challenges to improved absorption measurements.

An estimate of the absorption strengths can be made from oscillator strengths calculated using standard quantum chemistry computation methods and by estimating the lifetime of the excited states. At the sulphur L-edge in aldrithiol, the strongest pre-edge feature is predicted to be the 2s $\rightarrow$ s-s $\sigma^*$ transition, with an oscillator strength of 0.06. Using an approximate 10 fs lifetime, the peak of the absorption (on resonance) is approximately $5.3 \times 10^{-19}\,\text{cm}^2$. For a 0.15 M concentration, the number density of aldrithiol is $9.03 \times 10^{19}\,\text{cm}^{-3}$. The absorption length is then $2.1 \times 10^2\,\mu\text{m}$ and a 2 µm interaction length would have an absorbance of 4 mOD. The absorbance scales linearly with the lifetime, but given that narrow features are also 'washed out' by the detector energy resolution, an absorbance resolution on the order of mOD is necessary, which explains the lack of structure to the first measurements.

In order to increase the absorbance, one can either increase the number density or the interaction length. Increasing the interaction length is technically challenging and will simultaneously increase the solvent absorption, whilst there are physical limits on the number density imposed by the solubility of the sample of interest. From this first measurement in aldrithiol, it is therefore clear that early experiments should be limited to solutions which can be made in high concentrations. Once our method is refined, it will be possible to reduce the minimum detectable change in OD and return to less concentrated solutions.

With this in mind, investigations were made into the absorption of solutes dissolved in water. Due to the relative lack of hydrocarbons, compared to alcohols, water is a highly polar molecule and as such is a very good solvent for polar solutes, the simplest of which are basic salts. NaCl

was chosen as a test as its high solubility, up to 6.2 M in water, and high chlorine content give the greatest opportunity to see strong absorption features.

The triple point of water is at a relatively high pressure (6.116 57 mbar, 273.1575 K), posing technical challenges for in vacuum operation caused by rapid freezing when evacuating the target chamber. This can be understood by considering a trajectory on a phase diagram for water, such as the red arrow on Figure 5.14. The liquid begins at atmospheric pressure and lab temperature. As the chamber is evacuated, the pressure quickly falls below the liquid-vapour interface at which point the liquid begins to boil. The flowing liquid is replenished so a complete transition to gas does not occur and the target remains stable; however, boiling is an endothermic process, so the liquid begins to rapidly cool. Below the triple point, this cooling leads to a vapour-to-solid phase transition. The transition to a solid crystal require nucleation, so ice crystals rapidly form on the nozzle and catcher and the resulting ice blocks the nozzle and stops liquid flow. A further reduction in pressure results in sublimation, but this sublimation is not enough to unblock the nozzle and only cools the ice further.

To solve this problem, several steps have been made. Firstly, to reduce the opportunity for nucleation on the catcher, optimum alignment is assured. This has been achieved via improved imaging of the nozzle-catcher system, using zoom lenses which allow for the accurate positioning of the nozzle and catcher assemblies. Secondly, both the nozzle and catcher mounts are heated via 25 W heating cartridges controlled by a PID feedback circuit which maintains a temperature of 60 °C. It is also imperative that liquid target is first created at atmospheric pressure and slowly evacuated whilst the target is flowing; this avoids instabilities which can lead to freezing.

An unfortunate consequence of the higher concentration of NaCl and the rapid evaporation of the jet is that the NaCl can ‘crash out’ of the solution. The NaCl is then able to contaminate optics in the X-ray path, and potentially the detector itself, leading to a strong absorption background.

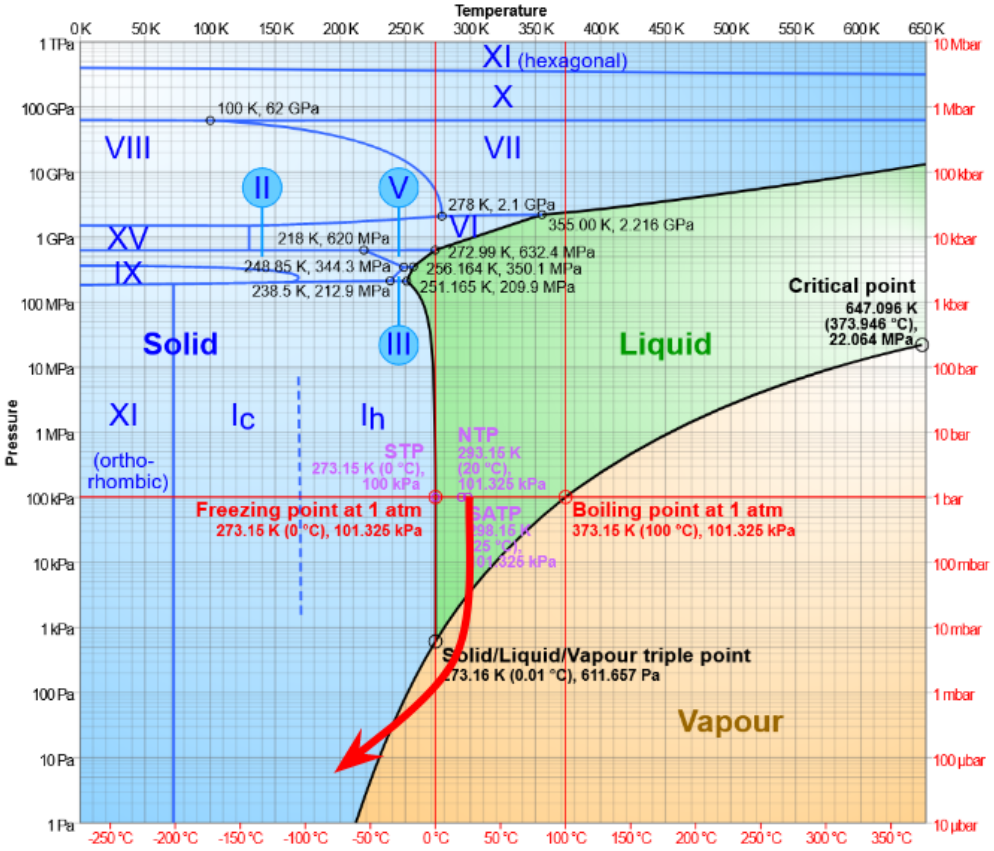



Figure 5.14: A phase diagram of water showing how its state of matter depends on temperature and pressure. Water does not exist in liquid form (in equilibrium) when below the triple point in either pressure or temperature. The red arrow indicates was happens to water as pressure is reduced and rapid boiling cools the water. Adapted from *https://en.wikipedia.org/wiki/Ice#/media/File:Phase_diagram_of_water.svg* under a creative commons license.

## 5.7 Future of liquid-phase XAS

Significant progress has been made towards transient XAS experiments in the liquid phase. A target delivery system has been successfully developed, which is capable of producing flat liquid sheets of order 1 µm thickness. Chapter 6 demonstrates the in-vacuum use of these targets for X-ray science. In terms of transient XAS, the next steps are to to transfer the methods for mOD resolution time-resolved measurements which have been developed for experiments in the gas and solid phase [17]. This includes the delivery of a pump beam to photo-excite the target of interest. In recent years, there have been significant advances on the development of femtosecond ultraviolet sources using dispersive wave emission in gas filled hollow-core waveguides [18]. This could prove to be the ideal source for studying photochemistry on the timescales of electronic coherences, or for quantum control experiments.

# References


[1] Jan Meibohm, Simon Schreck, and Philippe Wernet. Temperature dependent soft x-ray absorption spectroscopy of liquids. *Review of Scientific Instruments*, 85(10):103102, 2014. ISSN 10897623. doi: 10.1063/1.4896977. URL https://doi.org/10.1063/1.4896977.

[2] Douglas Garratt. *Time resolved X-ray absorption spectroscopy in Poly(3-hexylthiophene).* PhD thesis, Imperial College London, London, UK, October 2020.

[3] B. L. Henke, E. M. Gullikson, and J. C. Davis. X-ray interactions: Photoabsorption, scattering, transmission, and reflection at E = 50-30, 000 eV, Z = 1-92. *Atomic Data and Nuclear Data Tables*, 54(2):181–342, jul 1993. ISSN 0092640X. doi: 10.1006/adnd.1993.1013. URL http://linkinghub.elsevier.com/retrieve/pii/S0092640X83710132.

[4] G. Taylor. Formation of Thin Flat Sheets of Water. *Proceedings of the Royal Society A: Mathematical, Physical and Engineering Sciences*, 259(1296):1–17, nov 1960. ISSN 1364-5021. doi: 10.1098/rspa.1960.0207. URL http://rspa.royalsocietypublishing.org/cgi/doi/10.1098/rspa.1960.0207.

[5] Jonathan Charles Tobit Barnard. *X-ray generation from and spectroscopy of a thin liquid sheet.* PhD thesis, Imperial College London, London, UK, October 2021.

[6] Maria Ekimova, Wilson Quevedo, Manfred Faubel, Philippe Wernet, and Erik T. J. Nibbering. A liquid flatjet system for solution phase soft-x-ray spectroscopy. *Structural Dynamics*, 2(5):054301, sep 2015. ISSN 2329-7778. doi: 10.1063/1.4928715. URL http://aip.scitation.org/doi/10.1063/1.4928715http://aca.scitation.org/doi/10.1063/1.4928715.

[7] Gediminas Galinis, Jergus Strucka, Jonathan C.T. Barnard, Avi Braun, Roland A. Smith, and Jon P. Marangos. Micrometer-thickness liquid sheet jets flowing in vacuum. *Review of Scientific Instruments*, 88(8):083117, aug 2017. ISSN 10897623. doi: 10.1063/1.4990130. URL http://aip.scitation.org/doi/10.1063/1.4990130.

[8] N. Dombrowski, D. Hasson, and D. E. Ward. Some aspects of liquid flow through fan

spray nozzles. *Chemical Engineering Science*, 12(1):35–50, mar 1960. ISSN 00092509. doi: 10.1016/0009-2509(60)90004-X.

[9] Jake D. Koralek, Jongjin B. Kim, Petr Brůža, Chandra B. Curry, Zhijiang Chen, Hans A. Bechtel, Amy A. Cordones, Philipp Sperling, Sven Toleikis, Jan F. Kern, Stefan P. Moeller, Siegfried H. Glenzer, and Daniel P. DePonte. Generation and characterization of ultrathin free-flowing liquid sheets. *Nature Communications*, 9(1):1353, dec 2018. ISSN 20411723. doi: 10.1038/s41467-018-03696-w. URL http://www.nature.com/articles/s41467-018-03696-w.

[10] Jonathan C. T. Barnard, Jacob P. Lee, Oliver Alexander, Sebastian Jarosch, Douglas Garratt, Rose Picciuto, Katarzyna Kowalczyk, Clement Ferchaud, Andrew Gregory, Mary Matthews, and Jon P. Marangos. Delivery of stable ultrathin liquid sheets in vacuum for biochemical spectroscopy. *Frontiers in Molecular Biosciences*, 9, nov 2022. ISSN 2296889X. doi: 10.3389/fmolb.2022.1044610. URL /pmc/articles/PMC9701818//pmc/articles/PMC9701818/?report=abstracthttps://www.ncbi.nlm.nih.gov/pmc/articles/PMC9701818/.

[11] J. H. Hubbell. Photon Mass Attenuation and Mass Energy-Absorption Coefficients for H, C, N, O, Ar, and Seven Mixtures from 0.1 keV to 20 MeV. *Radiation Research*, 70(1):58, apr 1977. ISSN 00337587. doi: 10.2307/3574732. URL https://www.jstor.org/stable/3574732?origin=crossrefhttp://www.jstor.org/stable/3574732?origin=crossref.

[12] Toshiaki Kita, Tatsuo Harada, N. Nakano, and H. Kuroda. Mechanically ruled aberration-corrected concave gratings for a flat-field grazing-incidence spectrograph. *Applied Optics*, 22(4):512, feb 1983. ISSN 0003-6935. doi: 10.1364/AO.22.000512. URL https://www.osapublishing.org/abstract.cfm?URI=ao-22-4-512.

[13] Noboru Nakano, Hiroto Kuroda, Toshiaki Kita, and Tatsuo Harada. Development of a flat-field grazing-incidence XUV spectrometer and its application in picosecond XUV spectroscopy. *Applied Optics*, 23(14):2386, jul 1984. ISSN 0003-6935. doi: 10.1364/ao.23.

002386. URL https://www.osapublishing.org/abstract.cfm?URI=ao-23-14-2386.

[14] Tatsuo Harada, Kaoru Takahashi, Hideo Sakuma, and Andrzej Osyczka. Optimum design of a grazing-incidence flat-field spectrograph with a spherical varied-line-space grating. *Applied Optics*, 38(13):2743, may 1999. ISSN 0003-6935. doi: 10.1364/AO.38.002743. URL https://www.osapublishing.org/abstract.cfm?URI=ao-38-13-2743.

[15] Adam D. Smith, Tadas Balčiu Nas, Yi Ping Chang, Cédric Schmidt, Kristina Zinchenko, Fernanda B. Nunes, Emanuele Rossi, Vít Svoboda, Zhong Yin, Jean Pierre Wolf, and Hans Jakob Wörner. Femtosecond Soft-X-ray Absorption Spectroscopy of Liquids with a Water-Window High-Harmonic Source. *Journal of Physical Chemistry Letters*, 11(6): 1981–1988, mar 2020. ISSN 19487185. doi: 10.1021/acs.jpclett.9b03559.

[16] Kirsten Schnorr, Aditi Bhattacherjee, Katherine J. Oosterbaan, Mickaël G. Delcey, Zheyue Yang, Tian Xue, Andrew R. Attar, Adam S. Chatterley, Martin Head-Gordon, Stephen R. Leone, and Oliver Gessner. Tracing the 267 nm-Induced Radical Formation in Dimethyl Disulfide Using Time-Resolved X-ray Absorption Spectroscopy. *Journal of Physical Chemistry Letters*, 10(6):1382–1387, mar 2019. ISSN 19487185. doi: 10.1021/acs.jpclett.9b00159. URL https://pubs.acs.org/sharingguidelines.

[17] D. Garratt, L. Misiekis, D. Wood, E. W. Larsen, M. Matthews, O. Alexander, P. Ye, S. Jarosch, C. Ferchaud, C. Strüber, A. S. Johnson, A. A. Bakulin, T. J. Penfold, and J. P. Marangos. Direct observation of ultrafast exciton localization in an organic semiconductor with soft X-ray transient absorption spectroscopy. *Nature Communications*, 13(1):1–8, dec 2022. doi: 10.1038/s41467-022-31008-w.

[18] Christian Brahms, Dane R. Austin, Francesco Tani, Allan S. Johnson, Douglas Garratt, John C. Travers, John W. G. Tisch, Philip St.J. Russell, and Jon P. Marangos. Direct characterization of tuneable few-femtosecond dispersive-wave pulses in the deep UV. *Optics Letters*, 44(4):731, feb 2019. ISSN 0146-9592. doi: 10.1364/ol.44.000731. URL https://pubmed.ncbi.nlm.nih.gov/30767973/.

# Chapter 6

# High harmonic generation in liquid isopropanol

Section 3.1 introduced high harmonic generation within a recombination model and identified characteristics which have been derived from the corresponding theory. To recap, some of these characteristics are:

- A plateau of harmonics, which extend into the XUV or soft x-ray regime;
- Either an attosecond pulse train or isolated attosecond pulses, depending on duration and frequency of the driving field;
- Odd harmonics spaced in energy by twice the driving field photon energy, in the case of a pulse train; and a continuum, in the case of isolated pulses;
- A maximum harmonic energy, $E_{\text{cutoff}}$, which increases quadratically with the driving field wavelength and linearly with the intensity;
- Gaussian dependence on the ellipticity of the driving field;
- Harmonic yield which scales quadratically with the number of coherent emitters.

Regarding the final point, the natural question arises as to whether efficient high harmonic generation can occur in dense media, where even over a short coherence length, the number of

emitters is large compared to a gas.

Liquids offer some of the advantages of each of solids and gases. They are self-healing, reusable, and reproducible; they are a dense medium and, compared to a high pressure gas, can be well localised within a vacuum chamber, creating lower ambient pressure for re-absorption. These features may make them competitive VUV sources for science and industry, for example, in lithography or high precision metrology [1]. The potential energy surface an electron witnesses in a liquid bears similarities to a gas in that electrons are bound to molecular orbitals; however, unlike a gas, there is bonding in molecules from electronic wavefunctions spread over multiple molecules. Furthermore, the excursion lengths of electrons are larger than typical inter-molecular distances or mean free paths.

It is therefore of great curiosity to know the extent to which HHG in a liquid can be understood within the framework of re-collision based HHG. Does local order, which can create a quasi-band structure, mean that a better description is found in k-space; and where the underlying physics deviates, what are the ramifications for the characteristics of the emission? HHG spectroscopy has been used in molecules as a time resolved probe of charge dynamics on the timescale of 1 - 2 fs, which is possible due to the mapping of the electron trajectories onto the harmonic energy and the dipole strength at that energy depending on the molecular wavefunction. In liquids there may be the exciting opportunity to extend this method to the study of molecules in the liquid phase and also to use HHG spectroscopy to probe the liquid environment.

As with gas-phase HHG at its inception, the theory and computational methods and resources required to model liquid-phase HHG have not yet been developed; so, like its predecessor, an understanding of liquid-phase HHG currently relies on empirical methods. Flettner et al. [2] first reported harmonics above the ionisation potential of water, in microdroplets; however, these droplets were first exposed to an intense pre-pulse, ∼50 ns before the driving field. This vapourised the droplets and the HHG occurred at an intermediate density, between that of liquid- and vapour-phase water. They reported coherent harmonic emission as high as 42 eV, the 27th harmonic of an 800 nm driving field. Kurz et al. continued in a similar manner, exciting 15 µm diameter water droplets with a pre-pulse and probing with an 800 nm laser [3]. They

varied the delay over a ∼20 ns range to explore the effect of the density on the phase-matching of the resulting harmonics. They identified phase-matching phenomena similar to gas-phase HHG and noted a saturation of the harmonic yield with the intensity of their driving field, which was attributed to a rising density in free electrons. They followed this experiment with an investigation into the the frustration of the harmonic cutoff due to collisional effects in the medium [4]. They identified a damping of the harmonic yields at high densities, in particular for long trajectories.

Heissler et al. measured harmonics up to 19 eV in reflection from plasma formed at a liquid-vacuum interface, from a cylindrical microjet, drawing comparisons to similar experiments in plasma reflection at solid-vacuum interfaces. DiChiara et al. investigated harmonics in water and heavy water, through 5 – 100 µm liquid sheets with a mid IR laser in the optical range [5]. They generated perturbative harmonics up to the 13th order (∼4 eV) but no harmonic emission above the ionisation potential, though this is unsurprising as the experiment was not conducted at low vacuum. Luu et al. reported harmonic emission up to 20 eV, utilising sub-micrometer water sheets generated with colliding microjets [6]. Despite extending beyond the ionisation potentials of the liquids studied, the characteristic plateau harmonics of recombination based HHG were not observed. In contrast to all previous studies, they attributed their observations to a HHG mechanism similar to the band-structure models of solids and attributed the frustrated cutoff to a lack of long range order in liquids.

A better understanding of the mechanism of high harmonic generation in liquids can be reached by controlling the parameters of the driving field and relating the characteristics of the emission to the energy landscape as witnessed by the electrons. All of the experiments referenced above were conducted using pulses longer than 30 fs, i.e. in a regime in which the pulse envelope is significantly longer than the laser cycle period.

All harmonic spectra presented to-date are therefore resulting from many half-cycles and unravelling the processes happening in a single half-cycle is challenging. A few cycle laser field is employed here; not only does this provide a better probe of the physical mechanism, a few cycle laser field will also have a dramatically reduced plasma build-up before the peak field

from propagation through the target. It will be shown here that, using such a few-cycle field, higher energy XUV emission from liquids does occur, up to 50 eV. Critically, evidence is found that in the strong field regime electron scattering plays a role in modifying the spectrum whilst the emission no longer exhibits characteristics of a band structure system. Contrary to earlier indications, this behaviour shows that HHG in liquids is not limited to the low energy VUV range and HHG in liquids can offer physical insight into the behaviour of real space electron trajectories and of the intermolecular energy landscape [7, 8].

## 6.1 Setup for measuring liquid high harmonic generation

To show this, 1–2 micron thick liquid targets were illuminated with an actively CEP stabilised 13 fs (FWHM) 1.75 µm (corresponding to 2.2 cycles within the FWHM) laser with pulse energy of up to 500 µJ.

Control of the driving field was achieved using basic optical components. The pulse energy was modified either using a broadband half-waveplate and polariser pair or by adjusting an aperture placed before the focussing optic. Whilst other parameters were fixed, this allowed for the peak intensity at the interaction region to be controlled. These two methods of controlling the pulse energy have their own advantages. The half-waveplate and polariser add dispersion to the pulse, lengthening it to approximately 18 fs, but have negligible affect on the spatial profile of the focus at the interaction point, and can be scanned more easily and in smaller steps. An iris increases the focal spot size when closed, therefore having a nonlinear control of the peak intensity and requiring greater care to avoid a large error in establishing the relative change, but does not introduce dispersion.

Control of the ellipticity was achieved using a broadband achromatic quarter-waveplate (Bolder Vision). This has the additional effect of rotating the polarisation axis. This change could be corrected with a half-waveplate, at the expense of lengthening the pulse duration. Measurements were made whilst rotating the polarisation axis to verify the effect on the harmonic emission, and there was no registered effect. From this it is understood that the target molecules were randomly oriented and the waveplate was therefore omitted, to introduce as little dispersion as

possible to the few-cycle pulse.

Finally, the CEP of the pulse was controlled by scanning the transmission through a pair of fused silica wedges, in which there is a mismatch between the group and phase velocity. To achieve this control, the CEP was actively stabilised using a 2f-3f interferometer, in which spectral intereference between the second and third harmonics of a parasitic beam (reflection from the first incident fused silica wedge) was measured. The phase of spectral fringes was then input to a fast feedback loop controlling a piezo-actuator which modifies the delay between the pump and seed of the optical parametric amplifier used to generate the SWIR beam (see Appendix A). The liquid targets were generated via the methods described in Section 5.

The harmonic emission was measured using a flatfield spectrometer consisting of a grazing incidence variable-line-spacing grating, a microchannel plate (MCP) mounted on on a vertical translation stage, and a CCD camera (pixelfly, PCO) to image the MCP (APD059M-01, Photonis). The 40 mm MCP diameter allowed for the imaging of harmonic orders spanning an approximately 30 nm window and with vertical translation of the MCP, this window could be centred at different energy ranges. The liquid target could be translated along X, Y, and Z axes independently via a manipulator on the vacuum feedthrough for the target delivery system and to adjust the collector accordingly. It could also be rotated in the horizontal plane via a rotation flange. Ambient pressure below $1 \times 10^{-4}$ mbar in the target chamber and below $1 \times 10^{-6}$ mbar in the spectrometer chamber was maintained through a combination of: turbomolecular pumps backed with scroll and screw pumps; a liquid nitrogen cold trap surrounding the jet with through-holes for laser transmission, pumping, and visibility; and differential pumping between the two chambers. Figure 6.1 shows a diagram of the setup used.

## 6.2 Origin of harmonic emission

As shown in Figure 6.1c, harmonic emission extending 10s of eV beyond the ionisation potential of isopropanol, indicating that high harmonic generation is possible. However, before analysing closely the properties of the emission, as there is both liquid isopropanol and isopropanol vapour which has evaporated from the liquid surface within the Rayleigh range of the focus, the source

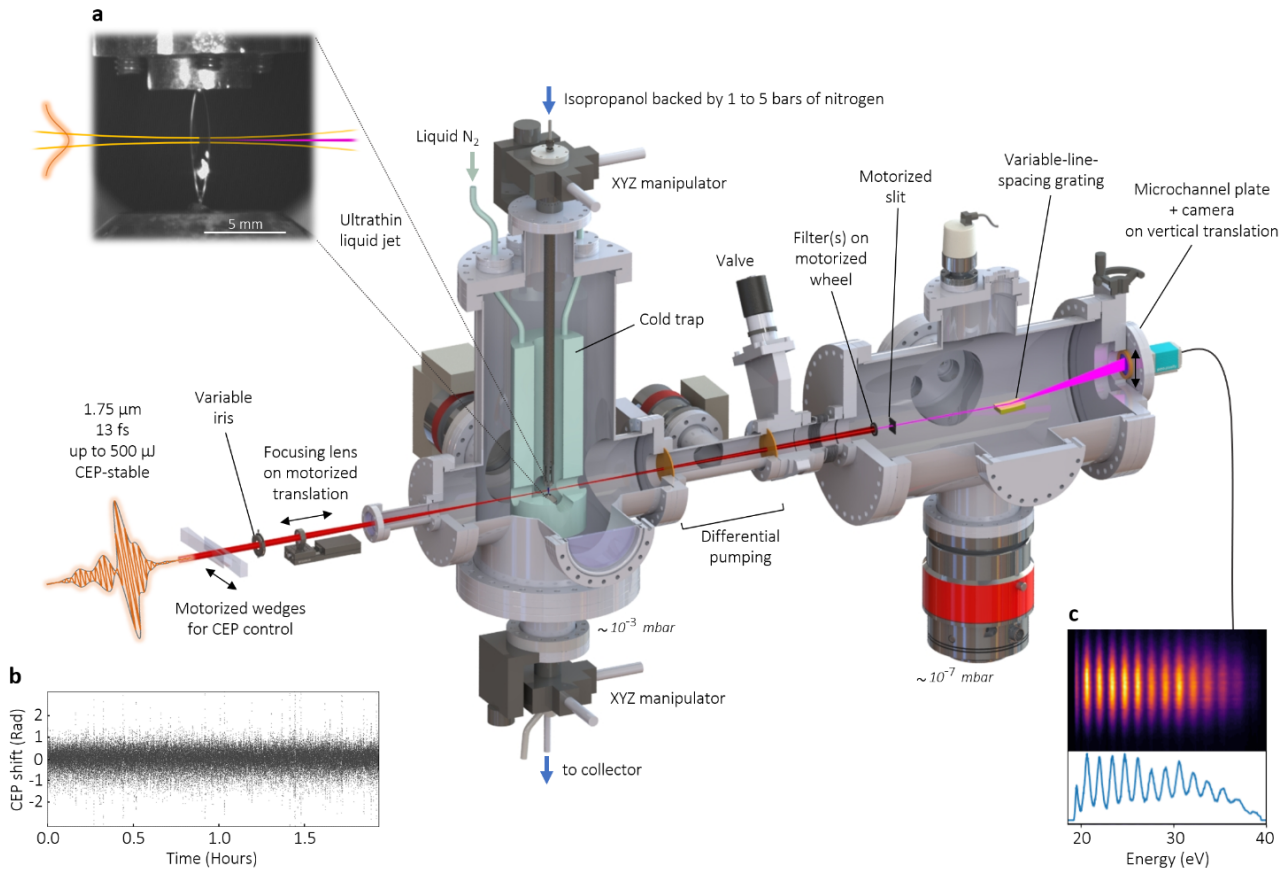



Figure 6.1: Schematic diagram of the experimental setup used to produce and measure high harmonic generation from liquid isopropanol. Figures inset show (a) an in situ image of an isopropanol liquid sheet, (b) measurement of the CEP stability over a two hour duration, and (c) an example of high harmonics recorded with the setup. Image courtesy of Clement Ferchaud.

of the emission must be established. To do so, a series of measurements were made which each isolate harmonic emission from either the liquid or vapour. Figure 6.2 shows the longitudinal (in the direction of the jet flow) and lateral (across the liquid sheet) pressure dependence of the HHG emission.

Figure 6.2a shows a horizontal scan relative to the laser focus, which was performed across the upper region of the jet where the vapour pressure at the surface of the jet was 28 mbar. This was done with a driving field with peak intensity of 80 TW cm$^{-2}$, such that a plasma plume was clearly visible when the jet is placed in the interaction region. The harmonic spectra show a distinct top-hat emission pattern corresponding to the width of the jet, with no emission detected when passing only through the vapour. To confirm this, the liquid target was rotated about the vertical axis to allow the laser pulses to pass directly parallel to either side of the jet;

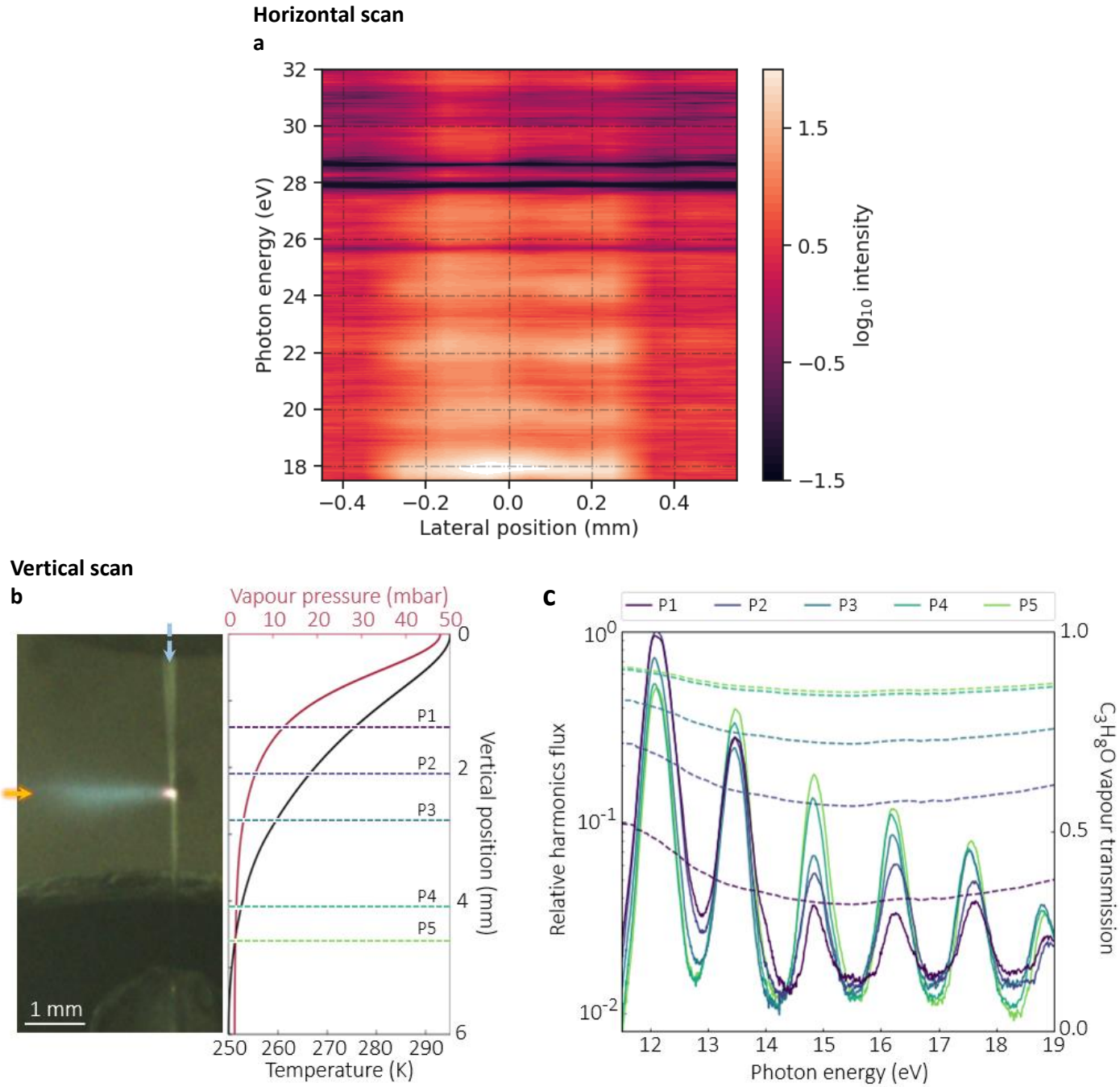



Figure 6.2: The dependence of the HHG on the position of the jet relative to the laser focus. (a) For a scan of the jet laterally, harmonic emission is seen only when the laser focus is incident on the liquid jet. The positions shown are relative to the centre of the jet. This scan was of the upper portion of the jet, where the vapour pressure at the jet surface is approximately 27 mbar and the jet is 600 µm wide. (b) At different longitudinal positions on the jet, vapour pressure changes significantly due to evaporative cooling. Five positions are highlighted, P1 – P5, with descending pressure and temperature. (c) HHG spectra at the five positions labelled in (b).

in this setting, no measurable VUV emission was observed.

By scanning the laser beam vertically down the jet, at the five positions shown in Figure 6.2b, the harmonics are measured as a function of the vapour pressure at the surface of the sheet. In the low density regime, any harmonic emission from the gas phase would increase with increasing vapour pressure. However, in descending the jet, the harmonic emission yield is increased by the declining isopropanol vapour density, as shown in Figure 6.2c. Instead of resulting in more HHG emission, absorption in the vapour at the different positions modifies the shape of the harmonic spectra. The greatest change is seen where isopropanol's transmission is lowest and the pressure is higher, resulting in a relative decrease in the flux. For example, the harmonic at 15 eV is least intense at P1, which corresponds to the lowest vapour transmission. As well as evidencing harmonic emission from the liquid, this also highlights the importance of absorption in the propagation of the harmonic emission. Any VUV light generated at the front surface of the liquid target will be unable to propagate, so any harmonic emission observed must be generated close to the rear surface. A consequence of this is that the ideal liquid target must be thin, transparent, and have low dispersion at the frequency of the driving field.

To understand the lack of harmonics originating from the vapour phase, a calculation of the number density of vapour molecules in the proximity of the focus was made. This is aided by mathematical similarities between the vapour flow and electrostatics: the density near a liquid surface is analogous to electric field near a charge or charged surface, as the flux of molecules is formally equivalent to Gauss's law. The pressure near a point source therefore follows in inverse square law. Calculations of the pressure surrounding a vapour source in vacuum exist in the literature, for at least two cases:

- For a cyclindrical jet by Faubel et al. [9] and equivalently for ice by Sadtchenko et al. [10].
- For a thin disk by Brastad and Nathanson [11].

Faubel et al.'s treatment is more complete, accounting for the different flow regimes close to the jet. Here, the simpler approach of the other works is used, modelling the target as a rectangular surface with a constant surface pressure. The vapour pressure is then adjusting according to

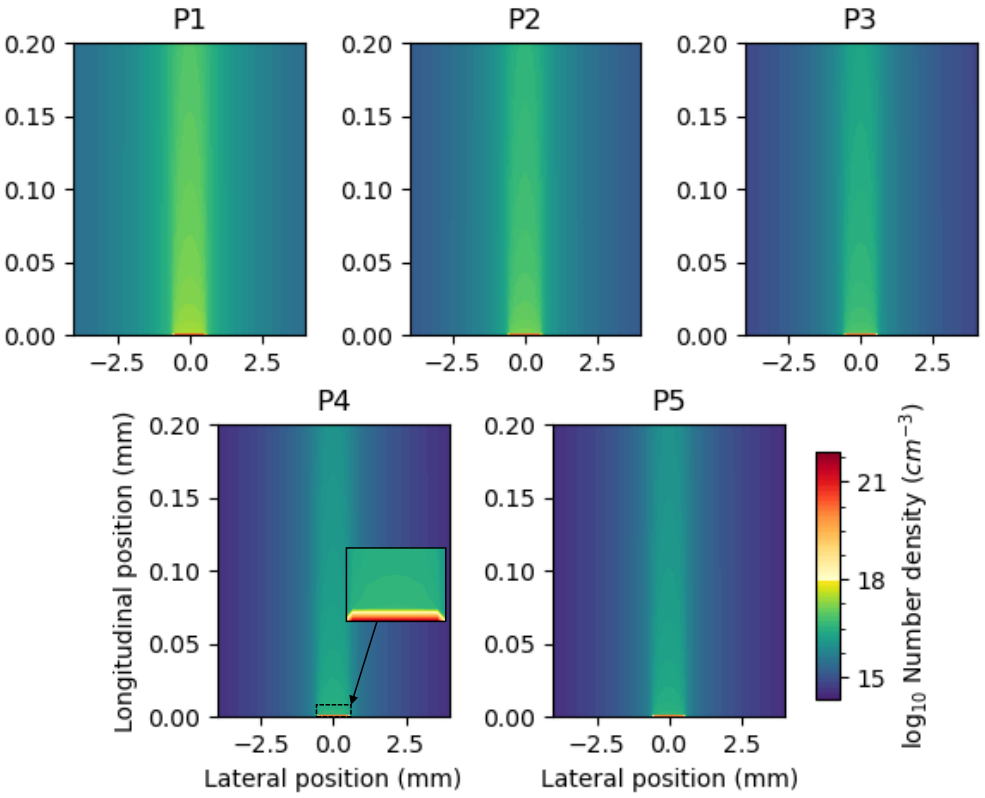



Figure 6.3: Slices in the horizontal plane of the calculated vapour pressure surrounding a rectangular isopropanol jet of 1 mm width, 1 cm length, and 5 different vapour pressures (P1–P5) corresponding to the longitudinal positions in Figure 6.2. Inset on the slice for P4 is an expanded view of the pressure 0-10 µm from the jet axis.

the position on the jet. The calculation converges with the two limiting cases: $1/r$ dependence for a thin and infinitely long source; and $1/r^2$ for a point-like source.

The result of these calculations is shown in Figure 6.3, and shows a drop off in the number density of isopropanol molecules of orders of magnitude over micrometer-scale distances. When the laser is along the axis of highest gas pressure, the areal number density of emitters is approximately 3 orders of magnitude fewer in the gas than in the liquid. Furthermore, the areal number density of gas-phase emitters is approximately equivalent to 0.2 mbar of an ideal gas with an interaction length of 1mm. This low areal density explains why any harmonic emission from this volume was below the sensitivity of the spectrometer.

The liquid jet enters into a vacuum at a temperature of 20 °C. The temperature of the jet at each position is calculated by considering the rate of evaporation, and a subsequent cooling due to the heat extraction for the phase change [12]. The number of molecules which evaporate

Table 6.1: Temperature measurements of a liquid isopropanol jet in vacuum, made using a thermocouple.

| **Distance from nozzle (mm)** | **Temperature ( °C)** |
|---|---|
| 1 | 10.6 |
| 3.5 | -5.5 |
| 5 | -9.5 |
| 7 | -19.5 |
| 10 | -20.0 |

from a surface $A$ during a time interval $\delta t$ is given by: [13]

$$\frac{\delta N}{\delta t} = \frac{1}{\sqrt{2\pi m k_b T}} \times (p_{vap} - p)A, \tag{6.1}$$

where $m$ is the mass of one molecule, $p_{vap}$ denotes the temperature dependent vapour pressure, $p$ is the pressure of the gas phase surrounding the jet, and $T$ is the temperature of the liquid. The phase transition requires a negative evaporation enthalpy $H_{vap}$ to be added to the liquid, leading to the temperature change,

$$\delta T = \frac{H_{vap}}{N_A C M}\delta N, \tag{6.2}$$

where $N_A$ denotes the Avogadro constant, $C$ the specific heat and $M$ the mass of the remaining liquid in the volume under consideration. Thus the cooling rate of the liquid jet can be estimated. The evaporation enthalpy $H_{vap}$ is assumed to be constant over the temperature range of interest. This calculation was checked against measured data (see Table 6.1 and previous measurements [14]), and good agreement was found.

## 6.3 Dependence on the driving field

HHG emission was recorded in liquid isopropanol beyond 45 eV. The spectrum of the emission depends on the length of pulse used for the driving field and the carrier envelope phase (CEP). As discussed in Section 3.1, CEP is of greater importance when the pulse envelope is comparable in width to the laser period. Figure 6.4 shows harmonic spectra taken with 11 fs, 55 TW cm$^{-2}$ pulses, for both CEP-averaged and fixed-CEP pulses.

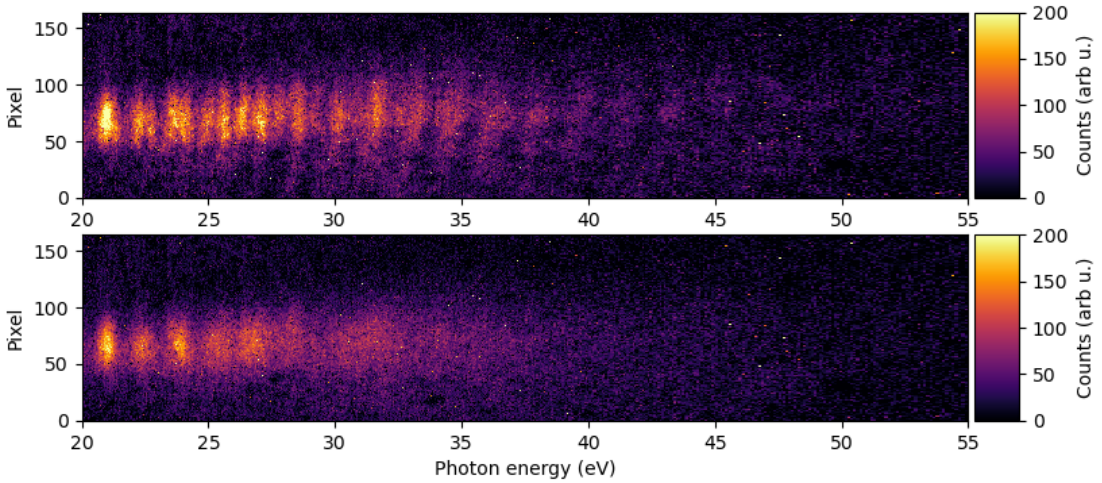



Figure 6.4: MCP images of the flatfield spectrum of VUV emission from HHG in liquid isopropanol for (a) averaged shots of fixed CEP and (b) averaged shots of CEP averaged over a $2\pi$ interval. The vertical axes show the spatial profile of the harmonics in the horizontal plane and the horizontal axes show the photon energy. The data as presented here is with minimal processing (only background subtraction); basic image processing such as thresholding and removal of hot pixels can be applied before summing over the spatial axis.

In the CEP-averaged harmonics, fringes are visible up to 30 eV and a continuum extends further, to approximately 45 eV. The single-CEP HHG shows additional fringes the lower photon energies, and harmonic fringes extending to 45 eV. The extension of the cutoff energy, compared to previous works [6], can be attributed to the use of a few cycle pulse below the threshold.

The HHG emission was measured whilst the CEP of the driving field was varied over more than $2\pi$ radians whilst looking at the highest achievable photon energies, with a peak intensity between 50 and 55 TW cm$^{-2}$. By integrating over the spatial axis of the MCP images, the dependence of the HHG spectrum on the CEP is revealed, as shown in Figure 6.5. The absolute value of the CEP is not measured independently of the CEP scan, so the values in Figure 6.5 are for a CEP shift from an arbitrarily set zero and referred to as either CEP shift or relative CEP. Note that because a 2f-3f interferometer was needed for these measurements, particular care was taken to optimise the pulse length and spectral broadening in the hollow core fibre compression. Therefore, the pulses in the driving field were the shortest for these measurements, 11 fs.

There is $\pi$-periodicity in the CEP dependence, which matches the periodicity of the magnitude of the electric field. A lack of change with the direction of the electric field indicates that, as

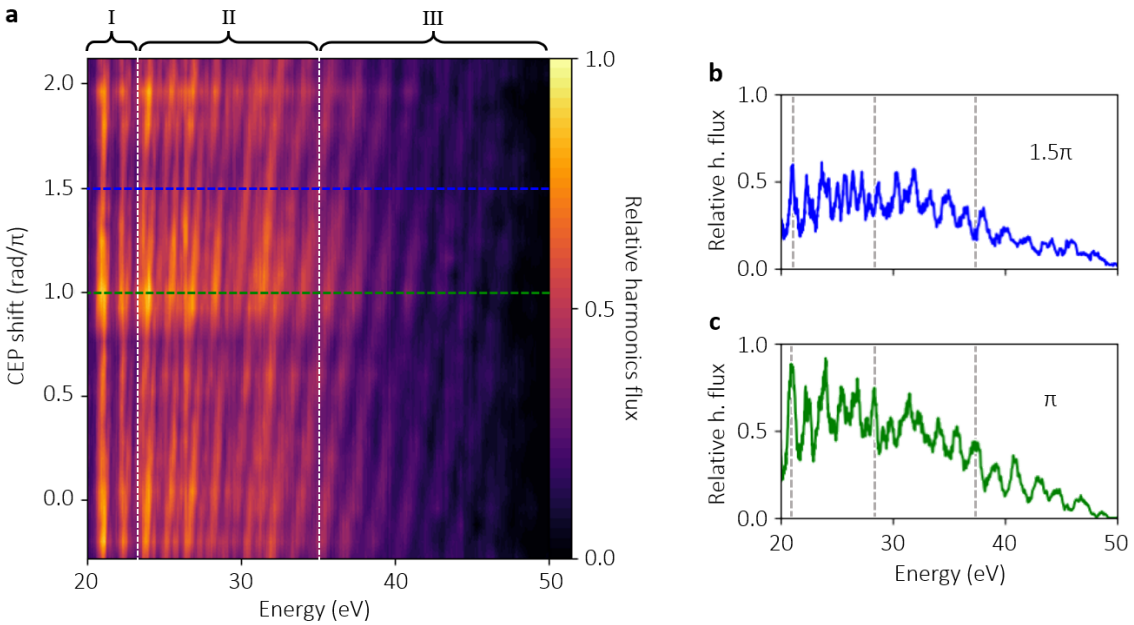



Figure 6.5: (a) Carrier envelope phase (CEP) dependence of high harmonic emission from liquid isopropanol, integrated over the spatial axis. Three spectral regions of interest are demarcated which show different behaviour dues to the different number of contributing cycles (see main text). (b) and (c) show the spectral emission at the two CEP points corresponding to the colour-coded dashed horizontal lines on (a). Dashed lines of constant energy on (b) and (c) show harmonic peaks and troughs for comparison between the emission at these two values.

expected, there are no symmetry breaking effects which have a preferential direction for the electric field. Furthermore, looking across the energy range of the spectrum, there is variation in how the harmonics change with respect to the CEP. This can be understood in a recollision based model by considering the temporal structure of the CEP and the driving laser.

Consider a pulse with a Gaussian envelope of 11 fs FWHM and carrier wavelength 1800 nm. When the CEP is zero, such that a maximum of the electric field's carrier wave and the maximum of its envelope coincide, the ratio between the second-largest and largest magnitude half-cycles is 0.44. With a peak intensity of 45 TW cm$^{-2}$ this corresponds to a reduction in highest photons emitted from that half-cycle by 24.0 eV. This exemplifies how as the photon energy moves from low to high, the number of half-cycles contributing to the harmonic emission decreases. As the fringes in the harmonics result from interference between the different pathways to emission a particular energy photon, a reduction in the number of contributing half-cycles closes some of these pathways to emission. Similarly, a change in the CEP will change the emission time within each half-cycle which contributes to a particular harmonic.

In the highest energy region of Figure 6.5, the harmonics are clearly distinguishable and following a single harmonic through a $\pi$ shift in the CEP, there is a shift to the next peak. Consider when the CEP is $\pi/2$, such that the two greatest half-cycles are of equal magnitude but opposite sign, and that they are the only two half-cycles contributing to a given energy emission (i.e. above the next half-cycle cutoff) The harmonic emission of angular frequency $\omega$ from the two half-cycles coherently sums as

$$E(\omega, t) = E_0(\omega)e^{-i\omega t} - E_0(\omega)e^{-i\omega(t+\frac{T}{2})} = E_0(\omega)e^{-i\omega t}\left(1 - e^{-i\frac{\omega T}{2}}\right) \tag{6.3}$$

Constructive interference is achieved for $\omega = 2\pi(2m+1)/T$, where $m$ is any integer and destructive interference is similarly achieved for $\omega = 4\pi m/T$. Therefore, only odd harmonics are seen at this CEP value. In [15], the CEP dependence of Argon gas is observed in this same energetic region and similar behaviour is observed. There, a simple model for the interference pattern from the interference of two successive half-cycles is derived, in a similar spirit to Eqn. 6.3. Evaluating a second order Taylor expansion of the envelope and considering a linear change in the photon emission time due from the intrinsic intensity chirp of the harmonics, a linear increase with CEP of the peak of the harmonic fringes is found. At lower photon energy, where more half-cycles contribute to the harmonic emission the interference pattern is more complicated due to the uneven spacing in the harmonic emission times and the increasing difference in ionisation rates.

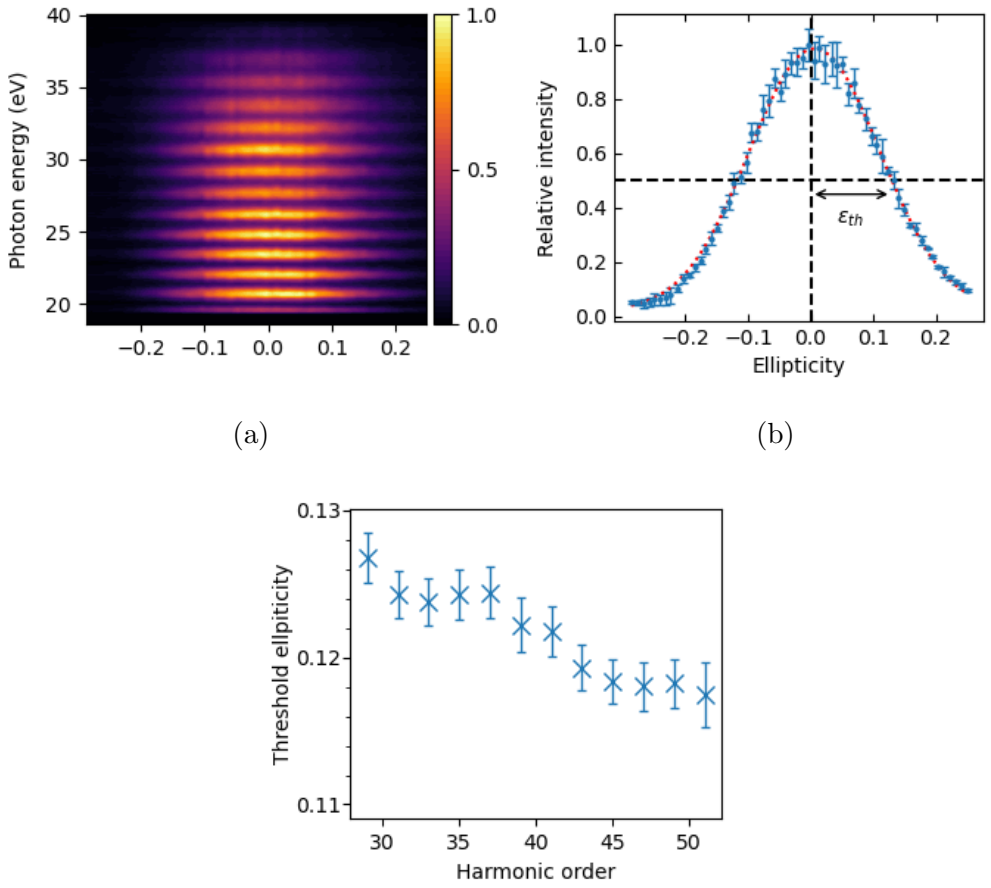
Figures 6.5b and 6.5c show the harmonic spectra for a relative CEP of 1.5 $\pi$rad and $\pi$rad (as annotated on Figure 6.5a) respectively. At the highest energies in Figure 6.5c, fringes are visible which could correspond to the case of two contributing half-cycles. Note that although Eqn. (6.3) suggests 100% fringe visibility, it does not account for the difference in amplitude or spatial averaging. For a relative CEP of $1.5\pi$ rad, however, fringes are absent above 39 eV and compared to at $\pi$ rad, the peak intensities are reduced. This is consistent with harmonic emission which, in the case of a $1.5\pi$ rad shift, is resulting from a single half-cycle, i.e. the relative CEP of of $1.5\pi$ rad is consistent with an absolute CEP of 0 rad.

Whilst the CEP dependence shows supporting evidence of recollision based HHG process, there

are however two points unaddressed: Firstly, despite a significant change in the peak electric field with a change in CEP, there is only a small extension to the harmonic cutoff. Furthermore, when the CEP is such that only one half-cycle contributes to the highest energy i.e. at a relative CEP of $1.5\pi$ rad, the region over which only one half cycle contributes is only $\sim$15 eV, not the 20 eV region of single cycle harmonics predicted.

To further investigate the mechanism of emission, the ellipticity of the driving field was varied in 61 steps from approximately $-0.25$ to 0.25 whilst measuring harmonics from the 31st to the 55th order. Note that in these measurements, the CEP is not actively stabilised and therefore each spectrum is CEP-averaged. The result is shown in Figure 6.6. The harmonic yield has a Gaussian dependence on the ellipticity of the driving field. To quantify this Gaussian dependence, a fit is made to the ellipticity of each harmonic, from which the half-width at half maximum is extracted. This can be referred to as the 'threshold ellipticity', or $\epsilon_{\mathrm{th}}$. It is found that the threshold ellipticity decreases with increasing harmonic order. This observation is consistent with a re-collision based mechanism for HHG and in agreement with previous measurements in gases [16]. The ellipticity of the field has two effects. Firstly, there is a reduction in the maximum electric field strength. Secondly, and more significantly, acceleration of a charge in a circularly polarised field can be decomposed into acceleration in two perpendicular axes, out of phase. As such, a classical trajectory does not return to its original point of ionisation, and therefore does not recombine with its parent nucleus. The lower threshold ellipticity at higher harmonic orders is consistent with the observation of the short trajectories, for which the length of electron excursions increases with the harmonic order. They are therefore displaced further from their parent nucleus by an elliptical driving field, reducing the ellipticity threshold.

Scans of the driving field intensity were also taken, using a half-waveplate and polariser, and are shown in Figure 6.7. Note that for these measurements the longer pulse length of $\sim$18 fs reduces the maximum obtainable peak intensity; furthermore, there is an increased ionisation fraction during the early stages of the pulse, making a like-for-like comparison to the shorter pulse length difficult. Nonetheless, a steep increase in the cutoff energy can be seen as the peak intensity increase, until approximately 25 eV. The harmonics then saturate, which can be attributed to a




(a) (b)

(c)

Figure 6.6: Ellipticity dependence of high harmonic generation in liquid isopropanol. (a) Harmonic emission spectra summed over the spatial axis with changing ellipticity. (b) The total harmonic emission within the range of the detector (approx. between 20 and 40 eV). 60 points are spaced evenly in $\tan(\theta_{\mathrm{QWP}})$ ($\theta_{\mathrm{QWP}}$ is the angle of the quarter waveplate rotation from linear), which corresponds to spacing of approximately 0.009 in ellipticity. 4 repeats were made at each point and the standard error of their mean is shown in the error bars.

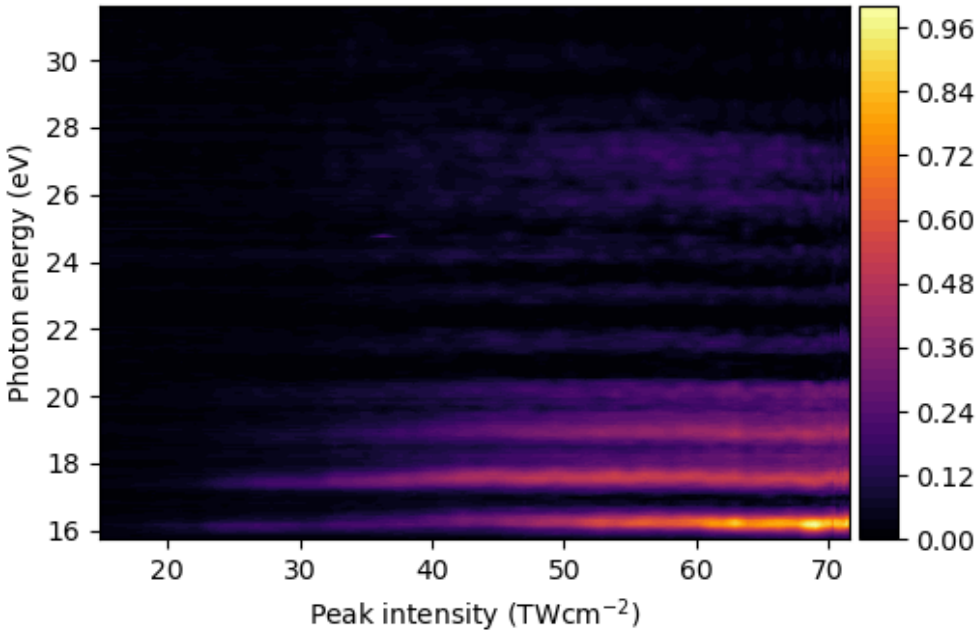



Figure 6.7: Peak intensity dependence of high harmonic emission in isopropanol, for an 18 fs pulse.

build up in the ionisation fraction before the peak of the field is reached temporally.

Similar scans using an iris to control the peak intensity whilst preserving a shorter, 13 fs pulse duration are shown in Figure 6.8. Here however, the spatial divergence of the harmonics along the horizontal axis is shown by stacking images of the MCP for each iris position. The harmonic cutoff can be seen to rise with increasing intensity until 45 TW cm$^{-2}$ to a maximum of approximately ∼45 eV. After this point the increasing density of plasma clamps the strength of the harmonics, they become unstable, and there is no further increase in the cutoff energy. There is also an increase in the background of the MCP images due to incoherent light and an increase in dark counts from a higher background pressure, which is not to be confused with harmonic emission. Coherent emission can be separated from the background due to its spatial properties, i.e. its Gaussian divergence in the spatial axis. The incoherent light is possibly from harmonic emission dispersed from the dense plasma. The increase in background pressure is due to to a plasma plume which is emitted from the surface of the jet which the laser is incident upon, when working above 53 TW cm$^{-2}$. This imparts momentum on the jet, destabilising it, and results in some spray of isopropanol from the jet itself and from the catcher. Figure 6.9

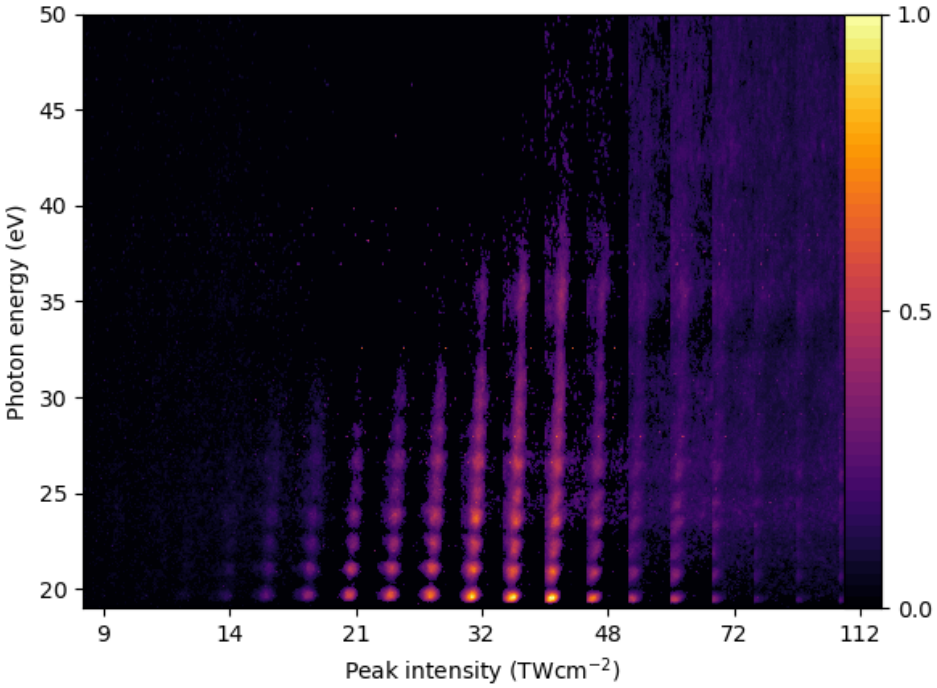



Figure 6.8: Stacked images of high harmonic generation in isopropanol, for focal spot intensity varied using an iris aperture. The iris both reduces the transmission and increases the focal spot size when the aperture is reduced. Each stacked image shows the spatial axis of the harmonics in y and the spectral axis in x. Intensities plotted on the x axis reflect the peak intensity of the images but note that the peak intensity is the constant accross the pixels of each image.

shows the the spatial distribution of the spectrum for a single intensity, which shows more clearly the spatial distribution of the emission. The harmonics are confined between approximately pixels 50 and 150 of the CCD (along the axis of the spatial divergence), whilst the incoherent emission is mostly below pixel 100.

## 6.4 Mechanism of HHG in the liquid phase

The evidence of these measurements indicates a recollision based mechanism for HHG in liquid in the regime of an intense, few-cycle driving field. However, the features highlighted in particular for the case of the CEP dependence indicate some discrepancies between the underlying physics for a liquid and for a gas. This can be understood by considering at the key differences between a liquid and a gas in terms of the HHG process.

A key length-scale of the interaction is the length of electron excursions. These are found classically to be of the order $|eE_0|/m_e\omega^2$. Therefore, for a 45 TW cm$^{-2}$ driving laser at 1.8 µm,

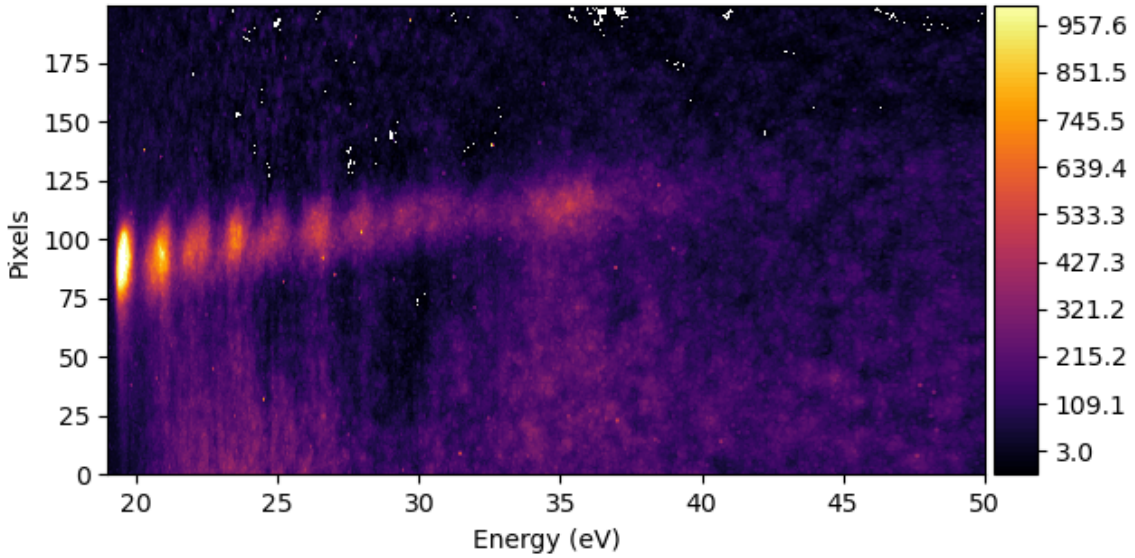



Figure 6.9: Flatfield spectrometer images from HHG emission from liquid isopropanol, for 13 fs pulses at 48 TW cm$^{-2}$, which is close to the threshold for formation of an plasma plume.

electron excursions of the order of 3 nm can be expected. Appropriate length-scales for liquids and gases are the average spacing between atoms or molecules (referred to as average inter-molecular spacing, for brevity) and the mean free path.

The mean free path is the mean distance a molecular entity in a fluid traverses before colliding with another molecular entity. As such, it is related to the the size of the molecular entities as viewed by themselves. For this reason, the relation to electron excursions is complicated; the 'size' of the molecular entity, as viewed by the electron, is not the same as the 'size' according to similar molecular entities. It is the scattering cross section, which depends on the kinetic energy of the electron and is not trivially measured. Also note that in the usual definition of the mean free path, it is also assumed that all molecules belong to the same velocity distribution, which has the effect of increasing the result by a factor of $\sqrt{2}$. This is not so in the case of the electron excursions, for which the molecular entities are approximately fixed.

The average inter-molecular spacing, however, depends only on number density and is typically much smaller than the mean free path; for example, air at standard temperature and pressure has a mean free path of 68 nm and an average inter-molecular distance of 3.3 nm. For a gas to have a mean free path below 3 nm it must have a pressure in excess of approximately 1 bar. However, this is easily achieved for a liquid; the average inter-molecular spacing of isopropanol

at standard temperature and pressure is $5.0 \times 10^{-1}$ nm. Therefore, liquid targets are physically distinct from gases in that the length scales of liquid targets are smaller than the length scales of recollision based high harmonic generation.

To account for this in a theory of high harmonic generation in liquids, one must consider the interaction of electrons with molecular entities aside from the one that they are ionised from, which is typically overlooked for gases. The interaction of electrons with molecular entities is a subject of scattering theory. To incorporate quantum scattering theory into existing theories for HHG would be an exacting task. A starting point may be to consider the exponential term in the Lewenstein model, in (3.3), and to modify or add to the existing term which corresponds to the second step of the three step model, $\exp(-iS(\mathbf{p}, t, t'))$, by including a phase shift due to scattering from neighbouring molecules. As a basis for calculating this term, one may even require a quantum treatment of the liquid potential, solving the Schrödinger equation for many bodies. This in itself is beyond the level of current theory.

Alternatively, one may treat the problem of liquid potentials semi-classically and refer to molecular dynamics to fix molecule positions and orientations whilst the electron is in the continuum. Then, summing coherently over the phase shifts given by scattering theory for many different trajectories, one could calculate the liquid contribution. This additional phase-space of integration would greatly increase the computation resources required but may be possible, though at the expense of including other effects (e.g. propagation). However, this is beyond the current scope of the work, which seeks to abstract from this process the fundamental consequence of scattering and to generate interest among theorists in developing more complex tools.

For that purpose, a much simpler model is assumed. An approximation is made to a classical scattering potential with electrons following their classical trajectories and scattering from isopropanol molecules with hard scattering centres. It is assumed that any collision will perturb the electron trajectories sufficiently to ensure that the electron will no longer return to its parent atom, and therefore its contribution to the harmonics is lost. The probability that an electron on a given trajectory, which corresponds to a photon emission energy, returns to its parent molecule is then applied as a linear filter.

The calculation of these probabilities goes as follows. The probability that an electron is not scattered along its trajectory is approximately the product of probabilities that is not scattered for small time steps, $\Delta t$, between its birth and recombination. This becomes exact when the number of steps, $N$, approaches infinite such that $\Delta t \to dt$.

$$p_{\text{n.s.}} = \prod_{k=1}^{N} 1 - p_k \Delta t, \tag{6.4}$$

$$p_k = p_{\text{scat}}(t_0 + k\Delta t), \tag{6.5}$$

$$N = \frac{t_{\text{rec}} - t_0}{\Delta t} \tag{6.6}$$

where $p_{\text{scat}}(t)$ is the probability of scattering per unit time, at time $t$; and $t_0$ and $t_{\text{rec}}$ are the birth and recombination times of the electron trajectory respectively. Expanding in orders of $\Delta t$,

$$p_{\text{n.s.}} = 1 + \sum_{k=1}^{N} \left( -\frac{1}{k!} \sum_{j=1}^{N} p_j \Delta t \right)^k = e^{-\langle n \rangle}, \tag{6.7}$$

where

$$\langle n \rangle = \sum_{j=1}^{N} p_j \Delta t \tag{6.8}$$

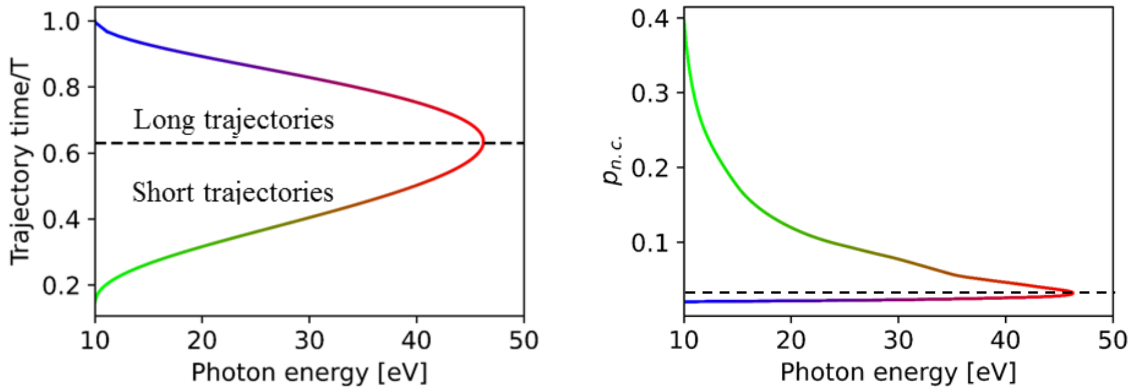
is the average number of collisions that would occur for the electron following its classical, scattering-free trajectory. For infinite $N$,

$$\langle n \rangle = \int_{t_0}^{t_{\text{rec}}} p_{\text{scat}}(t) dt \tag{6.9}$$

The problem is therefore reduced to determining and integrating the probability of the electron scattering per unit time.

In this billiard-ball model, the probability of scattering is given by the probability of encountering a molecule along its path. Considering an infinitesimal time step,

$$p_{\text{scat}}(t)dt = \rho_N A v(t) dt, \tag{6.10}$$




(a) (b)

Figure 6.10: (a) Classical trajectory times and (b) probabilities of non-collision for photon emission generated for a 40 TW cm$^{-2}$ peak intensity, 1800 nm half-cycle pulse in liquid isopropanol. Scattering cross sections used in the calculation of probabilities are unmodified empirical data from [17]

where $\rho_N$ is the number density of the molecules and $A$ is their cross-sectional area.

Figure 6.10a shows the trajectory times of classical electron excursions corresponding to different photon emission energies ($I_p$ =10 eV), calculated for a 40 TW cm$^{-2}$ driving field with 1.8 µm wavelength. Cooler colours show trajectories which begin later in the laser cycle. It is a well known result that trajectories can be separated into 'long' and 'short', depending on whether recombination energy increases or decreases with increased trajectory time. Figure 6.10b shows the probability, for these same trajectories, of the electron not scattering from a neighbouring molecule according to the billiard-ball model. Literature values of low energy scattering sections in isopropanol, which have been made in the vapour phase [17], were used for this calculation. An immediately apparent result is that the long trajectories are significantly more damped than the short. This is explained simply by the longer time spent in the continuum giving greater opportunity for collisions.

Assuming then that the long trajectories offer a negligible contribution to the total emission, the probability of a trajectory recombining maps linearly to the emitted photon energy. The effect of the damping is therefore similar to a spectral filter. Note that the emission is not linearly dependent on the number of emitters, due to the phase-matching of the propagation. For example, if phase-matched, the emission is proportional to the square of the number of emitters.

To simulate the emission, therefore, a strong field approximation calculation was used, including full 3D propagation, and applying this 'scattering filter' at every forward step of the propagation. This SFA kernel has previously been bench-marked against gas-phase HHG measurements [18] and incorporates the effect of plasma defocusing on the driving field intensity.[1]

There are, however, questions about the applicability of vapour phase measurements of scattering cross sections to condensed matter which must be addressed. Measurements in liquids are experimentally challenging, and generally unavailable in the literature. However, a recent comparison of liquid water and amorphous ice argues that they are similar [19] and low energy electrons scatter from amorphous ice with total scattering cross sections an order of magnitude lower than that of vapour-phase water [20]. Therefore, to include this screening effect, a modification to the magnitude of the scattering cross sections was made. The variation of this modification then allows for the HHG spectra to be used to probe its magnitude. In particular, this can be done with reference to the observed photon energy cutoff. Assuming an energy dependence similar to the vapour phase, but scaling the magnitude by a factor $k$,

$$A = \sigma = k\sigma_{emp}, \tag{6.11}$$

$k$ can then be determined through comparison of empirical and numerical data.

Figures 6.11a–c show measured and calculated harmonic spectra for a peak laser intensity varying between 18 and 60 TW cm$^{-2}$ and pulse length of 12 fs, with calculated spectra shown for a range of values of $k$. Figure 6.11a shows calculated harmonic spectra as a function of the laser intensity with a full vapour phase scattering cross section ($k = 1$). This leads to significant damping, which does not accurately model the experimental data. Figure 6.11b ($k = 0.3$) better reflects the experimental data, with the highest energy emission still present, but dampened to the point that the harmonic cutoff appears reduced. Figure 4c ($k = 0$) shows the unscattered calculation.

Comparison of the experimentally determined cutoffs in Figure 4d with the cutoffs from the simulated data for various $k$ shows that weak electron scattering is present to and dampens

[1] The SFA and propagation part of the calculation was carried out by Timur Avni, not the author.

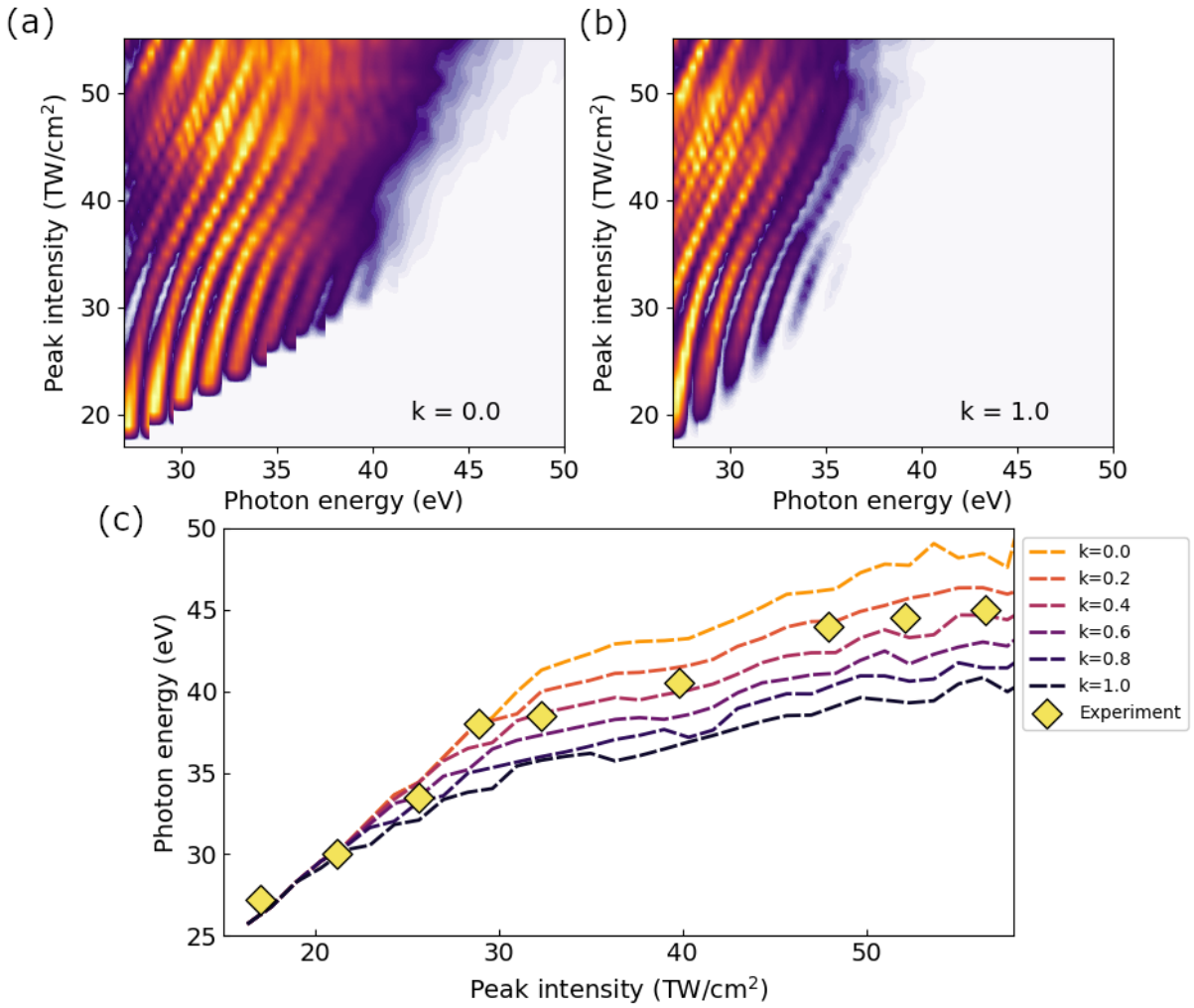



Figure 6.11: Numerical modelling of high harmonic generation in isopropanol-like dense media using a semi-classical strong field approximation, corresponding to experimental conditions. A scattering probability calculation is incorporated with (a) $k = 0$, i.e. no scattering. (b), $k = 1$ (see text). The higher energy trajectories are strongly damped through interactions with neighbouring molecules. Harmonic intensity is self-normalised. (c) Harmonic cutoff energy dependence on peak intensity calculated for varying values of k (dashed coloured lines).

harmonic generation, including below the breakdown threshold of 50 TW/cm$^2$, but only by a few eV. Note that even for $k = 0$ (collision free) there is a deviation from the linear cutoff expected of the single molecule response. This is accounted for by propagation effects. A polynomial fit to second order, made to all the experimental data, is added to help compare the measured to calculated harmonic cutoff scaling with intensity.

A least square fit of the measured data to the theory, with $k$ as the only free parameter, determines that $k = 0.34 \pm 0.05$; therefore, according to this measurement, scattering cross sections of liquid isopropanol are significantly lower (approximately 2.5 – 3.3 times) than those

previously measured in vapour. This simple but effective adaptation to SFA code gives an interesting insight into the behaviour of low energy electrons in liquids and highlights the rich complexity of the liquid phase under strong field illumination. It captures the important aspects of the scattering in that it quantifies the macroscopic screening effects of the surrounding environment. The agreement between theory and experiment shows that the premise for the calculation may prove an adequate description of the underlying physical processes, i.e. that the conservation of momentum is required for successful recombination of the electrons, so that even the elastically scattered electrons will experience sufficient spatial spreading that the recombination probability becomes negligible.

# References


[1] Randy A. Bartels, Ariel Paul, Hans Green, Henry C. Kapteyn, Margaret M. Murnane, Sterling Backus, Ivan P. Christov, Yanwei Liu, David Attwood, and Chris Jacobsen. Generation of spatially coherent light at extreme ultraviolet wavelengths. *Science*, 297 (5580):376–378, jul 2002. ISSN 00368075. doi: 10.1126/science.1071718.

[2] A. Flettner, T. Pfeifer, D. Walter, C. Winterfeldt, C. Spielmann, and G. Gerber. High-harmonic generation and plasma radiation from water microdroplets. In *Applied Physics B: Lasers and Optics*, volume 77, pages 747–751. Springer Berlin Heidelberg, dec 2003. ISBN 0034000313. doi: 10.1007/s00340-003-1329-x. URL `http://link.springer.com/10.1007/s00340-003-1329-x`.

[3] Heiko G. Kurz, Daniel S. Steingrube, Detlev Ristau, Manfred Lein, Uwe Morgner, and Milutin Kovačev. High-order-harmonic generation from dense water microdroplets. *Physical Review A - Atomic, Molecular, and Optical Physics*, 87(6):063811, jun 2013. ISSN 10502947. doi: 10.1103/PhysRevA.87.063811. URL `https://link.aps.org/doi/10.1103/PhysRevA.87.063811`.

[4] Heiko G. Kurz, Martin Kretschmar, Thomas Binhammer, Tamas Nagy, Detlev Ristau, Manfred Lein, Uwe Morgner, and Milutin Kovacev. Revealing the microscopic real-space excursion of a laser-driven electron. *Physical Review X*, 6(3):031029, aug 2016. ISSN 21603308. doi: 10.1103/PhysRevX.6.031029. URL `https://link.aps.org/doi/10.1103/PhysRevX.6.031029`.

[5] Anthony D. DiChiara, Emily Sistrunk, Terry A. Miller, Pierre Agostini, and Louis F. DiMauro. An investigation of harmonic generation in liquid media with a mid-infrared laser. *Optics Express*, 17(23):20959, nov 2009. ISSN 1094-4087. doi: 10.1364/oe.17.020959. URL `https://www.osapublishing.org/oe/abstract.cfm?uri=oe-17-23-20959`.

[6] Tran Trung Luu, Zhong Yin, Arohi Jain, Thomas Gaumnitz, Yoann Pertot, Jun Ma, and Hans Jakob Wörner. Extreme–ultraviolet high–harmonic generation in liquids. *Nature*

*Communications*, 9(1):3723, dec 2018. ISSN 20411723. doi: 10.1038/s41467-018-06040-4. URL http://www.nature.com/articles/s41467-018-06040-4.

[7] Yong Sing You, David A. Reis, and Shambhu Ghimire. Anisotropic high-harmonic generation in bulk crystals. *Nature Physics*, 13(4):345–349, apr 2017. ISSN 17452481. doi: 10.1038/nphys3955.

[8] V. Strelkov. Role of autoionizing state in resonant high-order harmonic generation and attosecond pulse production. *Physical Review Letters*, 104(12):123901, mar 2010. ISSN 00319007. doi: 10.1103/PhysRevLett.104.123901. URL https://link.aps.org/doi/10.1103/PhysRevLett.104.123901.

[9] M. Faubel, S. Schlemmer, and J. P. Toennies. A molecular beam study of the evaporation of water from a liquid jet. *Zeitschrift für Physik D Atoms, Molecules and Clusters*, 10 (2-3):269–277, jun 1988. ISSN 01787683. doi: 10.1007/BF01384861. URL http://link.springer.com/10.1007/BF01384861.

[10] Vlad Sadtchenko, M. Brindza, M. Chonde, B. Palmore, and R. Eom. The vaporization rate of ice at temperatures near its melting point. *Journal of Chemical Physics*, 121 (23):11980–11992, nov 2004. ISSN 00219606. doi: 10.1063/1.1817820. URL https://aip.scitation.org/doi/abs/10.1063/1.1817820.

[11] Susan M. Brastad and Gilbert M. Nathanson. Molecular beam studies of HCl dissolution and dissociation in cold salty water. *Physical Chemistry Chemical Physics*, 13(18):8284–8295, apr 2011. ISSN 14639076. doi: 10.1039/c0cp02540b. URL https://pubs.rsc.org/en/content/articlehtml/2011/cp/c0cp02540bhttps://pubs.rsc.org/en/content/articlelanding/2011/cp/c0cp02540b.

[12] P Heissler, E Lugovoy, R Hörlein, L Waldecker, J Wenz, M Heigoldt, K Khrennikov, S Karsch, F Krausz, B Abel, and G D Tsakiris. Using the third state of matter: High harmonic generation from liquid targets. *New Journal of Physics*, 16(11):113045, nov 2014. ISSN 13672630. doi: 10.1088/1367-2630/16/11/113045. URL http://stacks.iop.org/1367-2630/16/i=11/a=113045?key=crossref.4e0bfe526bd4d7ed190397944c436a02.

[13] G. Wyllie. Evaporation and Surface Structure of Liquids. *Proceedings of the Royal Society A: Mathematical, Physical and Engineering Sciences*, 197(1050):383–395, jun 1949. ISSN 1364-5021. doi: 10.1098/rspa.1949.0071. URL http://rspa.royalsocietypublishing.org/cgi/doi/10.1098/rspa.1949.0071.

[14] Maria Ekimova, Wilson Quevedo, Manfred Faubel, Philippe Wernet, and Erik T. J. Nibbering. A liquid flatjet system for solution phase soft-x-ray spectroscopy. *Structural Dynamics*, 2(5):054301, sep 2015. ISSN 2329-7778. doi: 10.1063/1.4928715. URL http://aip.scitation.org/doi/10.1063/1.4928715http://aca.scitation.org/doi/10.1063/1.4928715.

[15] Piotr Rudawski, Anne Harth, Chen Guo, Eleonora Lorek, Miguel Miranda, Christoph M. Heyl, Esben W. Larsen, Jan Ahrens, Oliver Prochnow, Thomas Binhammer, Uwe Morgner, Johan Mauritsson, Anne L'Huillier, and Cord L. Arnold. Carrier-envelope phase dependent high-order harmonic generation with a high-repetition rate OPCPA-system. *European Physical Journal D*, 69(3):70, mar 2015. ISSN 14346079. doi: 10.1140/epjd/e2015-50568-y. URL http://link.springer.com/10.1140/epjd/e2015-50568-y.

[16] K. S. Budil, P. Salières, M. D. Perry, and Anne L'Huillier. Influence of ellipticity on harmonic generation. *Physical Review A*, 48(5):R3437, nov 1993. ISSN 10502947. doi: 10.1103/PhysRevA.48.R3437. URL https://journals.aps.org/pra/abstract/10.1103/PhysRevA.48.R3437.

[17] M. H.F. Bettega, C. Winstead, V. McKoy, A. Jo, A. Gauf, J. Tanner, L. R. Hargreaves, and M. A. Khakoo. Collisions of low-energy electrons with isopropanol. *Physical Review A - Atomic, Molecular, and Optical Physics*, 84(4):042702, oct 2011. ISSN 10502947. doi: 10.1103/PhysRevA.84.042702.

[18] Allan S. Johnson, Dane R. Austin, David A. Wood, Christian Brahms, Andrew Gregory, Konstantin B. Holzner, Sebastian Jarosch, Esben W. Larsen, Susan Parker, Christian S. Strüber, Peng Ye, John W.G. Tisch, and Jon P. Marangos. High-flux soft x-ray harmonic generation from ionization-shaped few-cycle laser pulses. *Science Ad-*

*vances*, 4(5):eaar3761, may 2018. ISSN 23752548. doi: 10.1126/sciadv.aar3761. URL `http://advances.sciencemag.org/lookup/doi/10.1126/sciadv.aar3761`.

[19] Ruth Signorell. Electron Scattering in Liquid Water and Amorphous Ice: A Striking Resemblance. *Physical Review Letters*, 124(20):205501, may 2020. ISSN 10797114. doi: 10.1103/PhysRevLett.124.205501.

[20] M. Michaud, A. Wen, and L. Sanche. Cross sections for low-energy (1-100 eV) electron elastic and inelastic scattering in amorphous ice. *Radiation Research*, 159(1):3–22, jan 2003. ISSN 00337587. doi: 10.1667/0033-7587(2003)159[0003:CSFLEE]2.0.CO;2.

# Chapter 7

# Concluding comments and future direction

The work described in this thesis aimed to develop tools for studying charge dynamics in molecular systems on the timescale of electronic coherences and apply these tools to the study of small molecular systems, and in particular to liquids. For this purpose, due to availability of suitable ultrafast light sources and the interaction of with core states, X-ray and XUV light is currently the most useful probe of electron coherences, and particular focus has been given to X-ray and XUV interactions.

These aims have been addressed through multiple research directions. Firstly, through the experiment using an XFEL source to study the few femtosecond hole dynamics of isopropanol, which is described in Chapter 4. This experiment provides important evidence of the very fast decoherence of hole wavepackets in the inner valence of a molecule. It also demonstrates a viable method for X-ray absorption spectroscopy using XFEL sources to measure these very fast transients. It is interesting to note the difference in the methods used there from the methods when using an HHG source, such as the experiments which can be conducted with the setup described in Chapter 5. Isolated attosecond pulses from soft X-ray HHG sources have broad spectra which span all transitions up to its cutoff energy, in every pulse. In contrast, the relatively narrow pulses, closer to their transform limit, and large shot-for-shot fluctuations in

XFEL spectra mean that spectral measurements must be made on every shot to know which transitions are being probed.

The success of this method motivates its continued application for the study of few and sub-femtosecond dynamics. In that experiment, an electron spectrometer was used to measure the absorption through the resonant Auger electrons created. This is a sensible choice for the study of low density matter. For liquid targets, it will be more desirable to measure absorption via the transmitted spectrum, and hopefully the technical challenges around measuring the incident and transmitted spectrum at XFEL facilities can be overcome.

The fresh-slice mode used in that experiment was, at the time, the most advanced technique for the generation of femtosecond soft X-ray pulses using an XFEL. XFEL techniques are rapidly advancing and, as discussed in Chapter 3, the enhanced SASE mode can be used to generate high brightness pulses with few-hundred attosecond duration. It is therefore now possible to probe with higher time resolution and higher intensity, allowing for better statistics in the analysis of charge migration.

Another advantage of the newer modes is that there is greater freedom in the photon energies, when using two colours. In this measurement, a difference in energy of only 15 eV was used; whilst this is sufficient to have the pump below the core-shell ionisation edge and the probe resonant with the core-to-inner-valence transition, it has the consequence that the electron spectra are cluttered with direct ionisation from both pulses as well as Auger-Meitner electrons. With the pump pulse further detuned, for example by 100 eV, the direct photoelectrons from the pump are well separated in energy and no longer overlap with the Auger electrons from the probe, allowing for the different contributions to be resolved spectrally. Furthermore, ionisation cross sections from the pump in this case would be larger, increasing excitation fractions.

Experiments utilising the method used to study charge migration in Chapter 4 and utilising all of these advantages are currently ongoing, and the results are highly anticipated. Other techniques for studying attosecond charge dynamics using XFELS have also made rapid advances in recent years. Notably, attosecond angular streaking, sometimes referred to as the 'atto-clock' method, can be used to study ionising phenomena. Attosecond angular streaking has been successfully

applied to study the time structure of Auger-Meitner decay with approximately 150 as resolution, resolving a beating in the emission with time, where previous experiments had only been able to identify a decay rate [1].

Attosecond angular streaking necessarily studies an ionisation channel and is therefore particularly suited to the study of highly excited atoms and molecules, i.e with core holes. The experimental method used in Chapter 4 also studied the charge migration of an ionised molecule, but from the inner valence. The second ionisation step of the probe provides a measurement channel, but the dynamics probed are of the singly ionised molecule. An exciting prospect, particularly for applications towards photo-chemistry, is to generalise this method to the study of neutral molecules. With the recent advances towards higher attosecond pulses, it is now possible to excited valence wavepackets in neutral molecules using impulsive stimulated X-ray Raman scattering (ISXRS) [2, 3], in analogy to the creation of vibrational wavepackets by Raman scattering in the optical domain. Using a ISXRS pump pulse in place of the ionising pump used here is therefore an exciting future direction.

Another of the key research directions in this thesis is the liquid HHG experiments detailed in Chapter 6. Already since that work began, significant discussion and debate has continued in the community, which has led to a number of publications on the theory of high harmonic generation in liquids [4, 5, 6]. It is still unclear to what extent HHG spectroscopy will be possible in liquid targets for the purpose of measuring attosecond charge dynamics, either in solvents or solutes, but this remains an attractive research goal. The work on liquid HHG and the progress described in Chapter 5 demonstrates that liquid flatjets are good targets for in vacuum study of liquids and further investigations using these targets are highly anticipated. Many improvements are still to be made, primarily the demonstration that small (mOD) changes can be resolved with femtosecond time resolution in pump probe X-ray transient absorption experiments in liquids. This will open the field to the study of not only the types of dynamics studied in this thesis but many other phenomena, such as solute-solvent interactions, liquid structure, and liquid phase photo-chemistry. The advances in experimental techniques to achieve this are clear and ongoing: higher average photon flux, improved X-ray stability, improved liquid-target

stability, and in some applications higher photon energy.

In line with this experimental progress, theory is continuing to advance and the understanding of charge dynamics and coherence is better understood than ever. In particular, the interplay between nuclear and electron dynamics is now recognised as crucial to understanding decoherence of electronic wavepackets during charge migration. What remains less understood is whether or how electronic wavepackets lead to different long-term outcomes in the nuclear wavepacket, i.e. the role of electronic coherences on processes such as as chemical reactions or structural change. To understand this, theory and experiment must work across the boundary of dynamics due to the electron wavepacket up to the greater-than-ten femtosecond timescale of nuclear dynamics.

# References


[1] Siqi Li, Taran Driver, Philipp Rosenberger, Elio G. Champenois, Joseph Duris, Andre Al-Haddad, Vitali Averbukh, Jonathan C.T. Barnard, Nora Berrah, Christoph Bostedt, Philip H. Bucksbaum, Ryan N. Coffee, Louis F. DiMauro, Li Fang, Douglas Garratt, Averell Gatton, Zhaoheng Guo, Gregor Hartmann, Daniel Haxton, Wolfram Helml, Zhirong Huang, Aaron C. LaForge, Andrei Kamalov, Jonas Knurr, Ming Fu Lin, Alberto A. Lutman, James P. MacArthur, Jon P. Marangos, Megan Nantel, Adi Natan, Razib Obaid, Jordan T. O'Neal, Niranjan H. Shivaram, Aviad Schori, Peter Walter, Anna Li Wang, Thomas J.A. Wolf, Zhen Zhang, Matthias F. Kling, Agostino Marinelli, and James P. Cryan. Attosecond coherent electron motion in Auger-Meitner decay. *Science*, 375(6578):285–290, jan 2022. ISSN 10959203. doi: 10.1126/science.abj2096. URL `https://www.science.org/doi/10.1126/science.abj2096`.

[2] Satoshi Tanaka and Shaul Mukamel. Coherent X-Ray Raman Spectroscopy: A Nonlinear Local Probe for Electronic Excitations. *Physical Review Letters*, 89(4):043001, jul 2002. ISSN 10797114. doi: 10.1103/PhysRevLett.89.043001.

[3] Jordan T. O'Neal, Elio G. Champenois, Solène Oberli, Razib Obaid, Andre Al-Haddad, Jonathan Barnard, Nora Berrah, Ryan Coffee, Joseph Duris, Gediminas Galinis, Douglas Garratt, James M. Glownia, Daniel Haxton, Phay Ho, Siqi Li, Xiang Li, James Macarthur, Jon P Marangos, Adi Natan, Niranjan Shivaram, Daniel S. Slaughter, Peter Walter, Scott Wandel, Linda Young, Christoph Bostedt, Philip H. Bucksbaum, Antonio Picón, Agostino Marinelli, and James P. Cryan. Electronic Population Transfer via Impulsive Stimulated X-Ray Raman Scattering with Attosecond Soft-X-Ray Pulses. *Physical Review Letters*, 125(7):073203, aug 2020. ISSN 10797114. doi: 10.1103/PhysRevLett.125.073203. URL `https://link.aps.org/doi/10.1103/PhysRevLett.125.073203`.

[4] Chang Long Xia, Zheng Liang Li, Jia Qi Liu, Ai Wu Zeng, Ling Jie Lü, and Xue Bin Bian. Role of charge-resonance states in liquid high-order harmonic generation. *Physical Review A*, 105(1):013115, jan 2022. ISSN 24699934. doi: 10.1103/PhysRevA.105.013115.

[5] Ofer Neufeld, Zahra Nourbakhsh, Nicolas Tancogne-Dejean, and Angel Rubio. Ab Initio Cluster Approach for High Harmonic Generation in Liquids. *Journal of chemical theory and computation*, 18(7):4117–4126, jul 2022. ISSN 15499626. doi: 10.1021/acs.jctc.2c00235.

[6] Ai Wu Zeng and Xue Bin Bian. Impact of Statistical Fluctuations on High Harmonic Generation in Liquids. *Physical Review Letters*, 124(20):203901, may 2020. ISSN 10797114. doi: 10.1103/PhysRevLett.124.203901. URL `https://journals.aps.org/prl/abstract/10.1103/PhysRevLett.124.203901`.

# Appendix A

# Description of the laser system

Chapters 5 and 6 showed results from seeding high harmonic generation used the a few-cycle near infrared (NIR) laser system, in-house at Imperial College London. Whilst the operation, modification, and advancement of this laser system did form a significant part of the effort required to achieve those results, the scientific interest is independent of the laser system itself. That laser system is outlined here.

The laser is seeded by a Kerr-lens modelocked Titanium-doped Sapphire (Ti:Saph) oscillator (KM Labs Red dragon) with a repetition rate of 80 MHz. Dispersion management is done via a prism pair, with the insertion of each prism used to adjust the gain spectrum. The spectrum is centred at approximately 790 nm with a spectral width of 50 nm FWHM. This is lower than the optimum wavelength for gain from Ti:Saph close to room temperature, but is maintained at this wavelength to match the gain of cryogenic-cooled amplifiers. There are two chirped pulse amplifier (CPA) stages, both cooled using liquid helium from a helium compressor. The first is a heavily modified KM Labs Red Dragon amplifier. The pulses are first stretched to 170 ps in a grating stretcher. A Pockels cell and polariser pair are then used to reduce the repetition rate to 1 kHz. The pulses are then input to an eleven pass amplifier in a ring. The amplifier crystal is end-pumped by a single 30 mJ, 527 nm diode laser (Coherent DM527-30). The first 6 passes are spectrally filtered, reducing gain at the centre of the spectrum to limit the effects of gain narrowing. A second Pockels cell is then used to 'clean' the pulse, improving the contrast

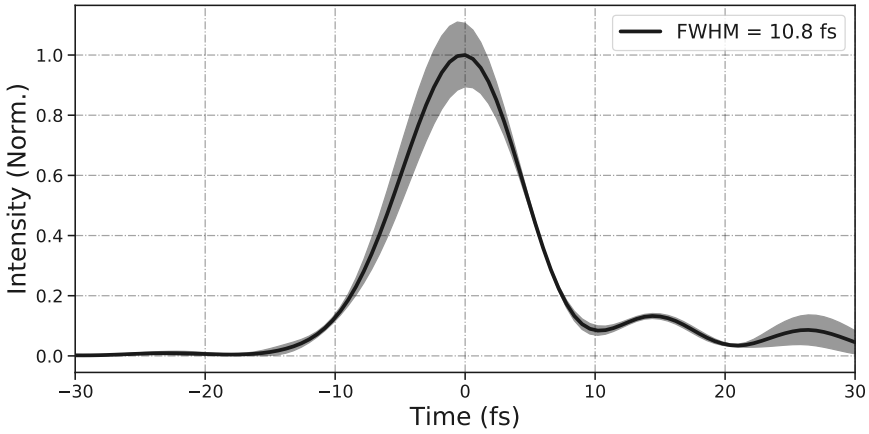



Figure A.1: An 11 fs pulse measured using the SEA-SPIDER method [1]. This 1780 nm, 1.8 cycle pulse is typical those used in Chapter 5 to drive high harmonic generation in the soft X-ray and of the shortest in Chapter 6 used for high harmonic generation in liquids.

ratio. 2.5 mJ pulses are produced in this way. To improve the power and pointing stability, two point active stabilisation is used. This consists of leak-through from a dielectric mirror being profiled in the near- and far-field directly and a PID controller fed back to actuators on two mirror mounts to stabilise the position of the near- and far-field onto references.

The second stage is a bowtie configuration with five passes. It is pumped by two 527 nm diode lasers, one at 27 mJ (Coherent DM527-30) and one at 34 mJ. The output 22 mJ pulse are split with the majority being sent to a grating compressor and the remaining pulses down-sampled by another Pockels cell for other, low-repetition rate applications. Before compression the beam waist is expanded using a lens telescope, to avoid damage to optics when compressed. The compressor consists of a pair of parallel, gold coated, 300 lines $mm^{-1}$ gratings and a retro-reflector for two vertically displaced passes. The second and third order phase is then measured using a commercially built SPIDER and can be optimised by adjusting the spacing between the gratings and the angle of incidence. At this stage it is compressed to a 35 fs pulse, with a transform limit of 29 fs. This 800 nm laser is used to pump a OPA (HE-TOPAS, Light Conversion), converting to a signal pulse at 1400 nm and idler pulse at 1780 nm with approximately 35% conversion efficiency. Operating in this high conversion efficiency regime, the pulse is 60 fs, as measured using a SHG-FROG. This can be broadened to span from below 1100 nm to 2200 nm using a 1.2 m long argon-filled hollow core fibre which is then compressed using a wedge pair. With argon pressure between 1 bar and 1.8 bar, compression to between

11 fs is possible. The pulse can be measured using a SEA-SPIDER [1]. Figure A.1 shows a SEA-SPIDER measurement of an fs pulse, which corresponds to 1.8 optical cycles.

# References

[1] T. Witting, S. J. Weber, J. W. G. Tisch, and J. P. Marangos. Spatio-temporal characterization of mid-infrared laser pulses with spatially encoded spectral shearing interferometry. *Optics Express*, 20(27):27974, 2012. ISSN 1094-4087. doi: 10.1364/OE.20.027974. URL `https://www.osapublishing.org/oe/abstract.cfm?uri=oe-20-27-27974`.